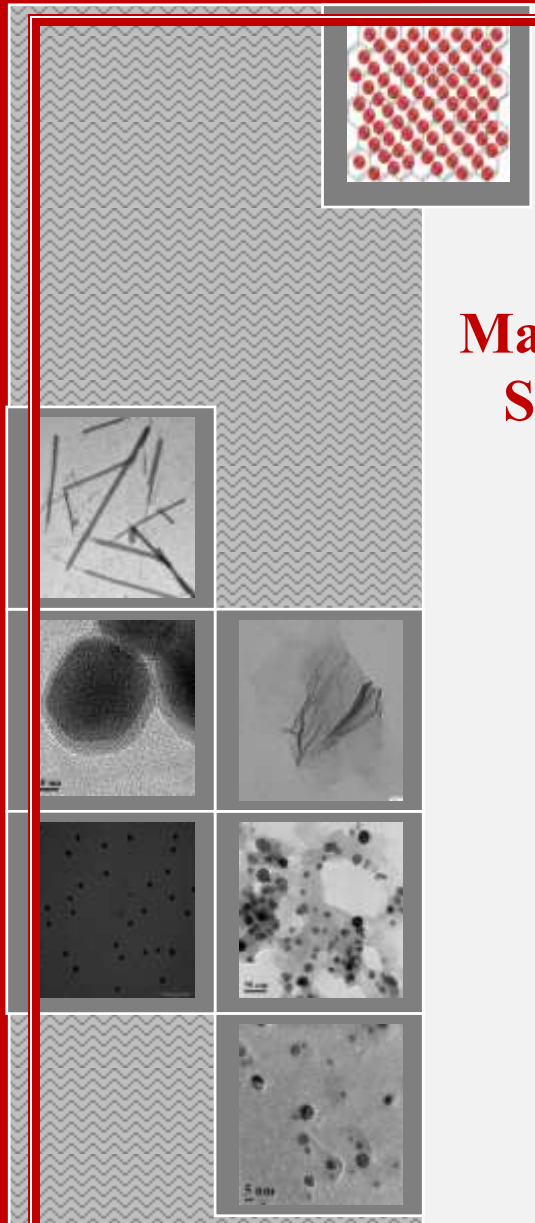


Studies on Structural, Optical and Magnetic Properties of Low Dimensional Systems: CdO, $Cd_{1-x}Mn_xO$, CeO_2 and Graphene based Composites

A
Thesis
Submitted in Partial Fulfillment of the Requirements for the Degree of
Doctor of Philosophy
in
Science

by

Sumeet Kumar

Under the supervision of

Dr. Animesh K. Ojha

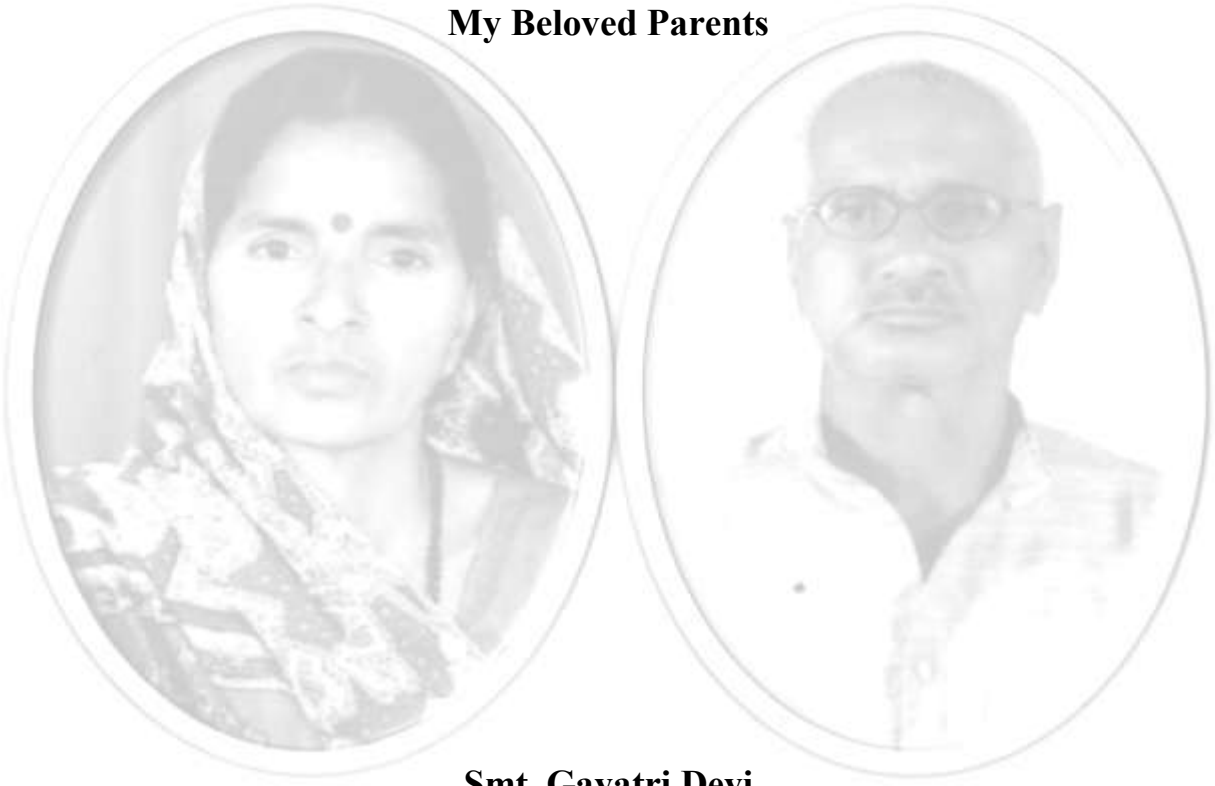
Department of Physics
Motilal Nehru National Institute of Technology
Allahabad – 211004 (India)

April, 2015 **Reg. No.2010RPH 54**

Dedicated

To

My Beloved Parents



Smt. Gayatri Devi

&

Sri Fulena Prasad Singh

Undertaking

I declare that the work presented in this thesis entitled **"Studies on Structural, Optical and Magnetic Properties of Low Dimensional Systems: CdO, $Cd_{1-x}Mn_xO$, CeO_2 and Graphene Based Composites"** submitted to the **Department of Physics, Motilal Nehru National Institute of Technology, Allahabad (India)** for the award of **Doctor of Philosophy** Degree in **Science (Physics)**, is my original work. I neither have plagiarized any part of the thesis nor submitted the same work for the award of any other Degree anywhere. In case this undertaking is found incorrect, the Degree shall be withdrawn unconditionally.

Date: **(Signature of Candidate)**

Place:



Department of Physics

Motilal Nehru National Institute of Technology
Allahabad – 211004 (India)

Certificate

This is to certify that the thesis entitled **"Studies on Structural, Optical and Magnetic Properties of Low Dimensional Systems: CdO, $Cd_{1-x}Mn_xO$, CeO_2 and Graphene Based Composites"** has been submitted by **Mr. Sumeet Kumar** in partial fulfillment of the degree of **Doctor of Philosophy in Science (Physics)** of **Motilal Nehru National Institute of Technology, Allahabad (India)**. He has carried out research work as a full time Ph.D. scholar under my supervision. He has fulfilled all the requirements as per the rules of this institute regarding the submission of his thesis. This work is original and has not been submitted in part or full for any degree or diploma of any University.

Date: **(Dr. Animesh K. Ojha)**

Place: **Thesis Supervisor**

Acknowledgements

I bow my head before the almighty and merciful god for providing me the courage and strength to complete this work.

With profound regards and respect, I avail this opportunity to express my deep sense of gratitude and indebtedness to my supervisor Dr. Animesh K. Ojha, Assistant Professor, Department of Physics, Motilal Nehru National Institute of Technology (MNNIT) Allahabad, for their inspiring guidance, constructive and valuable suggestions throughout my research work. His deep sense of appreciation and dedication to research has been a constant source of inspiration for me during the entire tenure of my Ph.D. It would have not been possible for me to bring out this thesis without his help and constant encouragement throughout my Ph. D. period.

I am grateful to Prof. P. Chakrabarti, Director MNNIT, Allahabad for providing me an opportunity to do research studies at MNNIT. I gratefully acknowledge the financial support from TEQIP-II, MNNIT Allahabad for the execution of some part of the research work presented in the present thesis.

I would like to express my gratefulness to all the faculty members of the Department; Prof. M. Kumar, Prof. S. Chaubey, Prof. P. P. Sahay, Dr. S. N. Pandey (HOD), Dr. A. Agarwal and Dr. Naresh Kumar for their cooperation, suggestions and useful discussion during my research work.

I would like to express my sincere regards to Dr. Rajnish Kurchania (HOD, Deptt. of Physics), NIT Bhopal and Dr. G. Bhagavannarayana (Chief Scientist), NPL, New Delhi for their inspiration to join the scientific world.

My special thanks go to few of my seniors, colleagues and friends, Dr. Manish Srivastava, Dr. Shekhar Prajapati, Dr. Manish K. Singh, Dr. R. K. Mishra, Dr. Ajey K. Tiwari, Dr. Pramod N. G., Mr. Sanjay Srivastava, Mr. S. B. Upadhayay, Mr. Vivek Agrahari, Mr. Mohit Sahni, Mr. Aashish Jha, Mr. Sushant Singh, Mr. Mohan C. Mathpal, Mr. Sachin Kumar, Mr. Kapil K. Sharma, Dr. S. K. Kushwaha, Dr. Muhammed Shkir, Mr. Ramnayan Mukherjee, Mr. Amit srivastava, Mr. Snehasis Bhunia and Mr. Bilal Ahmed.

I also thank to all the supportive staffs, (Dr. J. L Yadav, Sri O. P. Yadav and Mr. Ritesh) of the Department for helping academic and nonacademic levels during my Ph. D.

I would like to express thankfulness to my grandfather (Sri Ramashray singh), other family members; brother (Kanhaiya), brother in law (Shashi Ranjan), sister in law (Pritam) whose blessing, affection and moral support helped me a lot to complete this work.

I am very grateful to my wife Mrs. Jyotshna and my lovely daughters, Shashwati and Kanisha who supported me throughout my Ph.D. course with love and lot of sacrifices.

I feel immense pleasure to express my deepest sense of indebtedness to my father-in-law Sri Krishna Deo Singh and mother-in-law Smt. Sumala Kumari for their support and love without which it would have been impossible to make this work a success.

At last but not least, I feel a deep sense of gratitude for my father Sri Fulena Prasad Singh and mother Smt. Gayatri Devi who provided me a privileged to get higher education and taught me the good things that really matter in my life.

Sumeet Kumar

Abstract

The impact of nanoscience and nanotechnology has enabled us to understand, exploit, fabricate and engineered the materials to build devices at nanoscale. In order to develop unique chemical and physical properties in the materials, it is essential to structured them at the nanoscale. Synthesis of nanomaterials of desired shape and size is the subject of intense research due to their size and shape dependent unique physical and chemical properties. There are two main factors due to which the nanomaterials behave differently than that of its bulk form: (i) surface effects and (ii) quantum effects. In view of the above facts, it was thought worthwhile to synthesize different types of metal oxide based nanomaterials and its composites to explore their physical and chemical properties for applications in various fields of science and technology. The present work deals with the synthesis, characterizations and different applications of metal oxides nanomaterials along with graphene and its composites with metal oxide and sulfide based nanomaterials. The synthesis of metal oxide nanostructures of desired shape and size is one of the primary aims of the present thesis. Several exciting results found during the course of experiments have been described in more detailed in the respective chapters. The present thesis comprises with eight chapters. A brief description of the work presented in each chapter has been given as follows:

In the **first chapter**, the basic aspects of low dimensional systems and fundamentals of nanoscience and nanotechnology have been discussed in somewhat more detailed to make the thesis self-sufficient and consistent. The different aspects of nanoscience and nanotechnology that have been covered in this chapter include: general

introduction to low dimensional systems, effect of dimensionality on different physical and chemical properties of nanostructured materials. This chapter also includes a brief discussion about the materials considered for the investigation in the present work. A brief discussion on carbon based nanostructures such as; graphene oxide (GO), reduced graphene oxide (rGO) and graphene based nanocomposites have also been given in somewhat more detailed in the present chapter.

In the **second chapter**, an overview of different synthesis methods such as; co-precipitation, sol-gel and solvothermal/hydrothermal used for the synthesis of nanostructured materials of different shapes and sizes have been given. Further, a brief description of various characterization techniques such as; X-ray diffraction (XRD), ultraviolet-visible (UV-VIS) spectroscopy, photoluminescence (PL) spectroscopy, Raman spectroscopy (RS), transmission electron microscopy (TEM), high-resolution transmission electron microscopy (HR-TEM), scanning electron microscopy (SEM), vibrating sample magnetometer (VSM) used for characterizing the synthesized products have also been given in the present chapter. The details of photocatalytic and antimicrobial activities measurements of some synthesized nanostructured materials have also been given in somewhat more detailed in this chapter.

In the **third chapter**, a simple, efficient, low cost and template free method for synthesis of well dispersed ultra-long (1μm) CdO nanowires has been presented. The CdO nanowires were characterized by XRD, TEM, UV-VIS spectroscopy and RS measurements. The antimicrobial activities of the synthesized CdO nanowires against

B.subtilis and E.coli microbes were investigated. It has been found that the strength of antimicrobial activity of nanowires was found to be better against B.subtilis than that of E.coli microbe.

In the **fourth chapter**, pure CdO and CdO/MnO_2 (core/shell) nanostructures of various core and different shell sizes were sythesized using co-precipitation method. The phase, size, shape and strutural details of the pure CdO and CdO/MnO_2 (core/shell) nanostructures were investigated by XRD, TEM and RS measurements. TEM images confirm the formation of core/shell nanostructures. The presence of CdO (core) and MnO_2 (shell) crystal phase in the synthesized nanostrutures were detrmined by analyzing the Raman spectra of pure CdO and CdO/MnO_2 (core/shell) nanostructures.

In the **fifth chapter**, monodispersed CeO_2 nanostructures were synthesized using sol-gel method. Size dependent structural, optical and magnetic properties of as prepared samples were characterized by XRD, TEM, UV-VIS, RS and VSM measurements. The decrease in the value of optical band gap with increase of particle size may be attributed to the quantum confinement. The appearance of asymmetrical feature in the Raman peak indicates that the synthesized particles are in nanoscale regime. Weak ferromagnetism at room temperature was observed for the synthesized samples. The increase of saturation magnetization (Ms) and retentivity (Mr) for bigger particle size has been explained in terms of higher number of oxygen vacancies in CeO_2 matrix. The high concentration of Ce^{3+} ions activate more coupling between the individual magnetic moment of Ce ions, leading to an increase of saturation magnetization (Ms) with the particle size.

In the **sixth chapter**, a facile one step in-situ solvothermal synthesis method has been used to synthesize CdS NPs, GO, rGO and rGO-CdS nanocomposites. The structural and optical properties of the synthesized samples have been investigated using XRD, TEM, UV-VIS spectroscopy, PL spectroscopy and RS techniques and a comparative analysis of the results obtained by these techniques have been done. The presence of two distinct Raman peaks in 2D band indicates that the synthesized rGO could be composed by double layers of rGO. The room temperature ferromagnetism (RTFM) of CdS NPs decorated over rGO is decreased compared to pure CdS NPs. The rGO-CdS nanocomposites show enhanced photocatalytic activity for the degradation of methylene blue (MB) dye compared to the pure CdS NPs under ultraviolet (UV) irradiation.

In the **seventh chapter**, one pot in-situ synthesis of CdO NPs, GO, rGO and rGO-CdO nanocomposites has been reported using hydrothermal method. The structural and optical properties of the synthesized samples were investigated by XRD, TEM, UV-VIS, RS and PL spectroscopy. The RTFM of CdO NPs is increased by decorating them over rGO sheets, which may be attributed to the short range magnetic interaction between magnetic moments of CdO NPs and spin units present on the rGO sheets. The photocatalytic activity of the synthesized products has been investigated for photodegradation of MB dye under UV irradiation and found that the 80% of MB dye is degraded by adding the rGO-CdO nanocomposites as a catalyst to the dye solution.

In the **eighth chapter**, based on the research work reported in the present thesis, a brief description of future scope of research work has been given.

Table of Contents

Undertaking of the student.....(i)

Certificate of the supervisor.....(ii)

Acknowledgement.....(iii-iv)

Abstract.....(v-viii)

Table of contents.....(ix-xv)

Bio-data of the author.....(xvi-xvii)

CHAPTER - 1

Introduction.....1 - 45

1.1 Origin of Low Dimensional Systems.....1 - 2

1.2 Basic Concepts of Low Dimensional Systems.....2 - 10

1.2.1 Nanoscience and nanotechnology.....2 - 3

1.2.2 What are low dimensional systems?.....3 - 4

1.2.3 Classifications of low dimensional systems or nanostructured materials.....4 - 5

1.2.4 Significance of low dimensional systems.....5 - 8

1.2.5 Effect of dimensionality on physical and chemical properties.....8 - 10

1.3 Some Interesting Properties of Low Dimensional Systems.....10 - 15

1.3.1 Structural properties.....10 - 11

1.3.2 Catalytic properties.....11 - 11

1.3.3 Electronic properties.....11 - 12

1.3.4 Magnetic properties.....12 - 13

1.3.5 Optical properties.....14 - 15

1.4 Metal Oxide Semiconductor Nanostructures.....16 - 20

1.4.1 Cadmium oxide (CdO).....17 - 18

1.4.2 Cerium oxide (CeO_2).....18 - 20

1.4.2 Manganese oxide (MnO_2).....20 - 20

1.5 Cadmium Chalcogenide Nanostructures.....21 - 22

1.5.1 Cadmium sulfide (CdS).....21 - 22

1.6 Carbon based Nanostructures.....22 - 28

1.6.1 Graphene oxide (GO).....22 - 24

1.6.2 Graphene.....24 - 27

1.6.3 Graphene based composites.....27 - 28

1.7 Applications of Nanostructured Materials.....28 - 29

1.8 Objective of the Present Research Work.....29 - 31

References.....31 - 45

CHAPTER - 2

Synthesis methods and characterization techniques.....46 - 62

2.1 Introduction.....46 - 47

2.2 Synthesis Methods.....47 - 51

2.2.1 Co-precipitation method.....47 - 48

2.2.2 Sol-gel method.....48 - 49

2.2.3 Hydrothermal/solvothermal method.....49 - 51

2.3 Characterization Techniques.....51 - 61

2.3.1 X-ray diffraction (XRD.....51 - 52

2.3.2 Ultraviolet-visible (UV-VIS) spectroscopy.....52 - 53

2.3.3 Photoluminescence (PL) spectroscopy.....53 -54

2.3.4 Raman spectroscopy.....54 - 55

2.3.5 Transmission electron microscope (TEM).....55 - 56

2.3.6 Scanning electron microscope (SEM).....57 - 57

2.3.7 Vibrating sample magnetometer (VSM).....57 - 58

2.4 Photocatalytic Activity.....59 - 60

2.5 Antimicrobial Activity.....60 - 61

References.....61 - 62

CHAPTER - 3

Synthesis, characterization and antimicrobial activities of well dispersed ultra-long cadmium oxide nanowires.....63 - 73

3.1 Introduction.....63 - 64

3.2 Experimental Techniques.....64 - 65

3.2.1 Synthesis.....64 - 65

3.2.2 Characterization.....65 - 65

3.3 Results and Discussion.....65 - 71

3.3.1 XRD and TEM.....65 - 66

3.3.2 UV-VIS spectroscopy.....67 - 68

3.3.3 Raman spectroscopy.....68 - 69

3.3.4 Antimicrobial activity.....*69 - 71*

3.4 Conclusion.....72 - 72

References.....72 - 73

CHAPTER - 4

Synthesis and Raman signature for the formation of cadmium oxide/manganese oxide (core/shell) nanostructures.....74 - 92

4.1 Introduction.....74 - 79

4.2 Experimental Techniques.....79 - 81

4.2.1 Synthesis.....*79 - 80*

4.2.2 Characterization.....*80 - 81*

4.3 Results and Discussion.....81 - 90

4.3.1 XRD.....*81 - 82*

4.3.2 TEM.....*83 - 84*

4.3.3 Raman spectroscopy.....*84 - 90*

4.4 Conclusion.....90 - 91

References.....91 - 92

CHAPTER - 5

Controlled synthesis and magnetic properties of monodispersed cerium oxide nanoparticles.....93 - 120

5.1 Introduction.....93 - 96

5.2 Experimental Techniques.....96 - 98

5.2.1 Synthesis.....*96 - 97*

5.2.2 Characterization.....*97 - 98*

5.3 Results and Discussion.....98 - 115

5.3.1 XRD.....*98 - 101*

5.3.2 TEM and SEM.....*102 - 103*

5.3.3 UV-VIS spectroscopy.....*104 - 106*

5.3.4 Raman spectroscopy.....*107 - 110*

5.3.5 Magnetic properties.....*110 - 115*

5.4 Conclusion.....115 - 116

References.....116 - 120

CHAPTER - 6

In-situ synthesis of reduced graphene oxide decorated with highly dispersed ferromagnetic cadmium sulfide nanoparticles and its photocatalytic activity on methylene blue dye under ultraviolet irradiation.....121 - 154

6.1 Introduction.....121 - 124

6.2 Experimental Techniques.....124 - 130

6.2.1 Synthesis.....*124 - 125*

6.2.1.1 Synthesis of GO.....*126 - 126*

6.2.1.2 Synthesis of rGO.....*127 - 127*

6.2.1.3 Synthesis of pure CdS NPs.....*127 - 128*

6.2.1.4 Synthesis of rGO decorated with CdS NPs.....*128 - 128*

6.2.2 Characterization.....*128 - 129*

6.2.3 Photocatalysis.....*129 - 130*

6.3 Results and Discussion.....130 - 150

6.3.1 XRD.....*130 - 132*

6.3.2 TEM, HR-TEM, SAED and EDX.....*132 - 134*

6.3.3 Raman spectroscopy.....*134 - 137*

6.3.4 UV-VIS spectroscopy.....*138 - 139*

6.3.5 PL spectroscopy.....*139 - 141*

6.3.6 Photodegradation of MB dye.....*141 - 146*

6.3.7 Magnetic properties.....*147 - 150*

6.4 Conclusion.....151 - 151

References.....151 - 154

CHAPTER - 7

One pot in-situ synthesis of reduced graphene oxide decorated with highly dispersed ferromagnetic cadmium oxide nanoparticles for enhanced photocatalytic degradation of methylene blue dye under ultraviolet irradiation.....155 - 186

7.1 Introduction.....155 - 158

7.2 Experimental Techniques.....158 - 164

7.2.1 Synthesis.....*158 - 159*

7.2.1.1 Synthesis of GO.....*159 - 160*

7.2.1.2 Synthesis of rGO.....*160 - 160*

7.2.1.3 Synthesis of CdO NPs.....*161 - 161*

7.2.1.4 Synthesis of rGO decorated with CdO NPs.....*161 - 162*

7.2.2 Characterization.....*162 - 163*

7.2.3 Photocatalytic activity.....*163 - 164*

7.3 Results and Discussion.....164 - 182

7.3.1 XRD.....*164 - 165*

7.3.2 HR-TEM and EDX.....*165 - 167*

7.3.3 Raman spectroscopy.....*167 - 169*

7.3.4 UV-VIS spectroscopy.....*170 - 171*

7.3.5 PL spectroscopy.....*172 - 173*

7.3.6 Magnetic properties.....*173 - 178*

7.3.7 Photocatalytic degradation of MB dye.....*178 - 182*

7.4 Conclusion.....182 - 183

References.....183 - 186

CHAPTER - 8

Scope of future work.....187 - 188

Bio-Data



Name: Sumeet Kumar
Father's name: Sri Fulena Prasad Singh
Mother's name: Smt. Gayatri Devi
Date of birth: 15-08-1982
Nationality: Indian
Category: General
Religion: Hindu

Permanent address:	**Address for correspondence:**
Ramdiri - 3, Ward No.- 6 Dist.- Begusarai (Bihar) - 851129 Contact No: 9935711946	Ramdiri - 3, Ward No.- 6 Dist.- Begusarai (Bihar) - 851129 Contact No: 9935711946

1. Educational qualifications:

S. No.	Degree Obtained	University/ Institution	Year of Passing	Class/ Division	Subject
1.	Ph.D.	MNNIT, Allahabad	2015		Physics
2.	M.Sc.	RGPV, Bhopal	2007	First (H)	Applied Physics
3.	B.Sc. (H)	LNMU, Bihar	2005	First	Physics
4.	I.Sc.	BIEC, Bihar	2000	First	PCM
5.	Matric	BSEB, Bihar	1998	Second	All subjects

2. Professional experience:

S. No.	Organization	Post Held	Period		Work
			From	To	
1.	CSIR-National Physical Laboratory, New Delhi	Project Assistant-II (CSIR network project)	26 February 2009	14 January 2011	Research
2.	School of Nanotechnology, RGPV, Bhopal	Junior Research Fellow	23 April 2008	17 February 2009	Research & Teaching

3. List of publications:

(i) Controlled synthesis and magnetic properties of monodispersed ceria nanoparticles
Sumeet Kumar, Manish Srivastava, Jay Singh, Samar Layek, Madhu Yashpal, Arnulf Materny, Animesh K. Ojha, ***AIP Advances***, 2015, **5**, 027109. **Impact Factor - 1.590**

(ii) Influence of crystal size on the electron–phonon coupling in ZnO nanocrystals investigated by Raman spectroscopy
Animesh K. Ojha, Manish Srivastava, **Sumeet Kumar**, R. Hassanein, Jay Singh, Manish K. Singh, A. Materny, ***Vibrational Spectroscopy***, 2014, **72**, 90. **Impact Factor - 1.547**

(iii) Synthesis and Raman signature for the formation of CdO/MnO_2 (core/shell) nanostructures
Sumeet Kumar, Animesh K. Ojha, Ranjan K. Singh, ***Journal of Raman Spectroscopy***, 2014, **45**, 717. **Impact Factor - 2.519**

(iv) Experimental and theoretical studies on bis (glycine) lithium nitrate (BGLiN): A physico-chemical approach
Mohd. Shkir, Haider Abbas, **Sumeet Kumar**, G. Bhagavannarayana, S. AlFaify, ***Journal of Physics and Chemistry of Solids***, 2014,**75**, 959. **Impact Factor - 1.594**

(v) Synthesis of well–dispersed silver nanorods of different aspect ratios and their antimicrobial properties against gram positive and negative bacterial strains
Animesh K. Ojha, Stefan Forster, **Sumeet Kumar**, Siddharth Vats, Sangeeta Negi, Ingo Fischer, ***Journal of Nanobiotechnology***, 2013, **11**, 42. **Impact Factor - 4.08**

(vi) Synthesis, characterizations and antimicrobial activities of well dispersed ultra-long CdO nanowires
Sumeet Kumar, A. K. Ojha, ***AIP Advances***, 2013, **3**, 052109. **Impact Factor - 1.590**

(vii) Enhancement of SHG, optical and dielectric properties due to improvement in crystalline perfection by annealing in L-asparagine monohydrate single crystal
Mohd. Shakir, S. K. Kushawaha, K. K. Maurya, **Sumeet Kumar**, M. A. Wahab, G. Bhagavannarayana, ***Applied Crystallography***, 2010, **43**, 491-497. **Impact Factor - 3.950**

(viii) In-situ synthesis of reduced graphene oxide decorated with highly dispersed ferromagnetic CdS nanoparticles for enhanced photocatalytic activity under UV irradiation
Sumeet Kumar, Animesh K. Ojha (submitted in **Materials Chemistry and Physics**)

(ix) One pot in-situ synthesis of reduced graphene oxide decorated with highly dispersed ferromagnetic cadmium oxide nanoparticles for enhanced photocatalytic degradation of methylene blue dye under ultraviolet irradiation
Sumeet Kumar, Animesh K. Ojha (submitted in **Applied catalysis A: General**)

(x) Structural, Optical and Magnetic Properties of Mn Doped CdO Nanostructures
Sumeet Kumar, S. Layek, M. Yashpal, A. K. Ojha (Revision submitted in ***J. Magn. Magn. Mater.*** **Impact Factor - 2.002**

Sumeet Kumar

CHAPTER - 1

Introduction

In this chapter, the basic aspects of low dimensional systems and fundamentals of nanoscience and nanotechnology have been discussed in somewhat more detailed to make the thesis self-sufficient and consistent. The different aspects of nanoscience and nanotechnology that have been covered in this chapter include: general introduction to low dimensional systems, effect of dimensionality on different physical and chemical properties of nanostructured materials. This chapter also includes a brief discussion about the materials considered for the investigation in the present work.

1.1 Origin of Low Dimensional Systems

From the beginning of human life on the earth, people have made their sincere efforts to explore the various properties of the matter to make devices and instruments of desired shape, size and properties. In order to make devices for application in various fields of science and technology and can perform functions according to their shape and size, one has to develop the method to manipulate structure of the materials at atomic scale. But, till many of the years after beginning of human life, it was tried only to manipulate the materials for a size and shape which can be seen by the human eye only. It is due to the fact that no instrument was developed to see things beyond the human eyesight. The manipulation of materials for the shape and size that can be seen by the naked eye is known as "millimeter (10^{-3}m) scale technology". After a long period of time, the invention of microscope removed the limitations of human eyesight and established a new scale of technology called micrometer (μm) scale. It helps to see and observe the things at 1000 times smaller than the millimeter. In this period of time, people were not only interested to see the things smaller but also were trying to manipulate the objects at 10^{-6} meter scale and study their various physical and chemical properties. This new scale of technology is used to make various devices and instruments such as; computer chip of size (0.5-1.0 μm) that contains almost 100000 transistors. Further, the micro scale technology was used to make electron microscope. The invention of electron microscope has increased the resolution of naked eye by a factor of 100000 than that of the optical microscope. As electrons have a wavelength of the order of one-millionth of a micrometer (10^{-6}m), it further helps to see the

objects of size 10^{-9} meter. This new scale of technology is called nanometer (nm, 10^{-9}m) scale. The prefix "nano" denotes objects on this scale, and nano-objects are a hundred million times smaller than what can be seen with the naked eye. The invention of electron microscope had allowed one to think and look at the properties of nano scale objects. This had led the foundation stone of nanoscience and nanotechnology, which now has become possible and apparent [1].

1.2 Basic Concepts of Low Dimensional Systems

1.2.1 Nanoscience and nanotechnology

The famous speech entitled "there is plenty of room at the bottom" delivered by Richard Feynman in the annual meeting of the American Physical Society at California Institute of Technology in 1959 [2], was the real origin of the evolution for nanoscience and nanotechnology. But after a long time of this famous speech, Norio Taniguchi, professor of Tokyo Science University, has introduced the term nanotechnology in year, 1974 [3].

Nanoscience is meant for the advanced and collective study of various disciplines of science such as; physics, chemistry and biology at nanoscale regime. It has led a major scientific and technological development for materials by understanding their structural, mechanical, optical, chemical, biological and magnetic properties at nanometer scale (1nm = 10^{-9} meter) [2]. Nanotechnology is a promising area of research and technology which deals with the synthesis, design, fabrication and applications of materials and devices of various sizes and shapes that are engineered at the nanoscale level [4]. The actual significance of nanoscience and nanotechnology is the capability to understand, exploit,

fabricate and engineer materials, devices and systems at nanoscale size [5]. The ideas and concepts of different disciplines of science are taken to design a novel material with desired properties. The change in structural arrangement of atoms and the length scale of material could lead to modification in functionalities and properties of the materials at nanoscale which are significantly different from their bulk materials [6]. These unique properties driven from atomic level study of materials has made a greater impact in the development of science and technology with a remarkable output [5].

1.2.2 What are low dimensional systems?

Low dimensional systems are the materials whose one of the dimension reduced to nanometer length scale at least in one direction. The low dimensional materials exhibit novel structural, chemical, electrical, optical and magnetic properties than that of their bulk form [7]. Nanostructured materials are having average diameter in the range of 1 - 100 nm (10^2 to 10^7 atoms). The word "nano" has come from the Greek word "nanos" which stands for "dwarf" [8]. The word nano is used to represent size and shape of the materials whose one dimension is in order of 10^{-9} meter. The idea of low dimensional systems is not only theoretical but now it has become practically possible to build up structures of confined dimensionality. The confinement of carriers like electrons or holes in a low dimensional structure could lead to an amazing change in their physical and chemical properties due to the manifestation of quantum size effects [9]. The quantum size or confinement effect becomes significant when at least one dimension of the material is comparable to the de-Broglie wavelength of the particle [10]. The motion of electron around the nucleus in an

atom could not be explained by classical laws of physics. In order to address this issue, quantum-mechanical laws were used. These laws states that all matter at the nanoscale behaves as both, waves and particles [11]. All the information about a physical entity like electron, hole and photon or even a physical system such as an atom is described by a wave function and is sufficient to illustrate a particle or system of particles. Physical properties of the materials at nanoscale are predicted in terms of quantum mechanics by Schrödinger wave equation which provides a quantitative understanding of various properties of low dimensional systems [12].

1.2.3 Classifications of low dimensional systems or nanostructured materials

In nanotechnology, the nanostructured materials are classified in different categories. The most popular way to classify nanostructured materials is their dimensionality. On the basis of the number of confined or reduced dimensions to the nanoscale range (<100 nm), the nanostructured materials can be classified in the following categories:

- ***Three dimensional (3D) system*** **–** In a bulk material, all three dimensions are in macroscale regime and no dimensions are in nanoscale regime. In such system, charge carriers are free to move in all three dimensions and hence it is called a three dimensional (3D) system. Example – Bulk.
- ***Two dimensional (2D) system*** **–** In two dimensional systems, two dimensions are in macroscale and one dimension is in nanoscale regime. In this system, the charge carriers are free to move in two dimensions but confined in one dimension. Example – Quantum well.

- ***One dimensional (1D) system*** **–** In one dimensional system, one dimension is in macroscale and other two dimensions are at nanoscale regime. The charge carriers are free to move in one dimension and confined in other two dimensions. Example – Quantum wire.
- ***Zero dimensional (0D) system*** **–** In zero dimensional system, all three dimensions are in nanoscale. In this system, the charge carriers are confined in all the three dimensions. Example – Quantum dot.

Nanostructured materials are generally categorized by their geometrical configuration such as; nanowires, nanorods, nanoparticles, nanoshells and nanocomposites etc. On the basis of size, all categories of the nanostructured materials are shown in Fig. 1.1.

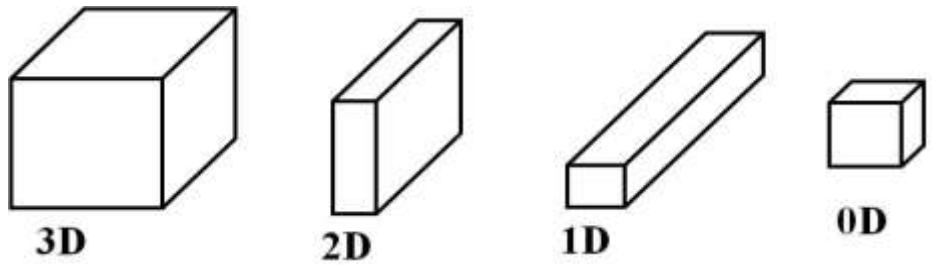


Fig. 1.1 Schematic presentation of low dimensional systems.

1.2.4 Significance of low dimensional systems

The Quantum dot (0D), quantum wire (1D) and quantum well (2D) nanostructures play an important role in fabrication of devices for applications in the fields of nanoelectronics and optoelectronics [4]. As the size of materials is reduced, the electrons are confined significantly such that the deBroglie wavelength of electrons becomes comparable to the physical size of nanostructured materials [10]. As a result, the materials start showing

extraordinary phenomena with unusual electron transfer and optical effects. It means that the properties of materials have become very sensitive to the shape and size of the materials at nanoscale range. Due to size and shape dependent confinement of electrons in nanostructured materials, the devices such as; transistor, memory card and gate could be fabricated and activated at very low voltage (0.2V) [4]. In addition, the band gap of the materials can also be tailored at the desired level by varying the shape and size of the materials. The re-distribution of electrons and holes with within the energy band structure will affect the various optical properties such as; rate of absorption and emission of the materials. The information provided by electronic structure of a material plays a vital role to understand various processes. The physics of low dimensional materials is, therefore, different in comparison to their bulk counterparts. The change in various physical properties of the materials with shape and size can be understood in terms of density of states. The density of state of the materials is a property that tells about how energy levels are packed in the materials [14]. For comparison, the density of states in 3D, 2D, 1D, and 0D nanostructured materials are given in Table 1.1. The variation of density of states with energy is illustrated in Fig. 1.2.

Table 1.1 Density of states of conduction electron in 3D, 2D, 1D and 0D systems.

Types of Nanostructure	**Density of states D(E)**	**Dimensions**	
		Delocalized	Confined
Bulk (3D)	$D(E) \propto E^{1/2}$	3	0
Quantum Well (2D)	$D(E) \propto E^{0}$	2	1
Quantum Wire (1D)	$D(E) \propto E^{-1/2}$	1	2
Quantum Dot (0D)	$D(E) \propto \delta(E)$	0	3

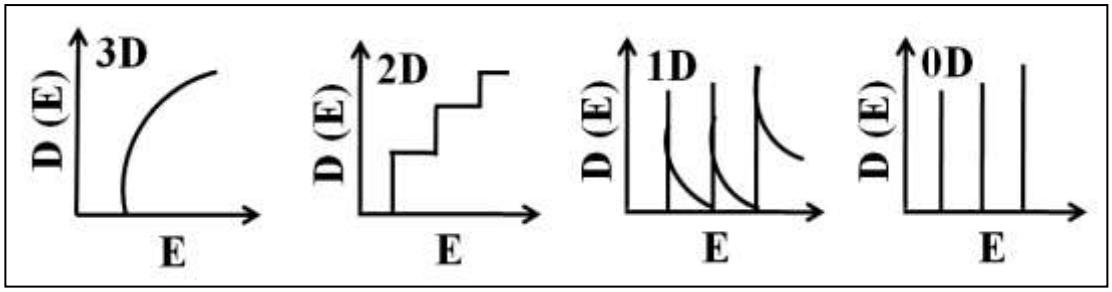


Fig. 1.2 The variation of density of states in 3D, 2D, 1D, and 0D systems with energy.

The shape, size, structural morphologies and dimensionality are the key factors for modification in properties and overall behavior of nanostructured materials owing to their numerous low dimensional characteristics different from their bulk counterparts [5]. These materials can be used in a wide range of applications due to their unique physical and chemical properties. The 0D nanostructured materials of different verities with well controlled dimensions such as; uniform spherical particle, core-shell, quantum dots and hollow spheres have been studied and developed by various physical and chemical methods [15-17]. These nanostructured materials are extensively utilized in light emitting diodes (LEDs), solar cell, single electron transistor and lasers [18-20]. 1D nanostructured materials such as; nanorods, nanowires, nanotubes, nanobelts, nanoribbons etc. are the ideal systems for investigating size and shape dependence of novel properties at the nanoscale regime [21-26]. They are expected to play a significant role in nanoelectronics, optoelectronics and as alternative energy sources [27]. The research field of 1D nanostructured materials has attained a significant attention after the pioneering work by lijima et al. [28] and such materials have been investigated by many other research groups

[29-33]. The 2D nanostructured materials with certain geometries such as; nanowalls, nanodisks and nanofilms [34-36] have become a central area in the materials science research which revealed unique shape dependent properties and it can be utilized for various novel applications such as; sensors, photocatalysts, nanocontainer and templates for synthesizing other nanostructured materials [37]. Owing to the large specific surface area and other superior properties over their bulk counterparts arising from the quantum size effect [38], the 3D nanostructured materials such as; nanoballs, nanocones, nanopillars and nanoflowers have been synthesized [39-42] and their physical and chemical properties have also been investigated thoroughly. It has attracted huge research interest from the scientific community due to their large surface area and other advanced properties compared to their bulk counterparts.

1.2.5 Effect of dimensionality on physical and chemical properties

In 2D structure, the motion of electron is confined along thickness by infinite potential barriers that build a quantum well. In such well, the particle cannot move away from the quantum well. Further, it does not lose any energy after collision with its walls. The quantum states in a quantum well are described by a quantum number. The Eigen energy is increased by reducing the size of the quantum well. The confinement of electrons in a potential well for the nano sized structures provides a dominant and powerful way to control the optical, magnetic and thermoelectric properties of the materials [43]. For 1D structure, the electrons are free to move along one direction only that builds a quantum wire. In this case, the quantum states are described by two principal quantum numbers that

describes the confinement direction of electrons. Similar to quantum well, the Eigen energy of the confined electrons is increased with decreasing the size of the wire [44].

The 0D structure, more commonly known as quantum box, restricts the motion of electrons in all three directions. According to the Heisenberg uncertainty principle, the increased spatial confinement resulted in increase of energy of the confined states. Due to 3D confinement in the 0D structure in contrast with the Quantum well and Quantum wire, which gives only the Eigen energies associated with transverse confinement, the discrete energy level and the short of free propagation of electrons are the main features of 0D structure. An outstanding feature of 0D structure is degeneracy, that appears due to the symmetry of the structure. It occurs when at least two dimensions are of the same length and more than one wave function has the same energy. We call this energy level as doubly degenerate energy levels [45]. Hence, it is obvious that the nature of confinement and dimensionality affect density of states of conduction electrons significantally. The change in physical and chemical properties of nanostructured materials such as; electronic, optical, magnetic and catalytic is mainly governed due to the transformation of energy band levels into quantized discrete energy levels, as the size of materials approaches to atomic dimensions [46]. It is predicted that the spacing between energy levels for the spherical nanoparticle is inversely proportional to the square of the nanoparticle radius [47]. Thus, on the basis of above discussions we can summarize that the following two principal factors are responsible for the unique physical and chemical properties of nanostructured materials than that of their bulk counterparts:

(i) Quantum confinement effect: The nanostructured materials have a reduced dimension at least in one dimension. It restricts the motion of electrons in that particular direction and resulting different optical and electronic properties [46]. The electronic energy levels are not continuous as in the bulk but are discrete in nature.

(ii) Increase in a surface area to volume ratio: The nanostructured materials have a relatively larger surface area compared to the same volume or mass of the materials produced in a bulk form. As a consequence, the number of atoms on the surface increases which ultimately causes to increase surface energy. The larger surface area facilitates the nanostructured materials for number of applications such as; catalysis, drug delivery and energy storage [48-50].

1.3 Some Interesting Physical and Chemical Properties of Low Dimensional Systems

The nanostructured materials exhibit interesting physical and chemical properties compared to their bulk counterpart.

1.3.1 Structural properties: Structural characteristics such as; lattice symmetry and lattice parameters are greatly influenced by size and shape. Bulk materials are typically robust and stable with well defined crystallographic structures. The crystal structure of nanostructured materials is identical as bulk structure except the modification in lattice parameters. Upon reduction in size, inter planer spacing is modified due to presence of short range core-core repulsion and long range electrostatic forces [51]. The variation in thermodynamic stability associated with particle size could also induce structural transformation and modification in lattice parameters. For structural stability,

nanostructures should have low value of surface free energy. The phase of material is highly stable due to low surface free energy at nanoscale dimension [52-53]. The decrease in particle size causes to increase the surface to volume ratio that generates excess stress or strain that causes structural perturbation [54] in the lattice. Size dependent structural distortions associated with change in cell parameters have been reported in earlier studies [55-56].

1.3.2 Catalytic properties: The nanostructured materials have a large fraction of the atoms on its surface. The excess atoms are responsible to increase its reactivity and catalytic activity. Beside this, the other parameters such as; high surface area to volume ratio, the variation in geometrical structure and unique electronic structure also greatly affect the catalytic properties [57]. Hence, nanotechnology has great potential to design new catalytic materials which may be useful for chemical, petroleum, food, pharmaceutical and automotive industries. One of the most important properties of a catalyst is its active surface that participates in chemical reaction. The active surface is increased with reduction of catalyst size [58]. A good example for the development of new catalytic material by the origin of nanotechnology is gold. In general, the bulk form of gold is stable, non-toxic, chemical attack and resistant to oxidation. It has been widely used in making Jewellery. On the other hand, the nanostructured gold is used to catalyze chemical reactions [59].

1.3.3 Electronic properties: The nanostructured materials have unusual electronic structure with different energy level separation and charge carrier density depending on its shape

and size. As a result, they show diverse electronic properties from their bulk form [60]. At nanoscale level, due to quantum confinement effect the energy levels are quantized that causes in the increase of band gap energy, as illustrated in Fig. 1.3. This explains why some of the metals behave like semiconductor and some may behave like insulator, as their size is decreased. It is reported that gold nanoparticles in the size range of 2-5 nm behave as insulator, semiconductor or conductor depending on their dimension due to quantum size effect [61].

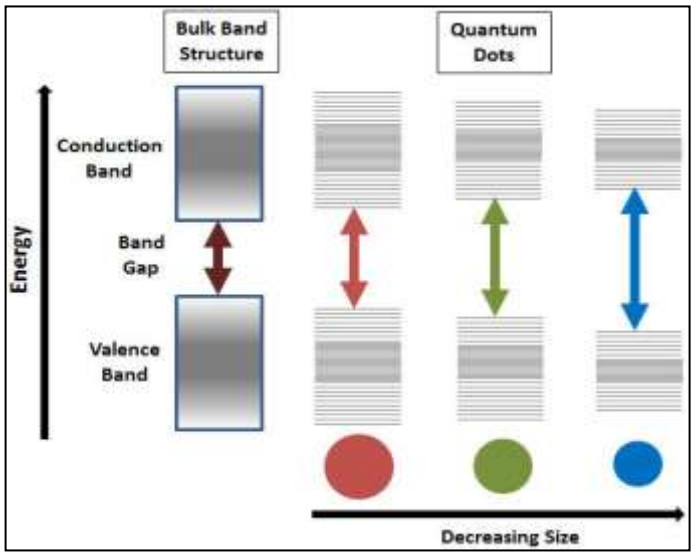


Fig. 1.3 Quantization of energy levels due to particle size effect.

1.3.4 Magnetic properties:

The magnetic properties of the nanostructured materials are also reported to be different compared to its bulk form. The nanostructured materials having ferromagnetic nature, consist of only a single magnetic domain comparison to multiple magnetic domains in their bulk form [62]. The presence of single domain in ferromagnetic nanostructured materials

has made it to use in building high density magnetic memory devices. In order to make ordered single-domain magnetic particle arrays, which is desirable for magnetic memory elements, the materials should have both high values of remanence and coercivity. Remanence and coercivity are determined by anisotropy forces. These forces are affected by many factors such as; shape and size of the nanostructured materials. Among the various anisotropies, the shape dependent anisotropy is quite important since it is directly associated with the change in shape of the nanomagnets [63]. In nanostructured materials, the large surface to volume ratio causes surface atoms to interact (magnetic interaction) differently to its neighboring atoms leading to the surface magnetic characteristics. Upon reduction in size, the surface effect becomes more important due to presence of large fraction of surface atoms on the nanostructured surface [64]. When size of magnetic domain reaches to nanoscale regime, a new property like giant magneto-resistance effect (GME) start appears in the nanomagnets. The GME has a great impact in storing ultra compact information [65]. The nanostructured materials have very less magnetic moment compared to its bulk form and therefore it is possible to convert non magnetic bulk material into magnetic by varying size. For example, the gold is non magnetic at bulk but magnetic at nanoscale [66]. The soft and hard magnetic behaviors materials can also be modified by structuring the materials in their nanoscale range. The soft magnetic materials have small or zero coercive fields that minimize the energy loss in the form of heating during operation (for use in transformer). In hard magnetic materials, large coercive field is required for making a high field magnetic system [62, 67].

1.3.5 Optical properties:

When the size of semiconductor and metal becomes smaller or equal to its Bohr radius, the space for motion of exciton is reduced and as a consequence, the band gap energy is increased [47]. The effective mass theory (EMA) is the most important theory to explain the size dependence of the optical properties of nanometer semiconductors [68]. The quantum confinement effect provides a method of tuning the optical and emission properties of the nano-sized semiconductor over a range of wavelengths by controlling its crystallite size and shape [69]. The nanostructured metals exhibit remarkable surface plasmon resonance where the electrons of conduction band oscillate at the frequency of alternating electric field incident over the material. This effect gives rise to tunable color variation with particle size and shape from visible to near infrared region. The emission of light of a particular wavelength corresponding to the incident radiation is a strong function of the size of nanostructures [46]. In addition, the increased value of energy level spacing is an important criterion for such behavior in semiconductor nanoparticles. Due to increased band gap value for semiconductor nanoparticles upon reduction in particle size, the absorption edge is shifted toward shorter wavelengths. Therefore, semiconductor nanoparticles with different sizes emit different colors after excitation with radiation [47]. Thus, the optical properties of semiconductor nanostructures become very sensitive to the size and shape of the materials. Hence, the fluorescence properties in semiconductor comes due to particle size effect while in metal, it comes due to surface plasmon effect. There are few examples where the materials show different color when they are converted

to nanoparticles. As per example, bulk gold appears yellow while its nanostructures show different color such as; red, purple or orange depending on its shape and size [70]. Similarly, the CdSe emits different colors depending on its size, which is different compared to its bulk form [71]. Fig. 1.4a-b illustrates this effect for metal nanoparticle such as; gold (Fig. 1.4a) and CdSe (Fig. 1.4b) nanoparticles, respectively. These tunable optical properties of semiconductor nanoparticles are widely used as an alternative to make conventional dyes for fluorescence spectroscopy as well as dye sensitized solar cell and these are also being studied as alternative materials for manufacturing light emitting sources.

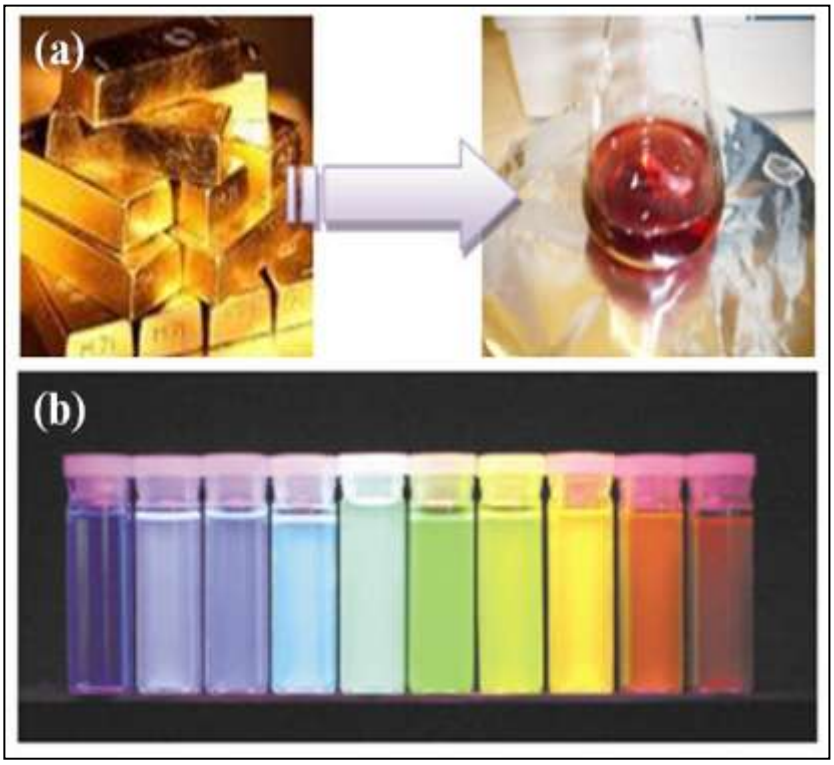


Fig. 1.4 Size dependent emission from (a) gold (b) CdSe nanoparticles.

1.4 Metal Oxide Semiconductor Nanostructures

Nanostructured transition and rare earth metal oxides have been the focus of immense research interest in materials science due to its unique properties and wide variety of technological applications. The nanostructures of mixed oxide materials can produce new properties and also improve the application performance by combining the properties of individual oxide components [72]. The metal elements are able to generate a large range of oxide materials of various physical and chemical properties to be used in variety of applications. The shape and size dependent properties of metal oxide nanostructures is a consequence of large surface area and effective number of surface atoms available in the nanostructured materials [47]. The properties of metal oxide nanostructures are changed drastically with shape and size that makes it ultimate candidate for many technological applications such as; optoelectronics, energy storage, sensing, biomedicine and catalysis etc [73]. The particle size not only affects the surface area of nanostructured materials but also show quantum confinement effect within the nanostructure. The combined effect of size, shape and quantum confinement is responsible for interesting structural, electronic and magnetic properties of the nanostructured materials [74]. The change in lattice parameters upon reduction in particle size has been observed for many metal oxide nanostructures such as; NiO, Fe_2O_3, CeO_2 and ZnO. The crystalline phase of metal oxide such as; TiO_2, Al_2O_3 etc. has been reported as highly stable nanostructure compared to their bulk counterpart. It happens due to low surface free energy at nanoscale regime compared to their bulk form [75]. Low dimensional metal oxides at nanoscale show

discrete energy levels similar to that as shown by an atom. These electronic effects are related to the shifting of exciton energy levels that causes change in optical band gap of the materials [76]. Further, in nanostructured metal oxides, surface properties are also strongly modified due to the presence of low coordination number and uncoordinated atoms like edges or corners or oxygen (O) vacancies. These parameters are responsible to produce specific chemical reactivity for metal oxide nanostructured materials [77]. The controlled synthesis (size, shape, chemical composition and crystal structure) of the nanomaterials is essential to obtain their unique properties and therefore it has become one of the most challenging issues faced by scientists and researchers working in field of nanoscience and nanotechnology. In the forthcoming section, a brief description of some oxide based materials considered in the present study has been discussed in somewhat more detailed.

1.4.1 Cadmium oxide (CdO)

CdO is one among the various transition metal based oxide materials. It is one of the most important transparent conducting oxide (TCO) materials. It belongs to II-VI n-type semiconductor with 2.5 eV direct band gap and 1.98 eV indirect band gap [78]. It generally acquires cubic rocksalt structure after crystallization like sodium chloride along with octahedral cation and anion centers [79]. Pure CdO appears as red or brown but it may also show different colors owing to its tendency to form defect structures due to anion vacancies [80]. Among various nanostructured metal oxides, the CdO nanostructures are expected to play major role in research and development due to their fundamental importance and wide range of potential technological applications due to its interesting

properties like low electrical resistivity, large band gap and high transmission in the visible region [81]. The large value of linear refractive index (2.49) has made it a promising candidate for optoelectronics applications such as; solar cell, liquid crystal displays, photodiodes, IR detectors, anti reflection coatings, phototransistors and sensors [82-85]. Being an n-type semiconductor, CdO has attracted great attention of the scientific community due its application in making low voltage and short wavelength electro-optical devices such as; light emitting dioxides and diode lasers [86]. For these applications, particle size, porosity and specific surface area of the CdO nanostructures are of major importance. So far, verities of CdO nanostructures of various size and structural morphologies have been synthesized. It includes; nanowires [87-89], nanotubes [90], nanofibers [91], nanorods [92], nanoclusters [93], nanocubes [94], nanobelts [95], and nanoparticles [96] by different synthesis methods like hydrothermal [97], template assisted [98], solvothermal [99], chemical co-precipitation [100], vapor phase transport [88], thermal evaporation [90], and sonochemical method [96]. CdO nanostructures have not only the unique optical and electrical characteristics but it also have very interesting catalytic properties that can be used for photodegradation of organic compounds, dyes, pigments and environmental pollutants [101-102]. Further, the antimicrobial properties of the CdO nanostructures have also been reported in the literature [103].

1.4.2 Cerium oxide (CeO_2)

CeO_2, commonly known as ceria, has a chemical formula CeO_2 and it crystallizes in the form of cubic fluorite structure, in which each metal cation is surrounded by eight oxygen

atoms [104]. The optical band gap of pure ceria is reported to be ~ 5 eV, but crystal defects and impurities can convert the material to a good n-type semiconductor [104]. One of the most interesting properties of ceria is its ability to have both +4 and +3 oxidation states. Recently published research articles suggest that the concentration of Ce^{+3} is increased with reduction of particle size [105]. The reduction of Ce^{+4} into Ce^{+3} creates loss of oxygen that generates stable oxygen (O) vacancies or defects in the CeO_2 matrix. The presence of oxygen vacancies may play significant role in developing magnetic behavior in the oxide based nanostructured materials. The density of oxygen vacancies and presence of Ce^{+3} oxidation states into CeO_2 matrix mainly depend on the synthesis methods and the oxidation state of Ce atom in the precursor salt [106]. Atomic size of Ce^{+3} (1.14 Å) is significantly larger than that of Ce^{+4} (0.97 Å) and therefore the size of the unit cell is increased due to expansion in the lattice constant [107]. The oxygen vacancies and defects present in CeO_2 nanostructures can create electronic states within the band gap which further lead to its special electronic properties and emission properties. The modification in band gap induces unique optical property that plays a key role to develop interesting catalytic behavior in CeO_2 nanostructures. As a result, the CeO_2 nanostructures have extensively used in automobile to reduce the emissions of carbon monoxide (CO) and hydrocarbons from the automobile exhaust [108].

Bulk CeO_2 as well as its nanostructures have also been used as hydrogen storage materials [109]. In addition, the CeO_2 nanostructures adsorb CO and decompose NO and SO_2 at room temperature. It can be used as base material of electrolytes and electrodes for

solid oxide fuel cells [110]. The increase in oxygen vacancies enhances the diffusion rate of oxygen in the lattice that causes better catalytic activity and ionic conductivity. Furthermore, it has attracted an extensive attention to the scientific community due to their prospective applications in a variety of field such as; polishing material [111], catalytic material [112], solar cell [113], luminescent material [114] and oxygen sensor [115] as well as oxygen storage capacitor [116]. The crystalline CeO_2 nanostructures have been synthesized by means of a variety of methods, including room-temperature solution precipitation [117], sonochemical [118], hydrothermal crystallization [119], microemulsion [120], mechanochemical processing [121], thermal decomposition [122], spray pyrolysis [123], sol–gel [124], thermal hydrolysis [125] and solvothermal [126].

1.4.3 Manganese oxide (MnO_2)

MnO_2 is an inorganic compound having rutile crystal structure with three-coordinate oxide and octahedral metal centres [127]. It is one of the oxide materials of manganese among different types of manganese oxides such as; MnO, Mn_3O_4, Mn_2O_3 and Mn_2O_7. The MnO_2 is low-cost, non-hazardous materials available in various polymorphic forms. It forms a variety of polymorphs such as; α-MnO_2, β-MnO_2 and γ-MnO_2 [128]. MnO_2 is used as a pigment in glass making as well as ceramics and as a precursor to prepare ferromanganese for use in steel industry and also in making other manganese compounds such as; $KMnO_4$ [129]. It can be a suitable material for dry cell batteries such as; alkaline battery and zinc carbon battery. The annually consumption of MnO_2 for this purpose is around 500,000 tonnes [130].

1.5 Cadmium Chalcogenide Nanostructures

A chalcogenide is a chemical compound that consists of at least one chalcogen anion and one electropositive element. The word chalcogen is generally used for sulfides, selenides, and tellurides. The elements of group sixteen in the periodic table are considered as chalcogens [130]. Metal chalcogenide follows the formula ME, where M belongs to a transition metal and E belongs to sulphur (S), selenium (Se), and tellurium (Te). Metal chalcogenide is a chemical compound made up of combination of metal element and chalcogen anion such as; S, Se or Te [131]. Nowadays, the nanostructured metal chalcogenide has created a center of significant attention due to their exceptional properties suitable for various technological applications.

1.5.1 Cadmium sulfide (CdS)

CdS is an inorganic compound having chemical formula CdS. It belongs to II-VI classof semiconductor and appears in yellow color [132]. In nature, it crystallizes in two different crystal structures such as; hexagonal wurtzite structure (found in the mineral Greenockite) and the cubic zinc blende structure (found in the mineral Hawleyite). At high pressure, CdS can be found in rock salt crystal structure similar to the structure of NaCl [131]. It has a direct band gap of 2.42 eV in its bulk form. The value of its optical band gap can be tuned by changing its shape and size [133]. The CdS nanostructures can be synthesized by co-precipitation method using soluble cadmium salts with sulfide ion. It is reported that the chemical precipitation method results cubic zinc blende type structure of CdS nanostructures [133]. Several other synthesis methods such as; sol-gel [134], evaporation

[135], template [136], solvothermal [137] and hydrothermal [138] have also been used to fabricate CdS nanostructures of various shapes and sizes. The CdS nanostructures can be used as pigment due to their good thermal stability against light and weather fastness and high opacity. Approximately, 2000 tons of CdS nanostructures are manufactured annually for this purpose [139]. It has good applications in making photo-resisters which is sensitive to visible and infra-red light. Thin films of CdS have already been used as transducers operated at GHz frequencies and its combination with other materials (composites) has been utilized in manufacturing different types of solar cells [140]. The CdS nanostructured materials can act as electroluminescence [141] and also have been used in solid state laser [142].

1.6 Carbon Based Nanostructures

After hydrogen, helium and oxygen, carbon is the fourth most abundant element in the universe (by mass) and the second most abundant mass within the human body. It makes carbon the most important element for all known life on earth [143]. Carbon based nanostructures are defined as the materials that consist of carbon atoms. The fullerenes and carbon nanotubes are the excellent examples of it.

1.6.1 Graphene oxide (GO)

Graphite is a three dimensional carbon based material made up of millions of graphene layers. When graphite is treated with strong oxidizing agents, oxygen containing functionalities are introduced in the graphite structure due to the oxidation of graphite. The oxidized graphite is called graphite oxide. Graphite oxide is a compound made up of

carbon, hydrogen and oxygen based molecules [144]. The presence of oxygen functionalities increase the layer separation of graphite and make the material hydrophilic. Due to hydrophilic nature, it can be dispersed in water. After sonication, graphite oxide can be exfoliated to produce its single or few layers, known as GO [145]. Thus, the main difference between graphite oxide and GO is the number of layers present in the synthesized material. The easy dispersability in water and other organic solvents is one of the important advantages of GO compared to the graphite. In comparison to graphite, the sheets in oxidized graphite or GO are heavily oxygenated by hydroxyl and epoxide functional groups located on their basal planes. However, the carbonyl and carboxyl groups are located at the sheet edges [146]. The presence of functional group with GO can vitally modify its properties. The chemically modified GO could then potentially become much more adaptable for various applications. Depending upon the application, the GO can be functionalized through different methods.

Brodie was the first person who demonstrated the synthesis of GO in 1859 by using potassium chlorate, graphite and fuming nitric acid [147]. After a long time, in 1898, Staudenmaier [148] made a small change in this protocol by adding sulfuric acid with fuming nitric acid and additional amount of potassium chlorate that produced improved oxidized GO. In 1958, Hummers [144] reported a more efficient method in which graphite is oxidized by using potassium permanganate ($KMnO_4$) and sodium nitrate ($NaNO_3$) in concentrated sulfuric acid (H_2SO_4). Nowadays, this is the most popular and commonly used method for the synthesis of GO. It should be noted that all three above mentioned

procedures involved the generation of the toxic gases such as; NO_2, N_2O_4 and ClO_2 with being explosive. To overcome these problems, a new method called "improved method" has been investigated [149] in year 2010. In this method, the scalable preparation of GO is achieved by treatment with $KMnO_4$ and concentrated H_2SO_4 with addition of phosphoric acid (H_3PO_4).

The GO can be utilized as containers for corrosive acids when painted on copper or glassware. It can also be used in DNA analysis applications and making GO based DNA sensors [150]. In addition, it has been considered as a freestanding flexible battery anode material for lithium-ion and sodium-ion batteries. Graphene-coated plastic films could be used in medical packaging to improve shelf life [151]. The most attractive property of GO is its reduction (partly) to graphene like sheets by mixing suitable reducing agents. The reducing agent mainly removes the oxygen containing functional groups and the recover the layered conjugated carbon structure [152].

1.6.2 Graphene

Graphite, diamond and amorphous carbons are three naturally occurring allotrope of carbon. The bonding and structures of the carbon atoms within these three naturally occurring allotropes are different. The diamond has crystalline structure while amorphous carbon (such as coal or soot) does not have a crystalline structure. However, the graphite contains thousands or even more of individual layers of hexagonally linked carbon atoms coordinated through covalent bonds in a form of honeycomb lattice stacked together. These covalent bonds are very strong, and carbon atoms are separated by 0.142 nm [153].

Graphene is basically a single layer of graphite in which the carbon atoms are bonded together hexagonally in a honeycomb lattice structure. Graphene was discovered in year 2004 [154]. It is an allotrope of carbon where carbon atoms are bonded through sp^2 bonds in a plane type of structure with bond length 0.142 nm. The layers of graphene stacked on the top of each other similar to graphite, with an interplanar spacing of 0.335 nm [155]. Due to extraordinary properties such as; large surface area, exceptional thermal conductivity high Young's modulus and high electrical conductivity, graphene has been widely used in commercial and industrial applications to make optoelectronics and nanoelectronics based devices such as; batteries, supercapacitors and composites [156-159]. However, the strong Vander Waals force and π-π stacking interaction among graphene layers causes aggregation that limits the performance of graphene. In order to have satisfactory performance, the aggregation problem can be minimized or prevented by decreasing π-π stacking interaction through functionalization of graphene sheets [160]. Further, in order to make monolayer or few-layer graphene sheets from GO, the chemical method is currently most suitable synthesis method for reduction of GO into reduced graphene (rGO). In the laboratory, the rGO or graphene is mainly produced by chemical reduction using hydrazine, sodium boron hydride and hydroquinone etc. The reduction of GO will remove most, but not all, of the oxygen containing functional groups [161]. Once rGO is produced, there are many approaches to functionalize rGO by treating it with other chemicals or by creating new compounds by combining rGO with other materials for their use in different commercial applications [162]. Some interesting properties/features of

graphene that can be used to explore its various applications [163-175] are summarized under the following points:

- Graphene is forty times stronger than the diamond and three hundred times stronger than A36 structural steel at 130 gigapascals.
- It offers energy levels for electronic conduction with very high electron mobility due to presence of free pi (π) electron at each carbon atom. This characteristic of graphene can be used to make photovoltaic cells and supercapacitors that will be able to charge our mobile telephones and tablet computers in a matter of minutes while walking to school or work.
- Graphene can be used to enhance the capacity and charge rate of batteries as well as the longevity. Currently, silicon is widely being used to store large amounts of energy. But that potential amount reduces drastically on every charge or recharge. By use of graphene, batteries can be made with almost no reduction in storage capacity between charges. It means that the electronic devices may be able to be charged faster.
- Another use of graphene is in paint. Graphene is highly inert and can act as a corrosion barrier between oxygen and water diffusion. This could be grown onto any metal surface to avoid the metal from corrosion.
- Due to its ultimate strength, it can be developed as a potential replacement for Kevlar (strong bulletproof material) in protective clothing. Being extremely translucent, it can be able to fit intelligent windows to home, with virtual curtains.

- It can also be used in security orientated clothing for protection against unwanted contact with the use of electrical discharge.

1.6.3 Graphene based composites

Graphene based metal oxide composites are emerging as a new category of materials that showing the properties of both, graphene and metal oxides. Owing to large surface area with exceptionally well electrical, thermal and mechanical properties, graphene offers a broad range of possibilities to synthesize graphene based metal oxide composite materials for several applications such as; battery, supercapacitor, photovoltaic cell, photocatalysis and fuel cell etc [176]. When the materials such as; polymer and inorganic nanostructures are decorated over the graphene sheet, the resulting composite material evolved with remarkably improved properties that can't be observed in graphene and metal oxides individually. In the last few years, a lot of efforts have been made to develop the composites of inorganic nanostructures of metals, metal oxides and semiconductors with graphene [177]. Graphene serves as a useful substrate for decorating inorganic nanostructured materials over its surface to enhance their properties. Recently, a great number of efforts have been made to incorporate various metals, metal oxides and semiconducting nanostructures such as; Au [178], ZnO [179], CdS [180] and CdSe [181] etc. over graphene for getting exceptional properties different than that of individual graphene and metal oxides. In general, in-situ growth technique such as; solvothermal/hydrothermal is used for synthesizing graphene based composites. The most important advantage of this technique is the uniform distribution of nanostructures on

graphene surface with direct interfacial contact between graphene sheets and nanostructures. Further, the in-situ approach overcomes the aggregation problems and low yield production of graphene layers significantly [182]. Other methods such as; sol–gel [183], UV assisted reduction [184], thermal treatment [185] and soft chemical route [186] has also been employed to prepare graphene based metal oxide composites.

1.7 Applications of Nanostructured Materials

Due to unique nature of nanostructured materials compared to their bulk counterpart, it has been used for various applications. The quantum confinement causes to change their various properties such as; optical, electronic, electrical, mechanical and magnetic etc. Thus, these unique properties have made the nanostructures to fabricate miniaturized devices for potential applications. In the recent years, the nanostructures are gaining wide range of applications in area such as; optoelectronics, photonic band gap materials, nanoelectronics, catalysis, sensing, drug delivery, energy and data memory storage etc [187-191]. The point wise applications of nanomaterials [192-197] are given below:

- ***Applications of nanostructures in chemical industry:*** Nanocomposites based coating systems, production of chemicals and magnetic fluids.
- ***Applications of nanostructures in catalysis:*** Catalytic converter and photocatalytic devices.
- ***Applications of nanostructures in medicine:*** Active agents in drug delivery systems and cancer therapy, tissue engineering, fluorescent biological labels, rapid test for medical diagnosis, separation and purification of biological molecules and

cells, antimicrobial agents, probing of DNA structure, detection of proteins, tumor destruction.

- ***Applications of nanostructures in automotive industry:*** Light weight automobile construction, painting and sensors.
- ***Applications of nanostructures in electronic industry:*** Electrode, data memory, Glass fibers, displays and laser diodes.
- ***Applications of nanostructures in energy Sources:*** Batteries, ultra capacitors, solar as well as photovoltaic cell and fuel cells.
- ***Applications of nanostructures in cosmetics:*** Antiseptic cream, tooth paste and UV light protection creams.

1.8 Objective of the Present Research Work

In view of above discussed studies on unique properties of low dimensional systems mainly, metal oxide nanostructures (transition and rare earth), graphene and graphene based nanocomposites and their applications in various fields of science and technology, it has been found that these materials are of great importance because of its tendency to produce unique shape and size dependent physical and chemical properties. But, expensive synthesis methods, complicated steps and aggregation or agglomeration problems of the nanostructures synthesis limits us the synthesis of controlled shape and size and consequently their possible applications in various fields. A highly controlled synthesis of desired shape and size depending upon its applications of the nanostructured materials with high reproducibility is still a great challenge for the scientific community. Further, as

graphene has excellent chemical and physical properties, but restacking tendency of graphene during reduction due to Vander Waals and π-π stacking interactions limits the wide applications of graphene for advancement of the future technology. Thus, in case of graphene also, the aggregation of graphene layers creates a great loss of effective surface area of graphene. It can be minimized by decreasing π-π stacking interactions through incorporation of nanoparticles on graphene sheets by decorating them over the graphene sheets. The world wide scientists have been still trying to develop an easy and efficient method to synthesize well controlled shape and size of the nanoparticles and graphene based metal oxide nanocomposites. In this context, a systematic study on shape and size dependent magnetic and optical properties of CdO, CeO_2 and CdO/MnO_2 (core/shell) nanostructures are still lacking in the literature. Further, a simple and low cost synthesis of graphene based CdS and CdO composites and their optical and magnetic properties along with its photocatalytic applications have not been thoroughly addressed in the literature. Thus, in view of above mentioned facts on shape and size dependent properties of metal oxides and their composites with graphene, it is worth to perform a systematic study on magnetic and optical properties of such systems along their some possible applications. Thus, the objective of the research work presented in the current thesis can be summarized under the following bullet points:

- To synthesize ultra-long nanowires of CdO using simple and low cost synthesis method and study their optical properties. The antimicrobial activity of synthesized CdO nanowires has also been tested on different microbes.

- To develop an efficient and low cost synthesis protocols to synthesize well controlled CdO/MnO2 (core/shell) nanostructures of different core and shell size and study their optical properties.
- To synthesize different size of highly dispersed and spherical CeO_2 nanoparticles and study their optical and magnetic properties as function of size.
- To synthesize GO, rGO and rGO decorated with highly dispersed CdS nanoparticles and study their optical and magnetic properties. The photocatalytic activity of GO, rGO and rGO decorated with CdS nanoparticles and pure CdS nanoparticles will be investigated for the photodegradation of methylene blue (MB) dye molecule under ultra-violet radiation.
- To synthesize GO, rGO and rGO decorated with highly dispersed CdO nanoparticles and study their optical and magnetic properties. The photocatalytic activity of GO, rGO and rGO decorated with CdO nanoparticles and pure CdO nanoparticles will be investigated for the photodegradation of MB dye molecule under ultraviolet radiation.

References

[1] L. Tilstra, S. A. Broughton, R. S. Tanke, D. Jelski, V. French, G. Zhang, A. K. Popov, A. B. Western, T. F. George, The science of nanotechnology: An introductory text, Nova Science Publishers, Inc. New York, 2008.

[2] (a) R. P. Feynman, Eng. Sci., 1960, **23**, 22. (b) http://www.nano.gov.

[3] N. Taniguchi, Proceedings of the international conference on production engineering,

Tokyo, Part II, Japan society of precision engineering, 1974, **18**, 23.

[4] G. Schmid, Nanoparticles from theory to applications, Wiley-VCH, Weinheim, 2004.

[5] G. Timp, Nanotechnology, Springer, New Jersy, 2004.

[6] J. R. Heath, Science, 1995, **270**, 1315.

[7] J. M. Thomas, Pure Appl. Chem., 1988, **60**, 1517.

[8] M, Fang, W. M. Zeisberg, C. Condon, V. Ogryzko, A. Danchin, U. Mechold, Nucl. Acids Res., 2009, **37**, 5114.

[9] J. H. Zhang, Acc. Chem. Res., 1997, **30**, 423.

[10] F. Raimondi, G. G. Scherer, R. Kötz, A. Wokaun, Angew. Chem. Int. Ed., 2005, **44**, 2190.

[11] M. Kerker, J. Colloid Interface Sci., 1985, **105**, 297.

[12] C. Cohen-Tannoudji, B. Diu, F. Laloe, Quantum mechanics, John Wiley & Sons, New York, 1991.

[13] A. P. Alivisatos, J. Phys. Chem., 1996, **100**, 13226.

[14] P. Butcher, N. H. March, M. P. Tosi, Physics of low dimensional semiconductor structures, Plenum Press, New York, 1993.

[15] Y. T. Kim, J. H. Han, B. H. Hong, Y. U. Kwon, Adv. Mater., 2010, **22**, 515.

[16] G. Zhang, D. Wang, J. Am. Chem. Soc., 2008, **130**, 5616.

[17] J. Wang, M. Lin, Y. Yan, Z. Wang, P. C. Ho, K. P. Loh, J. Am. Chem. Soc. 2009, **131**, 11300.

[18] J. W. Stouwdam, R. A. J. Janssen, J. Mater. Chem., 2008, **18**, 1889.

[19] W. Lee, S. H. Kang, J. Y. Kim, G. B. Kolekar, Y. E. Sung, S. H. Han, Nanotechnology, 2009, **20**, 335706.

[20] V. G. Mokerov, Y. V. Fedorov, L. E. Velikovski, M. Y. Scherbakova, Nanotechnology, 2001, **12**, 552.

[21] L. Huang, H. Wang, Z. Wang, A. Mitra, D. Zhao, Y. Yan, Chem. Mater., 2002, **14**, 876.

[22] T. Okada, K. Kawashima, Y. Nakata, X. Ning, J. Appl. Phys., 2005, **44**, 688.

[23] J. M. Park, K. S. Nalwa, W. Leung, K. Constant, S. Chaudhary, K. M. Ho, Nanotechnology, 2010, **21**, 215301.

[24] L. M. Cao, H. Tian, Z. Zhang, X. Y. Zhang, C. X. Gao, W. K. Wang, Nanotechnology, 2004, **15**, 139.

[25] Y. Wang, J. Y. Lee, J. S. Kim, G. H. Kim, K. S. Kim, Chem. Mater., 2007, **19**, 3912.

[26] Y. W. Wang, B. H. Hong, J. Y. Lee, J. S. Kim, G. H. Kim, K. S. Kim, J. Phys. Chem. B, 2004, **108**, 16723.

[27] S. V. N. T. Kuchibhatla, A. S. Karakoti, D. Bera, S. Seal, Prog. Mater. Sci., 2007, **52**, 699.

[28] S. Iijima, Nature, 1991, **354**, 56.

[29] B. H. Hong, S. C. Bae, C. W. Lee, S. Jeong, K. S. Kim, Science, 2001, **294**, 348.

[30] B. H. Hong, J. Y. Lee, C. W. Lee, J. C. Kim, S. C. Bae, K. S. Kim, J. Am. Chem. Soc., 2001, **123**, 10748.

[31] B. H. Hong, J. Y. Lee, T. Beetz, Y. Zhu, P. Kim, K. S. Kim, J. Am. Chem. Soc., 2005,

127, 15336.

[32] I. C. Hwang, et al. J. Phys. Chem. B, 2010, **114**, 7216.

[33] W. Y. Kim, Y. C. Choi, K. S. Kim, J. Mater. Chem., 2008, **18**, 4510.

[34] X. Dong, X. Ji, J. Jing, M. Li, J. Li, W. Yang, J. Phys. Chem. C, 2010, **114**, 2070.

[35] A. K. P. Mann, S. E. Skrabalak, Chem. Mater., 2011, **23**, 1017.

[36] S. H. Jung, E. Oh, K. H. Lee, Y. Yang, C. G. Park, W. Park, et al. Cryst. Growth Des., 2008, **8**, 265.

[37] J. W. Jun, J. W. Seo, S. J. Oh, J. Cheon, Coord. Chem. Rev., 2005, **249**, 1766.

[38] X. W. Teng, X. Y. Liang, S. Maksimuk, H. Yang, Small, 2006, **2**, 249.

[39] L. Wang, Y. Yamauchi, Chem. Mater., 2009, **21**, 3562.

[40] J. N. Wang, L. F. Su, Z. P. Wu, Cryst. Growth Des., 2008, **8**, 1741.

[41] J. Liu, J. Essner, J. Li, Chem. Mater., 2010, **22**, 5022.

[42] W. Lei, D. Liu, J. Zhang, P. Zhu, Q. Cui, G. Zou, Cryst. Growth Des., 2009, **9**, 1489.

[43] R. Dingle, W. Wiegmann, C. H. Henry, Phys. Rev. Lett., 1974, **33**, 827.

[44] Y. Xia, P. Yang, Y. Sun, Y. Wu, B. Mayers, B. Gates, et al., Adv. Mater., 2003, **15**, 353.

[45] S. M. Reimann, M. Manninen, Reviews of modern physics, 2002, **74**, 1283.

[46] S. Link, M. A. El-Sayed, Annu. Rev. Phys. Chem. 2003, **54**, 331.

[47] A. P. Alivisatos, Science 1996, **271**, 933.

[48] L. N. Lewis, Chem. Rev. 1993, **93**, 2693.

[49] H. M. Joshi, D. R. Bhumkar, K. Joshi, V. Pokharkar, M. Sastry, Langmuir, 2006, **22**,

300.

[50] A. Hagfeldt, M. Graetzel, Acc. Chem. Res. 2000, **33**, 269.

[51] J. Schoiswohl, G. Kresse, S. Surnev, M. Sock, M. G. Ramsey, F. P. Netzer, Phys. Rev. Lett. 2004, **92**, 206103.

[52] H. Zhang, J. F. Bandfield, J. Mater. Chem. 1998, **8**, 2073.

[53] Z. Song, T. Cai, Z. Chang, G. Liu, J. A. Rodriguez, J. Hrbek, J. Am. Chem. Soc. 2003, **125**, 8060.

[54] R. C. Cammarata, K. Sieradki, Phys. Rev. Lett. 1989, **62**, 2005.

[55] P. Ayyub, M. Multani, M. Barma, V. R. Palkar, R. Vijayaraghavan, J. Phys. C: Solid State Phys. 1988, **21**, 229.

[56] R. C. Garvie, M. F. Goss, J. Mater. Sci. 1986, **21**, 1253.

[57] C. N. R. Rao, G. U. Kulkarni, P. J. Thomas, P. P. Edwards, Chem. Eur. J., 2002, **8**, 29.

[58] C. Burda, X. Chen, R. Narayanan & M. A. El-Sayed, Chemical Reviews, 2005, **105**, 1025.

[59] M. Haruta, Catal. Today, 1997, **36**, 153.

[60] A. D. Yoffre, Advances in Physics, 1993, **42**, 173.

[61] E. Roduner, Nanoscopic materials:size dependent phenomena, The royal society of chemistry, Cambridge, 2006.

[62] H. Zeng, S. Sun, Adv. Funct. Mater., 2008, **18**, 391.

[63] N. Zhao, W. Nie, X. Liu, S. Tian, Y. Zhang, X. Ji, Small, 2008, **4**, 77.

[64] J. Gao, H. Gu, B. Xu, Acc. Chem. Res., 2009, **42**, 1097.

[65] J.-S. Lee, M. I. Bodnarchuk, E. V. Shevchenko, D. V. Talapin, J. Am. Chem. Soc., 2010, **132**, 6382-6391.

[66] P. Crespo, R. Litran, T. C. Rojas, et al., Phys. Rev. Lett., 2004, **93**, 087204.

[67] D. C. Lee, D. K. Smith, A. T. Heitsch, B. A. Korgel, Annual Reports Section "C" (Physical Chemistry), 2007, **103**, 351.

[68] L. E. Brus, J. Chem. Phys., 1983, **79**, 5566.

[69] G. D. Scholes, ACS Nano, 2008, **2**, 523.

[70] U. Kreibig, M. Volmer, Optical properties of metal clusters, Springr series in materials science, Springer, Berlin, 1995.

[71] M. Bruchez, M. Moronne, P. Gin, S. Weiss, A. P. Alivisatos, Science,1998, **281**, 2013.

[72] R. Seshadri, Oxide nanoparticles. Wiley-VCH Verlag GmbH & Co. KGaA, 2005.

[73] J. A. Rodríguez, M. Fernández-García, Synthesis, properties and applications of oxide nanoparticles, Whiley, New Jersey, 2007.

[74] P. V. Kamat, K. Tvrdy, D. R. Baker, J. G. Radich, Chemical Reviews, 2010, **110**, 6664.

[75] J. G. Lu, P. Chang, Z. Fan, Mater. Sci. Eng., R, 2006, **52**, 49.

[76] C. N. R. Rao,, A. Müller, A. K. Cheetham, Nanomaterials – An introduction, Wiley-VCH Verlag GmbH & Co. KGaA, 2005.

[77] S. Abbet, U. Heiz, Nanocatalysis, Wiley-VCH Verlag GmbH & Co. KGaA, 2005.

[78] Y. Z. Zhang, G. L. Wang, Mater. Lett., 2008, **62**, 673.

[79] A. F. Wells, Structural inorganic chemistry, Oxford: Clarendon Press, 1984.

[80] A. F. Holleman, E. Wiberg, Inorganic chemistry, Academic Press: San Diego, 2001.

[81] T. P. Gujar, V. R. Shinde, W. Y. Kim, K. D. Jung, C. D. Lokhande, O. Joo, Appl. Surf. Sci., 2008, **254**, 3813.

[82] R. Ferro, I. A. Rodriguez, Sol. Energy Mater. Sol. Cells, 2000, **64**, 363.

[83] M. Ristic, S. Poporic, S. Music, Mater. Lett., 2004, **58**, 2494.

[84] T. K. Subramanyam, S. Uthanna, N. B. Srinivasulu, Mater. Lett., 1998, **35**, 214.

[85] A. K. Srivastava, S. Pandey, K. N. Sood, S. K. Halder, R. Kishore, Mater. Lett., 2008, **62**, 727.

[86] Y. Dou, R. G. Egdell, D. S. L. Law, N. M. Harrison, B. G. Searle, J. Phys. Condens. Mater., 1998, **10**, 8447.

[87] Q. Chang, C. Chang, X. Zhang, H. Ye, G. Shi, W. Zhang, Y. Wang, X. Xin, Y. Song, Opt. Commun., 2007, **274**, 20.

[88] T. Kuo, M. H. Huang, J. Phys. Chem. B, 2006, **110**, 13717.

[89] X. S. Peng, X. F. Wang, Y. W. Wang, C. Z. Wang, G. W. Meng, L. D. Zhang, J. Phys. D: Appl. Phys., 2002, **35**, 1.

[90] H. B. Lu, L. Liao, H. Li, Y. Tian, D. F. Wang, J. C. Li, Q. Fu, B. P. Zhu, Y. Wu, Mater. Lett., 2008, **62**, 3928.

[91] A. M. Bazargan, S. M. A. Fateminia, M. E. Ganji, M. A. Bahrevar, Chem. Eng. J., 2009, **155**, 523.

[92] R. R. Salunkhe, D. S. Dhawale, U. M. Patil, C. D. Lokhande, Sens. Actuators B, 2009,

136, 39.

[93] B. S. Zou, V. V. Volkov, Chem. Mater., 1999, **11**, 3037.

[94] J. H. Kim, Y. C. Hong, H. S. Uhm, Jap. J. Appl. Phy., 2007, **46**, 4351.

[95] Z. W. Pan, Z. R. Dai, Z. L. Wang, Science, 2001, **291**, 1947.

[96] A. Askarinejad, A. Morsali, Mater. Lett., 2008, **62**, 478.

[97] F. Zhang, F. Bei, J. Cao, X. Wang, J. Solid State Chem., 2008, **181**, 143.

[98] Y. W. Wang, J. H. Liang, G. Z. Wang, J. Gao, S. X. Wang, J. C. Fan, L. D. Zhang, J. Mater. Sci. Lett., 2001, **20**, 1687.

[99] N. Varghese, L. S. Panchaakarla, M. Hanapi, A. Govindaraj, C. N. R. Rao, Mater. Res. Bull., 2007, **42**, 2117.

[100] R. B. Waghulade, P. P. Patil, R. Pasricha, Talanta, 2007, **72**, 594.

[101] C. Karunakaran, R. Dhanalakshmi, Cent. Eur. J. Chem., 2009, **7**, 134.

[102] C. Karunakaran, R. Dhanalakshmi, P. Gomathisankar, G. Manikandan, J. Hazard. Mater., 2010, **176**, 799.

[103] G. Fu, P. S. Vary, C. Lin, J. Phys. Chem. B, 2005, **109**, 8889.

[104] A. M. Thompson, Oxides of the rare earths, Wiley, New York, 1978.

[105] F. Zhang, P. Wang, J. Koberstein, S. Khalid, S.-W. Chan, Surf. Sci., 2004, **563**, 74.

[106] M. Fernández-García, A. Martínez-Arias, J. C. Hanson, J. A. Rodríguez, Chem. Rev. 2004, **104**, 4063.

[107] J. A. Rodriguez, X. Wang, J. C. Hanson, G. Liu, A. Iglesias-Juez, M. Fernández-García, J. Chem. Phys., 2003, **119**, 5659.

[108] A. Trovarelli, Catal. Rev. Sci.- Eng. 1996, **38**, 439.

[109] J. L. G. Fierro, J. Soria, J. Sanz, J. M. Rojo, J. Solid State Chem., 1987, **66**, 154.

[110] M. Shelef, G. W. Graham, Catal. Rev. Sci. Eng. 1994, **36**, 433.

[111] C. Korsvik, S. Patil, S. Seal, W. T. Self, Chem. Commun., 2007, **14**, 1056.

[112] J. Kašpar, P. Fornasiero, M. Graziani, Cat. Today, 1999, **50**, 285.

[113] M. Lira-Cantu, F. C. Krebs, Sol. Energy Mater. Sol. Cells, 2006, **90**, 2076.

[114] A. H. Morshed, M. E. Moussa, S. M. Bedair, R. Leonard, S. X. Liu, N. El-Masry, Appl. Phys. Lett., 1997, **70**, 1647.

[115] P. Kaminski, T. Suzuki, H. U. Anderson, Sensors Actuat B-Chem., 2003, **95**, 73.

[116] N. Kakuta, N. Morishima, M. Kotobuki, T. Iwase, T. Mizushima, Y. Sato, S. Matsuura, Appl. Surf. Sci., 1997, **121/122**, 408.

[117] H. Chen, H. Chang, Ceram. Int., 2005, **31**, 795.

[118] R. J. Qi, Y. J. Zhu, Y. H. Huang, Nanotechnology, 2005, **16**, 2502.

[119] P. Shuk, M. Greenblatt, Solid State Ion., 1999, **116**, 217.

[120] A. Bumajdad, M. I. Zaki, J. Eastoe, L. Pasupulety, Langmuir, 2004, **20**, 11223.

[121] T. Tsuzuki, J. S. Robinson, P. G. J. McCormick, J. Aust. Ceram. Soc., 2002, **38**, 15.

[122] Y. Wang, T. Mori, J. Li, T. Ikegami, J. Am. Ceram. Soc., 2002, **85**, 3105.

[123] E. L. Navarrete, A. Caballero, A. R. G. Elipe, M. Ocana, J. Mater. Res., 2002, **17**, 797.

[124] A. Hartridge, A. K. Bhattacharya, J. Phys. Chem. Solids, 2002, **63**, 441.

[125] M. Hirano, Y. Fukuda, H. Iwata, Y. Hotta, M. Inagaki, J. Am. Ceram. Soc., 2000,

83, 1287.

[126] C. W. Sun, H. Li, H. R. Zhang, Z. X. Wang, L. Q. Chen, Nanotechnology, 2005, **16**, 1454.

[127] N. N. Greenwood, A. Earnshaw, Chemistry of the elements, Oxford, Pergamon Press, 1984.

[128] A. H. Reidies, Manganese Compounds - Ullmann's encyclopedia of industrial chemistry, Weinheim, Wiley-VCH, 2002.

[129] G. Cahiez, M. Alami, R. J. K. Taylor, M. Reid, J. S. Foot, Manganese dioxide encyclopedia of reagents for organic synthesis, New York, J. Wiley & Sons, 2004.

[130] N. N. Greenwood, A. Earnshaw, Chemistry of the Elements, Oxford, Butterworth Heinemann, 1997.

[131] A. F. Wells, Structural inorganic chemistry, Oxford, Clarendon Press, 1984.

[132] E. Wiberg, A. F. Holleman, Inorg. Chem., Elsevier, 2001.

[133] P. Klocek, Handbook of infrared optical materials, CRC Press, 1991.

[134] R. Reisfeld, J. Alloys Compd., 2002, **341**, 56.

[135] Y. Wang, G. Meng, L. Zhang, C. Liang, J. Zhang, Chem. Mater., 2002, **14**, 1773.

[136] P. Xue, R. Lu, Y. Huang, M. Jin, C. Tan, C. Bao, Z. Wang, Y. Zhao, Langmuir, 2004, **20**, 6470.

[137] F. Wei, G. Li, Z. Zhang, J. Nanopart. Res., 2005, **7**, 685.

[138] P. Zhang, L. Gao, Langmuir, 2003, **19**, 208.

[139] K.-H. Schulte-Schrepping, M. Piscator, Cadmium and cadmium compounds in

Ullmann's Encyclopedia of industrial chemistry, Wiley-VCH, Weinheim, 2007.

[140] H. Zhao et al., Thin Solid Films, 2009, **517**, 2365.

[141] R. Smith, Phys. Rev., 1957, **105**, 900.

[142] R. Agarwal, C. J. Barrelet, C. M. Lieber, Nano Letters, 2005, **5**, 917.

[143] www.graphenea.com.

[144] W. S. Hummers, R. E. Offeman, J. Am. Chem. Soc., 1958, **80**, 1339.

[145] D. R. Dreyer, S. Park, C. W. Bielawski, R. S. Ruoff, Chem. Soc. Rev., 2010, **39**, 228.

[146] S. Stankovich, D. A. Dikin, G. H. B. Dommett, Nature, 2006, **442**, 282.

[147] B. C. Brodie, Philos.Trans. R. Soc. London, 1859, **14**, 249.

[148] L. Staudenmaier, Ber. Dtsch. Chem. Ges., 1898, **31**, 1481.

[149] D. C. Marcano, D. V. Kosynkin, J. M. Berlin, A. Sinitskii, Z. Sun, A. Slesarev, L. B. Alemany, W. Lu, J. M. Tour, ACS Nano, 2010, **4**, 4806.

[150] S. He, B. Song, D. Li, C. Zhu, W. Qi, Y. Wen, L. Wang, S. Song, H. Fang, C. Fan, Adv. Funct. Mater., 2010, **20**, 453.

[151] F. Perrozzi, S. Prezioso, M. Donarelli, F. Bisti, P. D. Marco, S. Santucci, M. Nardone, E. Treossi, V. Palermo, L. Ottaviano, J. Phys. Chem. C, 2013, **117**, 620.

[152] G. Eda, M. Chhowalla, Adv. Mater., 2010, **22**, 2392.

[153] K. Erickson, R. Erni, Z. Z. Lee, N. Alem, A. W. Gannett, A. Zettl, Adv. Mater., 2010, **22**, 4467.

[154] K. S. Novoselov, A. K. Geim, S. V. Morozov, D. Jiang, Y. Zhang, S. V. Dubonos, I.

V. Grigorieva, A. A. Firsov, Science, 2004, **306**, 666.

[155] A. K. Geim, K. S. Novoselov, Nat. Mater., 2007, **6**, 183.

[156] K.S. Novoselov, Z. Jiang, Y. Zhang, S. V. Morozov, H. L. Stormer, U. Zeitler, et al., Science, 2007, **315**, 1379.

[157] K. I. Bolotin, K. J. Sikes, Z. Jiang, M. Klima, G. Fudenberg, J. Hone, et al., Solid State Commun., 2008, **146**, 351.

[158] C. G. Lee, X. D. Wei, J. W. Kysar, J. Hone, Science, 2008, **321**, 385.

[159] A. A. Balandin, S. Ghosh, W. Bao, I. Calizo, D. Teweldebrhan, F. Miao, et al., Nano Lett., 2008, **8**, 902.

[160] Q. Y. He, H. G. Sudibya, Z. Y. Yin, et al., ACS Nano, 2010, **4**, 3201.

[161] S. Pei, H.-M. Cheng, Carbon, 2012, **50**, 3210.

[162] A. Geim, Science, 2009, **324**, 1530.

[163] S. Hong, E. S. Kim, W. Kim, S.-J. Jeon, S. C. Lim, K. H. Kim, et al., Phys. Chem. Chem. Phys. 2012, **14**, 13527.

[164] S. Bae, H. Kim, Y. Lee, X. Xu, J.-S. Park, Y. Zheng, et al., Nat. Nanotechnol. 2010, **5**, 574.

[165] S. Biswas, L. T. Drzal, Chem. Mater. 2010, **22**, 5667.

[166] J. R. Lake, A. Cheng, S. Selverston, J. Koehne, M. Meyyappan, B. Chen, J. Vac. Sci. Technol. B, 2012, **30**, 03D118.

[167] Z. Wang, J. K. Nelson, H. Hillborg, S. Zhao, L. S. Schadler, Adv. Mater., 2012, **24**, 3134.

[168] T. Ramanathan, A. A. Abdala, S. Stankovich, D. A. Dikin, M. Herrera-Alonso, R. D. Piner, Nat. Nanotechnol., 2008, **3**, 327.

[169] S. Stankovich, D. A. Dikin, G. H. B. Dommett, K. M. Kohlhaas, E. J. Zimney, E. A. Stach, et al., Nature, 2006, **442**, 282.

[170] Y.-H. Yang, L. Bolling, M. A. Priolo, J. C. Grunlan, Adv. Mater., 2013, **25**, 503.

[171] W. Hung, C. Tsou, M. De Guzman, Q. An, Y. Liu, Y. Zhang, C. Hu, K. Lee, J. Lai, Chem. Mater., 2014, **26**, 2983.

[172] J. Liang, Y. Xu, Y. Huang, L. Zhang, Y. Wang, Y. Ma, et al., J. Phys. Chem. C, 2009, **113**, 9921.

[173] W. Zhang, Z. Guo, D. Huang, Z. Liu, X. Guo, H. Zhong, Biomaterials, 2011, **32**, 8555.

[174] C.-H. Lu, C.-L. Zhu, J. Li, J.-J. Liu, X. Chen, H.-H. Yang, Chem. Commun., 2010, **46**, 3116.

[175] T. Xue, B. Peng, M. Xue, X. Zhong, C.-Y. Chiu, S. Yang, et al., Nat. Commun., 2014, **5**, 3200.

[176] X. Huang, X. Qi, F. Boey, H. Zhang, Chem. Soc. Rev., 2012, **41**, 666.

[177] G. Eda, M. Chhowalla, Nano Lett., 2009, **9**, 814.

[178] Z. Yin, S. Wu, X. Zhou, X. Huang, Q. Zhang, F. Boey, H. Zhang, Small, 2010, **6**, 307.

[179] X. Zhou, X. Huang, X. Qi, S. Wu, C. Xue, F. Y. C. Boey, Q. Yan, P. Chen, H. Zhang, J. Phys. Chem. C, 2009, **113**, 10842.

[180] C. Nethravathi, T. Nisha, N. Ravishankar, C. Shivakumara, M. Rajamathi, Carbon, 2009, **47**, 2054.

[181] Y. T. Kim, J. H. Han, B. H. Hong, Y. U. Kwon, Adv. Mater., 2010, **22**, 515.

[182] J. Huang, L. Zhang, B. Chen, N. Ji, F. Chen, Y. Zhang, Z. Zhang, Nanoscale, 2010, **2**, 2733.

[183] L. Shao, S. Quan, Y. Liu, Z. Guo, Z. Wang, Mater. Lett., 2013, **107**, 307.

[184] X. Liu, L. Pan, Q. Zhao, T. Lv, G. Zhu, T. Chen, T. Lu, Z. Sun, C. Sun, Biochem. Eng. J., 2012, **183**, 238.

[185] Y. Yang, L. Ren, C. Zhang, S. Huang, T. Liu, ACS Appl. Mater. Interfaces, 2011, **3**, 2779.

[186] S. Chen, J. Zhu, X. Wu, Q. Han, X. Wang, ACS nano, 2010, **4**, 2822.

[187] M. Bruchez Jr., M. Moronne, P. Gin, S. Weiss, A. P. Alivisatos, Science, 1998, **281**, 2013.

[188] Z. Xu, F. S. Xiao, S. K. Purnell, O. Alexeev, S. Kawi, S. E. Deuth, B. C. Gates, Nature, 1994, **372**, 346.

[189] V. L. Colvin, M. C. Schlamp, A. P. Alivisatos, Nature, 1994, **370**, 354.

[190] B. O. Dabbousi, M. G. Bawendi, O. Onitsuka, M. F. Rubner, Appl. Phys. Lett., 1995, **66**, 1316.

[191] D. L. Klein, R. Roth, A. K. L. Lim, A. P. Alivisatos, P. L. McEven, Nature, 1997, **389**, 699.

[192] T. Nakahara, T. Imai, Frontier nanotechnology for the next generation, John wiley &

sons, 2005.

[193] M. Aliofkhazraei, C. Morillo, R. Miresmaeili, A. S. Rouhaghdam, Surf. Coat. Technol., 2008, **202**, 5493.

[194] B. Karn, T. Kuiken, M. Otto, Environ. Health Perspect., 2009, **117**, 1823.

[195] X. Qu, P. J. Alvarez, Q. Li, Water Res., 2013, **47**, 3931.

[196] R. M. Zadegan, M. L. Norton, .Int. J. Mol. Sci., 2012, **13**, 7149.

[197] P. Boisseau, B. Loubaton, Comptes Rendus Physique, 2011, **12**, 620.

CHAPTER - 2

Synthesis methods and characterization techniques

In this chapter, an overview of different synthesis methods such as; co-precipitation, sol-gel and solvothermal/hydrothermal used for the synthesis of nanostructured materials of different shapes and sizes have been given. Further, a brief description of various characterization techniques such as; X-ray diffraction (XRD), ultraviolet-visible (UV-VIS) spectroscopy, photoluminescence (PL) spectroscopy, Raman spectroscopy (RS), transmission electron microscopy (TEM), scanning electron microscopy (SEM), vibrating sample magnetometer (VSM) used for characterizing the synthesized products have also been given in the present chapter. The details of photocatalytic and antimicrobial activities measurements of some synthesized nanostructured materials have also been given in somewhat more detailed in this chapter.

2.1 Introduction

In order to manipulate the materials at nanoscale range for getting desired shape and size and to utilize their size and shape dependent properties, the synthesis methods used in the synthesis process play an important role to control the growth of nanostructured materials. In this regard, major success have been achieved today with the help of expanding horizons of nanotechnology, which always demands new protocols for the synthesis of nanostructures of different sizes and shapes [1]. The scientists are usually applying either "top-down or "bottom-up" approach for the synthesis of nanostructures. The top-down approach mainly involves physical methods like lithography, milling and sputtering etc. In the top-down approach, nanostructures are synthesized by breaking down of bulk material into small segments till the desired size and shape is achieved. The bottom-up approach mainly involves chemical methods like co-precipitation, sol-gel and hydrothermal/solvothermal. In the bottom up approach, nanostructures are synthesized by assembling basic units of the materials into larger structures [2]. Due to limited success and high cost of physical methods, chemical methods are comparatively cost effective, and easy for the synthesis of nanostructures. As we know that the properties of nanostructured materials are very sensitive to size and shape, therefore, the synthesis methods through which one can have the controlled over the growth on shape and size of the nanostructures of metals, metal oxides, metal sulfides and its composites with various morphologies at large scale have been the subject of immense research interest [3]. In chemical method of synthesis, different capping agents and solvents are used to control the size, shape and

stability of nanostructures for its various applications [4].

In this chapter, an overview of synthesis methods and characterization techniques used to study the nanostructures has been presented. In the entire research work, co-precipitation, sol-gel and solvothermal/hydrothermal methods of synthesis were used for synthesizing the desired shape and size of the nanostructures. Structural and morphological characterizations of the nanostructured materials were done through X-ray diffraction (XRD), transmission electron microscopy (TEM) and scanning electron microscopy (SEM) measurements. Optical properties of the synthesized nanostructures were studied by ultraviolet-visible (UV-VIS) spectroscopy, photoluminescence (PL) spectroscopy and Raman spectroscopy (RS) measurements. Magnetic properties of the synthesized nanostructured materials were done with the help of vibrating sample magnetometer (VSM) measurements. Besides the synthesis and characterizations, some possible applications such as; antimicrobial and photocatalytic activities of the synthesized nanostructures have also been investigated.

2.2 Synthesis Methods

2.2.1 Co-precipitation method

Co-precipitation is a facile and convenient chemical method to synthesize nanostructures of desired shapes and sizes. This method has been mostly used to synthesize metal oxide based nanostructures. Usually, in this method, the aqueous solutions of the metal salts are mixed in the appropriate ratio and the co-precipitation of the product could be obtained by hydrolysis process by keeping the solvent medium basic in nature in the presence/absence

of inert atmosphere at room temperature or elevated temperature [5-6]. In this method, it is crucial to control the factors such as the ratio of metal salts, reaction temperature, pH value, type of salts and ionic strength of mixed solution that determine the precipitation process to make desired size and shape of the materials. Careful control of precipitation kinetics can result in monodispersed and narrow size distribution of the nanostructures [7]. After controlling the above mentioned factors during the synthesis process, co-precipitation of various salts such as; nitrates, acetates, sulphates and chlorides yields different types of nanostructures with narrow size distributions of various materials such as; ZnO, SnO_2, MnO_2, and CdS etc for various applications such as; catalysis, energy storage, optoelectronics and sensing etc. Due to the low cost, simple and easy to control the different parameter for getting the desired shape and size of the nanostructures, the co-precipitation method has widely been used to synthesize simple and more complicated nanostructures such as; core-shell and nanocomposites [8].

2.2.2 Sol-gel method

In general, the sol-gel process is used to synthesize the nanostructures of inorganic non-metallic materials from solutions precursor [9]. The sol-gel process consists of four different steps: (i) hydrolysis, (ii) poly-condensation, (iii) drying, and (iv) thermal decomposition [8]. At first step, the precursors are dissolved in a suitable liquid (usually water for the colloidal route and alcohol for the polymeric route) to make colloidal solution, called sol. The size of the sol particles mainly depends on several factors such as; composition of the solution, pH, and temperature at which reaction is occured. The sol is

then treated by the addition of an acid or a base which further react with each other to form a network of solid material. The network grows and ages with time and temperature and the viscosity of the liquid solution is increased at an exponential rate until gelation process occurs. Once the mixed solution has been condensed to a gel, the solvent must be removed by washing followed by drying. Thereafter, the obtained product is calcined at higher temperature to make final product. By controlling above mentioned factors during synthesis, the size of the particles can be tuned to the nanoscale range. This synthesis method has been used to prepare nanomaterials in different forms for its applications in different areas of science and technology. The advantages of sol-gel method of synthesis over other synthesis method are its low synthesis temperature, high purity, novel material and low investment. This method has mainly been used to synthesize various shapes and sizes of TiO_2, CeO_2, ZrO_2, SnO_2, ZnO, CdS and other oxide based nanostructures [10-11].

2.2.3 Hydrothermal/solvothermal method

Hydrothermal method of synthesis is a commonly used synthesis method to synthesize nanostructures of different sizes and shapes. The word hydrothermal has originated from Greek words ‘hydros’ meaning water and ‘thermos’ meaning heat. Hydrothermal synthesis can be defined as the occurrence of heterogeneous reaction in the presence of aqueous solvents under high pressure and temperature to dissolve and re-crystallize the materials which is insoluble under ordinary conditions [12]. The hydrothermal process is carried out in a sealed Teflon lined stainless steel autoclave that can hold up at high temperature and pressure for a long time. The mixed solution consisting of solvent, precursors and acidic or

basic medium placed into an autoclave. The loaded mixture in autoclave is then heated at the desired temperature. A temperature gradient is maintained at both the ends of growth chamber so that the hotter end dissolves the loaded material and the cooler end causes seeds to take additional growth. The precursor materials transform to the stable compound due to elevated temperature of water since the structure of water at elevated temperatures is different than that of the ambient temperature. In addition, the properties of precursor materials such as; solubility and reactivity are also changed at high temperature. After cooling the autoclave, the final product can be isolated by filtration and after washing several times with water [13]. During the synthesis, different parameters such as, stoichiometries amount of reactants, pH of the reacting solution, temperature, pressure and reaction time play a vital role to maintain homogeneous nucleation rate and narrow size distribution with desired shapes and sizes [14]. Different types of oxides and sulfides based nanostructures such as; TiO_2, $LaCrO_3$, ZrO_2, $BaTiO_3$, $SrTiO_3$ and PbS of various shapes and sizes have been successfully synthesized by this method [10-11]. Further, when polar and non-polar solvents such as; alcohol, benzene etc. are used in synthesis in place of water then this method is called solvothermal synthesis. The advantages of hydrothermal method of synthesis over any other chemical methods of synthesis are manufacturing of high crystallinity, less defects fine powders with controlled morphology and high purity. A digital photograph of the Teflon lined stainless steel autoclave used in the present study is given in Fig. 2.1.



Fig. 2.1 Digital photograph of Teflon lined stainless steel autoclave.

2.3 Characterization Techniques

2.3.1 X-ray diffraction (XRD)

XRD is a versatile tool for structural characterization of the materials. This technique has extensively been used to determine the crystalline phase of the solid materials. The phase formation, lattice constant, inter planar spacing and crystallize size of the synthesized samples were investigated by performing the XRD measurements at room temperature. The XRD measurements on powder samples were performed with the Rigaku Smart Lab equipped with Cu-Kα radiation (λ = 1.54 Å) operated at 20 - 60 kV and 2 - 60 mA. Samples were scanned in the angle range of 10-80^{o} with a scanning rate of 0.1 (degree) / min. The recorded diffraction pattern is composed of characteristic peaks at specific angles. The peak position, full width at half maximum (FWHM) and intensity of specific peak provides the information about the phase, crystallite size and crystallinity with details of crystal planes. A digital photograph of X-ray diffractometer is presented in Fig. 2.2.



Fig. 2.2 Digital photograph of X-ray diffractometer.

2.3.2 Ultraviolet-visible (UV-VIS) spectroscopy

UV-VIS spectroscopy is an important tool to study the optical properties of the materials. This technique has been extremely useful in studying optical properties of low dimension systems due change in electronic properties of the materials at nanoscale range. The UV-VIS spectra of the synthesized samples were recorded in the spectral range of 200-800 nm using PerkinElmer (Lambda35) UV-VIS spectrometer. UV-VIS spectra were used to calculate the optical band gap and the nature of electronic transition. The UV-VIS spectra of the synthesized samples were measured by dispersing the powder samples in solution.

The details of the measurements have also been given in the experimental section of the respective chapter. This instrument can be used to record the UV-VIS spectra in liquids, solids, pastes and powder samples. The variable bandwidth operation allows sensitive measurements with accessories such as integrating spheres and fiber optic cables. A digital photograph of UV-VIS spectrometer is given in Fig. 2.3.



Fig. 2.3 Digital photograph of UV-VIS spectrometer.

2.3.3 Photoluminescence (PL) spectroscopy

The PL spectroscopy is an experimental technique which has been used to study the emission behavior of bulk and low dimension systems. The PL measurements of the synthesized samples were performed using a PerkinElmer (LS-55) Fluorescence Spectrometer. The emission range for the spectra which can be recorded using this instrument is 200 – 900 nm at the spectral resolution of 1 nm. Excitation and emission slit width (spectral band width) used in this experiment is fixed at 5 nm. The emission spectra of the synthesized samples were recorded in powder as well as in solution form. The

details of the PL measurements of the synthesized samples have been presented in the experimental section of the respective chapter. The samples were excited by radiation of 320 nm wavelength and emission spectra were recorded in the spectral range of 350-550 nm. A digital photograph of PL spectrometer is given in Fig. 2.4.



Fig. 2.4 Digital photograph of PL spectrometer.

2.3.4 Raman spectroscopy (RS)

RS is a non destructive and very useful experimental tool to study the optical as well as structural properties of the bulk as well as nanomaterials. Since the Raman scattering is originated from the molecular level, it has been widely used to characterize the nanomaterials of different shapes and sizes. Due to confinement of phonon in low dimension systems, the Raman features of low dimension materials are observed to be different than that of its bulk form of the materials. The Raman spectra of the synthesized products were recorded at room temperature in the spectral range 200-1200 cm^{-1} using a Renishaw invia Raman spectrometer. It is equipped with a microscope and a high-

performance CCD detector. The 514 nm line of argon-ion laser was used to illuminate the sample. The other experimental details of the Raman measurements have been given in the experimental section of the corresponding chapter. For recording the Raman spectra of the samples, 180° scattering geometry was used. A digital photograph of Raman spectrometer is illustrated in Fig. 2.5.



Fig. 2.5 Digital photograph of Raman spectrometer.

2.3.5 Transmission electron microscope (TEM)

TEM is one of the most powerful and useful tools to characterize the shape and size of the nanostructured materials. The TEM has been extensively used to determine the shape, size, crystalline phase, growth direction of crystal plane and surface structure of the low dimension systems. The shape and size of the nanostructures are determined by imaging of synthesized products. The size, shape and inter-planar spacing of the nanostructures were analyzed by high resolution transmission electron microscopy (HR-TEM) (TEM, Tecnai G20 S-Twin). The HR-TEM instrument was equipped with an ultra-high resolution

objective lens and was operated at an accelerating voltage of 80 kV. To perform the measurements, 2 mg of powder sample was dispersed in ethanol by sonication for 1h and one drop of the well-dispersed sample solution was deposited on to a carbon coated copper grid having 400 mesh/mm. The dried grid was used for HR-TEM measurements. Selective area electron diffraction (SAED) pattern can be obtained by TEM measurements when a selected-area aperture is used to determine inter-planar spacing of corresponding plane. The other details of the TEM measurements of the synthesized products have been given in the corresponding chapter. A digital photograph of TEM is presented in Fig. 2.6.



Fig. 2.6 Digital photograph of Transmission electron microscope.

2.3.6 Scanning electron microscope (SEM)

SEM is an important tool to characterize the low dimension systems. This technique has been widely used to characterize the structural morphology and surface analysis of the nanostructured materials. The most important use of this technique in nanoscience and technology is to determine the presence of different elements in nanostructured materials especially to the nanocomposite materials. Surface morphologies of the synthesized samples were studied using FE-SEM (SIRIDN 2000) and SEM (FEI QUANTA-200 MK2). Before SEM measurements, samples were coated with gold. A working distance of 10 mm was maintained and a 15 kV acceleration voltage was used to perform the measurements. The details of the measurement can be found in the experimental section of the corresponding chapter. A digital photograph of SEM is given in Fig. 2.7.

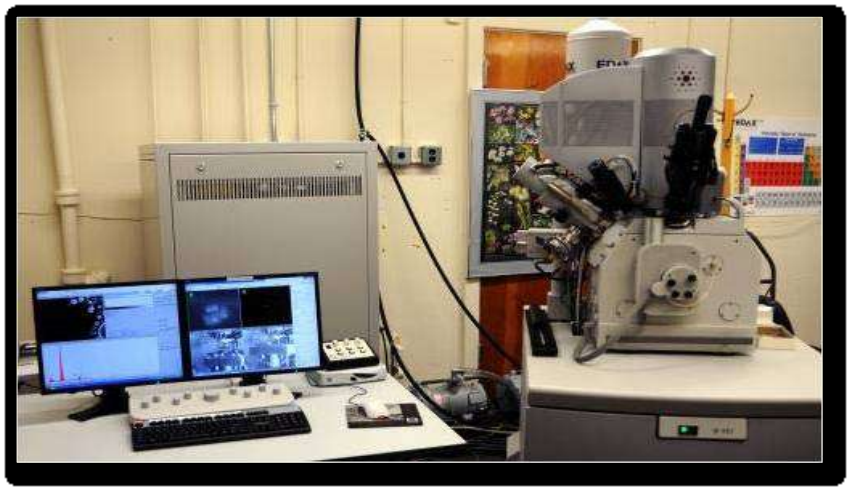


Fig. 2.7 Digital photograph of scanning electron microscope.

2.3.7 Vibrating sample magnetometer (VSM)

The VSM has become a widely used instrument to determine magnetic properties of a

large variety of materials such as; diamagnetic, paramagnetic, ferromagnetic, anti-ferromagnetic and ferrimagnetic. It has a flexible design and combines high sensitivity with simplicity of sample mounting and exchange. The magnetic properties of the synthesized samples were measured at room temperature by the means of VSM (ADE-DMS, model EV-7USA) at maximum applied field of 17.5 KOe. A small amount of powder ~ 10 mg was put in the butter paper and makes it tight to avoid the movement of sample inside the sample holder. All important magnetic parameters are determined by analyzing magnetization vs applied magnetic field curve. The magnetic moment, coercivity, retentivity, and saturation magnetization have been calculated with the help of M-H loop of the samples. A digital photograph of VSM is given in Fig. 2.8.



Fig. 2.8 Digital photograph of vibrating sample magnetometer.

2.4 Photocatalytic Activity

The photocatalytic activity of any material, used as a catalyst, is the ability of the catalyst to generate electron–hole pairs after irradiation of light. These photogenerated electron–hole pairs create free radicals such as; hydroxyl radicals and •OH. These radicals have ability to undergo for secondary reactions and resulting the degradation of organic pollutants. For the occurrence of photocatalysis, the incident photon should have energy equal to or greater than the catalyst material. Upon irradiation of light, a photon is absorbed by the catalyst and an electron is excited from the valence band (VB) to the conduction band (CB), generating a positive hole in the valence band. The main goal of this process is to make a reaction between the generated holes with OH^- (present in the aqueous solution) to produce hydroxyl radicals (·OH) and also a reaction between the excited electrons with dissolved O_2 molecules to produce oxygen peroxide radical $O_2^{\bullet -}$. These radical ions degrade the organic pollutants into small molecules such as; CO_2 and H_2O [15].

The degradation mechanism of long molecules into small molecules by addition of catalyst can be understood by going through the following steps:

$$\text{Catalyst material} + h\nu\ (E > Eg) \rightarrow \text{Catalyst material}\ [h^+\ (VB) + e^-\ (CB)]$$

$$O_2 + e^-\ (CB) \rightarrow O_2^{\bullet -}$$

$$H_2O + h^+ \rightarrow H^+ + OH^-$$

$$OH^- + h^+\ (VB) \rightarrow \cdot OH$$

$$\text{Organic pollutants} + \cdot OH + O_2^{\bullet -} \rightarrow CO_2 + H_2O + \ldots\ldots \text{ etc.}$$

In order to study the photocatalytic properties of the synthesized samples over organic pollutants under desired light irradiation, the aqueous solution of organic pollutants mixed with suitable catalyst is prepared. The obtained dispersed aqueous solution was stirred in the dark for 30 min to achieve the adsorption equilibrium. The solution is exposed to light of desired wavelength for a fixed time. After a fixed interval of time, the solution is taken out from the light chamber to record UV-VIS absorption spectra and determine the residual concentration of organic pollutants by analyzing the intensity of absorption peak appeared in the UV-VIS spectra.

2.5 Antimicrobial Activity

Nanostructures have high surface to volume ratio with reactive components on the surface. The size and shape of the nanostructures are generally responsible for generating reactive oxygen species, at the nanostructured surfaces that damage the microbial or cell membrane lipids and damage to the DNA, which ultimately leads to death to the microbes or cell when the nanoparticles are brought closer to these biological species. Thus, one of the most important applications of nanostructured materials in biology is to prevent the growth of bacteria. Thus, the nanostructured materials are also known to have good antimicrobial activity.

The Modified Bauer-Kirby disc diffusion method [16] was followed to study antimicrobial activity of synthesized samples. Microbial culture of 106 Colony forming Unit (CFU) for analysis was fresh prepared from stock solution. Microbes were inoculated in sterilized and autoclaved Muller hinton broth (MHB). Further, 15 gm of MHB was

dissolved in 500 ml of distilled water, pH 7.0 and incubated for 24 hours at 28±2 ◦C in an incubator shaker at 120 rpm. Plates were got ready of Muller Hinton Agar (MHA) to check the antimicrobial activity of filter paper disc coated with silver solution of nanorods with different aspect ratios. The size of each disc was fixed to 8 mm. The disc is made from sterilized filter paper. These discs were then impregnated with 20 µl synthesized samples solution and were placed onto MHA plates made up of autoclaved MHA media. These plates were then incubated overnight at 28±2 ◦C and the zone of inhibition around the discs was measured. The large zones of inhibition around each disc indicated susceptibility of microbe toward synthesized samples while small zones or no zones of inhibition indicated resistive microbes. Minimum inhibitory concentrations (MIC) and minimum bactericidal concentration (MBC) of synthesized samples has been studied against B.subtilis (gram+ve) and E.coli (gram-ve) microbes. The details of the antimicrobial measurements of the nanostructured materials over B.subtilis (gram+ve) and E.coli (gram-ve) microbes have been well described in the experimental section of the corresponding chapter.

References

[1] I. Yamada, J. Matsuo, N. Toyoda, A. Kirkpatrick, Mater. Sci. Eng. R, 2001, **34**, 231.

[2] H. S. Nalwa, Handbook of nanostructured materials and nanotechnology, Academic Press, 2000.

[3] J. Park, J. Joo, S. G. Kwon, Y. Jang, T. Hyeon, Angew. Chem. Int. Ed., 2007, **46**, 4630.

[4] D. C. Lee, D. K. Smith, A. T. Heitsch, B. A. Korgel, Annual Reports Section "C" (Physical Chemistry), 2007, **103**, 351.

[5] M. Santiago, M. S. Yalfani, J. P. Ramırez, J. Mater. Chem., 2006, **16**, 2886.

[6] T. Nedkov, L. Merodiiska, R. E. Slavov, Y. Vandenberghe, J. Kusano, J. Takada, J. Magn. Magn. Mater., 2006, **300**, 358.

[7] Y. Kima, D. Kima, C. S. Lee, Physica B, 2003, **337**, 42.

[8] C. Burda, X. Chen, R. Narayanan, M. A. El-Sayed, Chem. Rev., 2005, **105**, 1025.

[9] S. M. Attia, J. Wang, G. Wu, J. Shen, J. Ma, J. Mater. Sci. Technol., 2002, **18**, 211.

[10] G. Cao, Nanostructures and nanomaterials: synthesis, properties and applications, Imperial College Press, London, 2004.

[11] E. Wolf, Nanophysics and nanotechnology, Wiley-VCH, Weinheim, 2004.

[12] K. Byrappa, T. Adschiri, Prog. Cryst. Growth Ch., 2007, **53**, 117.

[13] L. N. Demianets, Prog. Cryst. Growth Ch., 1991, **21**, 299.

[14] M. I. Khan, E. Yohannes, S. Ayesh, R. J. Doedens, J. Mol. Struct., 2003, **656**, 45.

[15] N. Serpone, E. Pelizzetti, Photocatalysis, fundamentals and applications, Wiley Interscience, New York, 1989.

[16] A. W. Bauer, W. M. Kirby, J. C. Sherris, M. Turck, Am. J. Clin. Pathol., 1966, **45**, 493.

CHAPTER - 3

Synthesis, characterization and antimicrobial activities of well dispersed ultra-long cadmium oxide nanowires

In this chapter, a simple, efficient and low cost method for preparation of well dispersed ultra-long (1μm) cadmium oxide (CdO) nanowires has been presented. The CdO nanowires were characterized by X-ray diffraction (XRD), transmission electron microscopy (TEM), ultraviolet-visible (UV-VIS) and Raman spectroscopic measurements. The values of direct and indirect optical band gap were calculated to be 3.5 eV and 2.6 eV, respectively. In the Raman spectra, only second order features were observed. The antimicrobial activities of synthesized CdO nanowires were investigated against both, B.subtilis and E.coli microbes. It has been found that the CdO nanowires exhibit antimicrobial activity against both, B.subtilis and E.coli microbes. However, the strength of antimicrobial activity of nanowires was found to be better against B.subtilis than that of E.coli microbes.

3.1 Introduction

Over the past two decades, the controlled growth of one dimensional nanostructure such as, nanowires, nanorods, nanotubes and nanobelts have been the subject of intense research due to their novel size and shape dependent physical and chemical properties [1, 2]. The size and shape dependent properties of the materials are expected to play critical role in the development of new electronic, optoelectronic and biotechnological devices [1-3]. There has been increasing interest in developing simple synthesis methods and investigating the size and shape dependent properties of oxide based semiconductor materials such as; CeO_2 [4], CdO [5], ZnO [6] and SnO_2 [7]. Recently, CdO nanostructure has attracted immense research interest due its application in solar cells [8] flat-panel display [9] and developing sensing devices [10]. It is an important n-type semiconductor with a direct band gap of 2.3 eV and an indirect band gap of 1.36 eV [11]. One dimensional CdO nanostructures have been synthesized and well studied by various research group [12-13]. However, in the reported studies, the synthesis methods were involved many steps and also these methods did not yield well dispersed ultra-long nanowires. Thus, a combined report on synthesis, optical studies and antimicrobial activities of well dispersed CdO nanowires on B.subtilis and E.coli microbes is still lacking in the literature.

Here, a simple, low cost and template free method for the preparation of ultra-long CdO nanowires. XRD, TEM and Raman spectroscopy measurements were used to characterize the synthesized product. The band gap of synthesized product was determined using UV-VIS spectroscopy measurements and their antimicrobial activities against

B.subtilis (gram positive) and E.coli (gram negative) microbes were also investigated.

3.2 Experimental Techniques

3.2.1 Synthesis

CdO nanowires have been synthesized at room temperature by simple and low cost chemical method using $Cd(CH_3COO)_2 \cdot 2H_2O$ and ammonia solution 25% (0.91) as starting materials. The synthesis method reported in the present study is relatively simple than that of reported in the earlier studies [13-14]. All chemicals were used without further purification. For the synthesis of CdO nanowires, the appropriate amount of $Cd(CH_3COO)_2 \cdot 2H_2O$ (0.5 M) as solute, 100 mL distilled water as solvent and ammonia solution was taken. $Cd(CH_3COO)_2 \cdot 2H_2O$ was dissolved in distilled water under gently stirring for half an hour with a Teflon-coated magnetic bar and then ammonia solution was added to above solution drop wise until desired pH is reached with constant stirring for another few hours. The white precipitate of $Cd(OH)_2$ after hydrolysis was formed inside the solution and it was kept overnight without stirring. Next day, the solution was filtered with Whatman filter paper of 125 mm and washed 5-6 times with distilled water. The obtained precipitate was dried at 60 ◦C overnight. The resulting powder after grinding was calcined at 400 ◦C for 2 hours. After calcination, the obtained powder was turned into reddish brown color, which confirms the formation of final product. The CdO structure may be formed according to following reaction:

$$Cd(CH_3COO)_2 \cdot 2H_2O + 2NH_4OH \rightarrow Cd(OH)_2 + 2H_2O + 2CH_3COONH_4$$

During calcination at 400 ˚C, the prepared powder samples lose H_2O molecules according

to the following equation:

$Cd(OH)_2 \rightarrow CdO + H_2O$

3.2.2 Characterization

The crystalline features of the synthesized products have been probed by powder XRD using Rigaku Smart Lab X-ray diffractometer with CuKα radiation (λ = 1.54 Å). The detailed structure of the products was further investigated through TEM (TEM, Tecnai G20 S-Twin) consisting of a tungsten filament. UV-VIS spectrum of the product dispersed in ethanol was recorded in the spectral range of 200-800 nm using PerkinElmer (Lambda35) UV-VIS spectrometer. Room temperature Raman spectrum was recorded in the spectral range of 200-1300 cm^{-1} (Renishaw invia Raman spectrometer). The samples were illuminated by 514 nm wavelength using the Argon-ion laser. In addition, antimicrobial activity of the synthesized samples was studied using Modified Bauer-Kirby disc diffusion method.

3.3 Results and Discussion

3.3.1 XRD and TEM

As synthesized powder samples was characterized by powder X-ray diffractometer. The measurements were carried out with Cu Kα (λ = 1.54 Å) incident radiation. Fig. 3.1a shows the XRD pattern of the synthesized product. The diffraction peaks observed at 2θ values match nicely with the reference patterns of (JCPDS File No. 73-2245) (111), (200), (220), (311) and (222) planes corresponding to cubic structure of CdO. It is clearly seen from Fig. 3.1a that all diffraction peaks correspond to cubic structure of CdO and no any

other peaks related to the impurities were detected, which further confirms that the synthesis procedure adopted in the present study yields impurity free CdO. The (111) peak (2θ = 32.98◦) has highest intensity. This indicates that the CdO structure is grown in the (111) preferred direction. The lattice parameters were calculated using matched hkl values and the value of 'a' was calculated to be a = 4.69 Å, which is in good agreement with the value reported in earlier study [5]. In order to determine the shape and size, the synthesized CdO powder samples was further investigated using TEM. Fig. 3.1b-d shows the TEM micrographs of CdO powder sample taken at different magnifications. The Fig. 3.1b clearly shows well dispersed wire type of structure of average length ~ 1 μm and width ~ 15 nm. The TEM images taken at higher magnification are shown in Fig. 3.1c and 3.1d. It clearly reveals that the nanowires are straight with smooth surfaces.

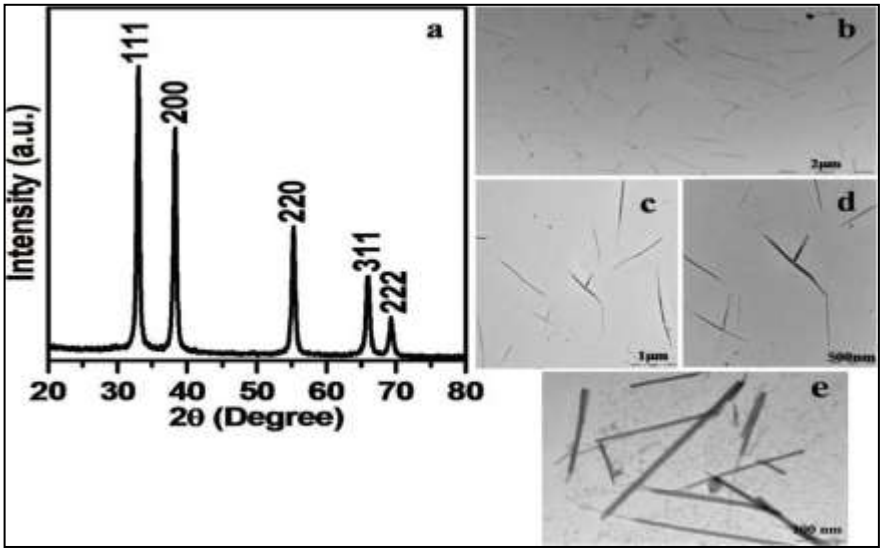


Fig. 3.1 XRD pattern of (a) CdO nanowires (b-e) TEM micrographs of CdO nanowires taken at different magnifications.

3.3.2 UV-VIS spectroscopy

The UV-VIS absorption spectroscopy is a useful characterization technique to analyze and determine the value of optical band gap. UV-VIS absorption spectrum recorded for spectral range 200-800 nm of as synthesized CdO nanowires is shown in Fig. 3.2a. The absorption spectrum shows two absorption bands ~ 350 and ~ 463 nm. The absorption between 250 and 350 nm may be due the ligand-to-metal charge-transfer transitions and less contribution comes from the Cd^{2+} ligand field transitions. However, the absorption occurs between 400-600 nm is assigned to the pair excitation process 6A1 + 6A1 → 4T1 + 4T1 and partly overlapping the contributions of the ligand field transitions [15]. Further, it may also be due to the fact that in case of nanostructures, the size and shape causes to increase the surface to volume ratio, which ultimately create states at different energies in the forbidden gap and thereby it allow some finite transition probabilities from these developed states [16]. The UV-VIS data are used to estimate the optical band gap of CdO nanowires. In order to calculate the band gap from observed absorption spectrum, we have plotted $(\alpha h\nu)^2$ vs. hν and the curve thus obtained is shown in Fig. 3.2b. The value of band gap is calculated by extrapolating the linear part up to zero on energy axis, which provides the value of direct band gap. The extrapolated line intercepts to energy axis at 3.5 eV. Thus, the value of direct band gap is found to be 3.5 eV. This value is almost ~ 1.3 eV larger compared to their value in bulk form [11] and ~ 1 eV larger compared to the reported value for the spherical nanoparticles [17]. The enhanced value of direct band gap may be due to the change in shape, which account for shifting of delocalized band. Further,

we also plotted $(\alpha h\nu)^{1/2}$ vs. hν and the curve thus obtained is shown in Fig. 3.2c. It provides the value of band gap corresponding to indirect transition. The value of band gap is calculated by extrapolating the linear portion of curve until it intercepts to energy axis. The value of indirect band gap is found to be 2.6 eV. Thus, the values of direct and indirect optical band gap of CdO nanowires were found to be 3.5 and 2.6 eV, respectively.

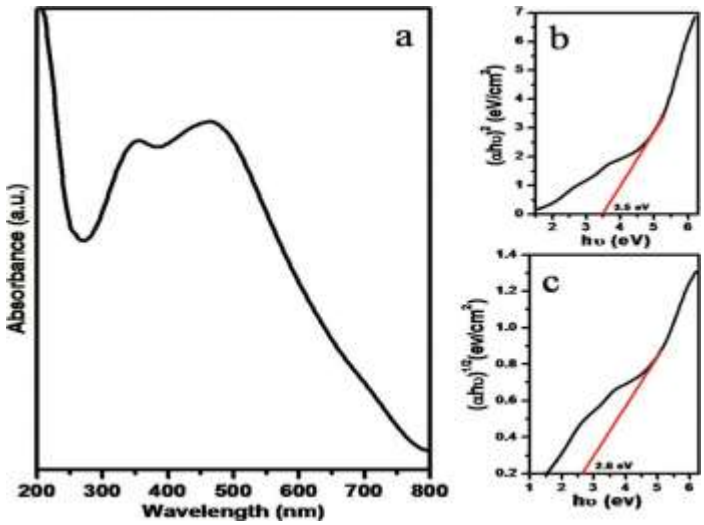


Fig. 3.2 (a) UV-VIS absorption spectrum of synthesized CdO nanowires (b) $(\alpha h\nu)^2$ and vs. hν plot (c) $(\alpha h\nu)^{1/2}$ vs. hν plot.

3.3.3 Raman spectroscopy

Raman scattering is very sensitive and valuable tool for the investigation and characterization of nanostructures. The Raman spectrum of CdO nanowires was recorded in the spectral range 200-1300 cm^{-1} and shown in Fig. 3.3. The Raman spectrum shows three peaks at ~ 290, ~392 and a broad weak band at 938 cm^{-1}. It is reported that only second-order Raman scattering is expected to appear in CdO [9]. The Raman peaks at

~ 290 and ~ 392 cm^{-1} are assigned to a 2TA(L) and 2LA(L) Raman scattered peak [9]. In order to assign the Raman features of CdO nanostructure, Cusco et al. [9] have performed a lattice dynamics study and they reported that the Raman peak appeared at ~ 392 cm^{-1} may be due to presence of high two phonons density of states in the spectral range 300-450 cm^{-1} and it may probably arise from 2LA overtones at different high symmetry points of the Brillouin zone. According to the selection rule, both TO and LO modes are dipole forbidden and therefore all features in the spectrum can be attributed to second-order Raman scattering process in CdO nanostructures.

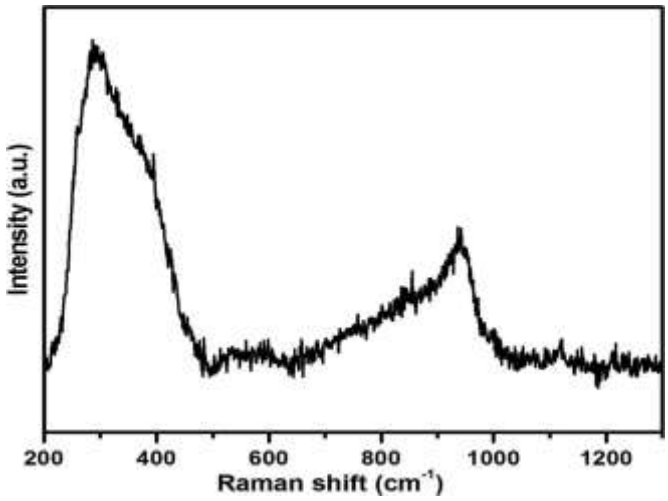


Fig. 3.3 Raman spectrum of CdO nanowires recorded for the spectral range 200-1300 cm^{-1}.

3.3.4 Antimicrobial activity

Nanostructures have high surface to volume ratio and reactive facets. Its nano size is responsible for generating reactive oxygen species, damage to the microbial or cell membrane lipids and damage to the DNA, which ultimately leads to death to the microbes or cell. Microbial culture of 106 colony forming unit (CFU) for analysis was fresh

prepared from stock solution. Microbes were inoculated in sterilized and autoclaved Muller Hinton Broth (MHB) to the conditions mentioned on the box. Further, 15 gm of MHB was dissolved in 1000 ml flask containing 500 ml of distilled water of pH 7.0 and incubated for 24 hours at 28±2 ◦C in an incubator shaker at 120 rpm. Plates were prepared from Muller Hinton Agar (MHA) to check the antimicrobial activity of filter paper disc coated with solution of CdO nanowires. Discs were 8 mm in size and made from sterilized filter paper. Modified Bauer-Kirby disc diffusion method was followed to study antimicrobial activity of CdO nanowires. Discs used were made up of sterilized filter paper and had a diameter of 8 mm. These discs were then impregnated with 20 µl CdO nanowires solution and placed onto MHA plates made up of autoclaved MHA media and had bacteria swabbed (100 µl). These plates were then incubated overnight at 28±2 ◦C and the zone of inhibition around each disc was measured. Large zone of inhibition around each disc indicated susceptibility of microbe toward CdO nanowires while small zones or no zones of inhibition indicated resistive microbes. Minimum inhibitory concentrations (MIC) and Minimum bactericidal concentration (MBC) of CdO nanowires has been studied against B.subtilis (gram+ve) and E.coli (gram-ve), as shown in Fig. 3.4a and 3.4b, respectively. Very recently Hossain et al. [18] had reported the toxicological behavior of synthesized CdO nanoparticles (NPs) on E. coli. They found that that the CdO nanoparticles have antibacterial activity against E. coli. In the study, the complete growth inhibitory concentration was found to be 40µg/ml. In another report [19], the antibacterial activity and acting mechanism of silver nanoparticles (SNPs) on E. coli ATCC 8739 were investigated. In the study, it was observed that the 10

μg/ml silver nanoparticles could completely inhibit the growth of 107 cfu/ml E. coli cells in liquid Mueller Hinton medium. Further, the silver nanoparticles were found to damage the structure of bacterial cell membrane and depress the activity of some membranous enzymes, which cause E. coli bacteria to die eventually. In another interesting report [20], the antibacterial activity of CuO nanoparticles was investigated against two gram positive and two gram negative bacteria such as; E. coli, B. subtilis, P. aeruginosa, and S. auereus. The antimicrobial activity of 20 nm CuO nanoparticles was found to be more pronounced against B. subtilis microbe. However, in the present report we tried explore the antimicrobial activity of CdO nanowires against B.subtilis (gram positive) and E.coli (gram negative) microbes. The complete growth inhibitory concentration against E.coli (gram negative) microbe was found to be 20 μg/ml. Further, we also observed that the CdO nanowires have strong antimicrobial effect against B.subtilis (gram+ve) than that of E.coli (gram-ve) microbes.

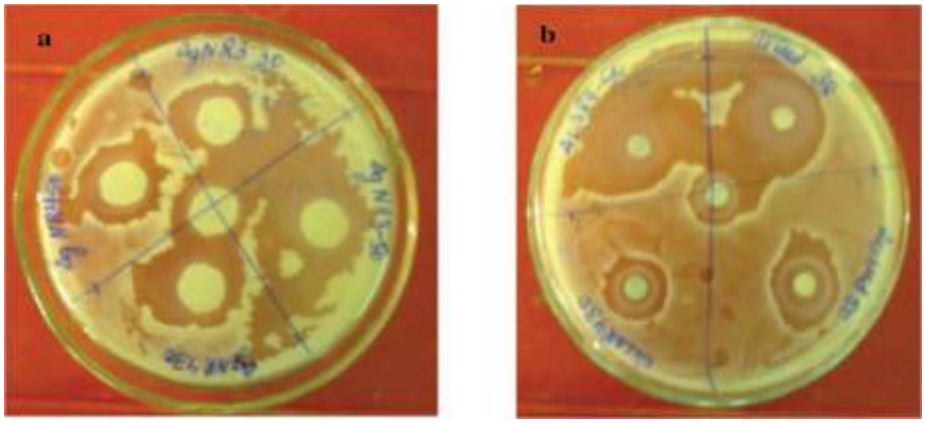


Fig. 3.4 Pictures of antimicrobial activity of CdO nanowires against (a) B. subtilis (gram+ve) (b) E.coli (gram-ve).

3.4 Conclusion

Ultra-long CdO nanowires have been synthesized by a simple, efficient and low cost chemical method. The obtained product is almost impurity free and well dispersed as confirmed by XRD and TEM measurements respectively. UV-VIS absorption spectrum shows absorption peaks at ~ 350 nm and ~ 463 nm. The values of direct and indirect band gap were calculated by plotting $(\alpha h\nu)^2$ vs. hν and $(\alpha h\nu)^{1/2}$ vs. hν curves, respectively. The Raman spectrum of CdO nanowires revealed second order Raman scattering. The antimicrobial activities of CdO nanowires are found to be better against B.subtilis (gram +ve) than that of E.coli (gram-ve) microbes. Moreover, it can be expected that this approach could be further extended to prepare other metal oxide nanowires.

References

[1] Y. Xia, P. Yang, Y. Sun, Y. Wu, B. Mayers, B. Gates, Y. Yin, F. Kim, H. Yan, Adv. Mater., 2003, **15**, 353.

[2] W. Lu, C. M. Lieber, J. Phys. D: Appl. Phys., 2006, **39**, R387.

[3] L. A. Bauer, N. S. Birenbaum, G. J. Meyer, J. Mater. Chem., 2004, **14**, 517.

[4] F. Zhang, S.-W. Chan, J. E. Spanier, E. Apak, Q. Jin, R. D. Robinson, I. P. Herman, Appl. Phys. Lett., 2002, **80**, 127.

[5] W.-S. Wang, L. Zhen, C.-Y. Xu, W.-Z. Shao, J. Phys. Chem. C, 2008, **112**, 14360.

[6] M. Rajalakshmi, A. K. Arora, B. S. Bendre, S. Mahamuni, Appl. Phys. Lett., 2000, **87**, 2445.

[7] V. Juttukonda, R. L. Paddock, J. E. Raymond, D. Denomme, A. E. Richardson, L. E.

Lusher, Bradley D. Fahlman, J. Am. Chem. Soc., 2006, **128**, 420.

[8] F. Yakuphanoglu, Appl. Surf. Sci., 2010, **257**, 1413.

[9] R. Cusco, J. lbanez, N. D. Amador, L. Artus, J. Z. Perez, V. M. Sanjose, J. Appl. Phys., 2010, **107**, 063519.

[10] A. S. Kamble, R. C. Pawar, N. L. Tarwal, L. D. More, P. S. Patil, Mater. Lett., 2011, **65**, 1488.

[11] T. Ghosal, S. Kar, S. Chaudhari, Appl. Surf. Sci., 2007, **253**, 7578.

[12] Z. Guo, M. Li, J. Liu, Nanotechnology, 2008, **19**, 245611.

[13] F. Zhang, L. Bei, J. M. Cao, X. Wang, J. Solid State chem., 2008, **181**, 143.

[14] X. S. Peng, X. F. Wang, Y. W. Wang, G. W. Meng L. D. Zhang, J. Phys. D: Appl. Phys., 2002, **35**, L101.

[15] K. Cheng, Y. P. He, Y. M. Miao, B. S. Zou, Y. G. Wang, T. H. Wang, X. T. Zhang, Z. L. Du, J. Phys. Chem., 2006, **110**, 7259.

[16] P. K. Ghosh, S. Das, K. K. Chaudhary, J. Nanopart. Res., 2005, **7**, 219.

[17] N. C. S. Selvam, R. T. Kumar, K. Yogeenth, L. J. Kennedy, G. Sekaran, J. Judith Vijaya, Powder Technol., 2011, **211**, 250.

[18] S. K. T. Hossain, S. K. Mukherjee, Langmuir, 2012, **28**, 16614.

[19] W.-R. Li, X-B. Xie, Q.-S. Shi, H.-Y. Zeng, Y.-Sheng OU-Yang, Yi. B. Chen, Appl. Microbiol. Biotechnol., 2010, **85**, 1115.

[20] A. Azam, A. S. Ahmed, M. Oves, M. S. Khan, A. Memic, Int. J. Nanomedicine, 2012, **7**, 3527.

CHAPTER - 4

Synthesis and Raman signature for the formation of cadmium oxide/manganese oxide (core/shell) nanostructures

In this chapter, pure cadmium oxide (CdO) and cadmium oxide/manganese oxide (CdO/MnO_2) core/shell nanostructures of various cores and different shell sizes were synthesized using co-precipitation method. The phase, size, shape and structural details of the pure CdO and CdO/MnO_2 (core/shell) nanostructures were investigated by X-ray diffraction (XRD), transmission electron microscopy (TEM), and Raman spectroscopy (RS) measurements. TEM micrographs confirm the formation of core/shell nanostructures. The presence of CdO (core) and MnO_2 (shell) crystal phase was determined by analyzing the Raman spectra of pure CdO and CdO/MnO_2 (core/shell) nanostructures. The disappearance of characteristics Raman bands of CdO crystal phase and the appearance of characteristics Raman bands corresponding to MnO_2 phase for the nanostructures of shell size 5.3 ± 1nm authenticate the presence of CdO nanostructures as core and MnO_2 nanostructures as shell in the core/shell nanostructures.

4.1 Introduction

Cadmium oxide (CdO) is an n-type semiconductor having rocksalt structure with strongly ionic character. Recently, it has attracted great attention of the worldwide scientists because of its applications in various fields such as; solar cells and flat-panel displays. It has an indirect band gap of 1.2 eV and a direct gap of 2.3 eV [1] corresponding to $\Sigma_3 - \Gamma_1$ and $\Gamma_{15} - \Gamma_1$ optical transitions, respectively. Very recently, the band gap energy and the band-edge effective mass values of CdO were reported to be 2.16 ± 0.02 eV and (0.21 ± 0.01) m_0, respectively, using optical measurements [1].

Recently, low dimensional materials have been a subject of significant research interest for the scientists due to its unique size and shape dependent physical and chemical properties. Because of the unique size and shape dependent properties, the low-dimensional materials have numerous device based applications. By reducing the size of nanostructures, unusual transport, structural, and optical properties may be obtained. These properties are largely due to the size dependent quantum confinement effects and additional surface electron states. Quantum confinement is much stronger in core/shell nanostructures and/or quantum wells, since the thickness of active layers is comparable with the mean free path of the charge carriers [2].

Raman spectroscopy has been proven to be a non destructive and powerful technique to study the molecular and crystal lattice vibrations. Recently, it has also been used to study nanomaterials because it is very sensitive to the structure and symmetry of the systems. The Raman spectroscopy has been widely used for studying the phonon

confinement, strain and substitutional effects, porosity, and non-stoichiometry in nanomaterials of different shapes and sizes [2-3]. The Raman measurements of any sample contain the scientific information about the sample in terms of Raman bands. The parameters of the Raman bands such as peak position, line width and intensities provide the information about the composition, chemical environment, and crystalline/amorphous along with the confinement details of phonons in nanostructured materials [3]. Due to large surface to volume ratio of the nanoparticles, the states of the surface atoms play an important role in determining the properties of nanostructured materials. It has also been observed that if the size of nanoparticles becomes very small, then only surface mode persists in the system. Surface optical phonon-based Raman spectra were observed in the spectral range of 545-565 cm^{-1} for metal semiconductor Zn/ZnO (core/shell) structured nanomaterials [4]. Baranov et al. [5] have found a very weak surface optical phonon mode, which shifts toward red with the increase of shell thickness of CdSe/ZnS (core/shell) quantum dots. Ashrafi et al. [2] proposed a simple method to grow and detect the wurtzite CdO nano layer on a very thin film of ZnO layer using Raman spectroscopy. According to Raman selection rules, the wurtzite nanophase is Raman active where thermodynamically preferred rocksalt phase is inactive. In the study, Raman signature of the wurtzite nanophase was identified using Raman measurements.

Cadmium oxide belongs to the class of rocksalt structure in which first order Raman modes are forbidden. Schaack and Uhle [1] had performed Raman measurements on polycrystalline CdO samples having different electron densities, and two first order

Raman bands were observed at ~ 404 and ~ 354 cm^{-1}. The second order bands peaking at ~ 970 and ~ 780 cm^{-1} were described in terms of 2LO and 2TO Raman process. However, the assignment of second order modes was not done on the basis of phonon dispersion curves of CdO. In order to explain the origin of the first order and second order Raman bands in CdO, Cusco et al. [6] had performed Raman scattering measurements on high quality CdO thin films grown by metal-organic vapor-phase epitaxy on substrates, and the Raman bands were assigned on the basis of phonon dispersion curve of CdO obtained by the ab-initio calculation. They found two main features at ~ 265 and ~ 390 cm^{-1}. The mode at ~ 265cm^{-1} is assigned to 2TA(L), and the broad feature at ~ 390 cm^{-1} has appeared due to the presence of two-phonon density of state in the spectral region 300-450 cm^{-1}. Based on the confinement of phonon in nanomaterials, which eventually causes to relax q = 0 selection rule, to the best of our knowledge, the Raman spectroscopic study of nanostructured CdO is still lacking in the literature.

Mainly, two approaches have been used to understand and predict the Raman signature of the materials: (i) the molecular description and (ii) the phonon description. The band structure of the material is a function of size and shape and therefore, overall phonon behavior of the nanomaterials also got modified because of the confinement of phonons between the grain boundaries [7-9]. The size and shape dependent Raman features of different materials have been explained using two models: (i) phonon confinement model (PCM), which projects Raman 'inactive' bulk modes onto the Brillouin zone (BZ) center, and (ii) elastic sphere model, which describes the free oscillations of isolated

spheres. The PCM cannot be applied to the acoustic modes because their energy is zero at BZ center and it is very rarely used for the transverse optical (TO) phonon modes on account of their low dispersion. It is almost exclusively applied to the longitudinal optical (LO) phonon modes. In case of low dimensional materials, in addition to the TO phonon at K = 0, the LO phonon, away from K = 0 point, also participates in the Raman scattering process, leading to asymmetric Raman feature towards low frequency side. Besides, the dipoles generated in polar semiconductors by vibration of optical phonon it also generates electromagnetic fields. As a result, it also may interact with electrons (polarons) or electron–hole pairs (excitons).

Fröhlich interaction is weak in single crystals but leads to strong resonance of the LO and surface optical (SO) phonon modes in confined semiconductors; quantum dots, wires, and superlattices. The use of bulk dispersion curve is questionable when the particle size is very small. An alternative way to consider the vibrations as ensuing from a disturbed infinite crystal (what the PCM does) is to be adopted for principle description of vibrations in a free sphere. In long-range ordered solids, the bandwidth is much smaller, and the peak intensity is highly determined by structural symmetry and polarization effects. Raman scattering probes the chemical bond and its neighbor, 0.5-10 nm, typically and is thus well suited to analyze disordered materials. The band intensity is the best measure of the structure distortion of an ideal cubic lattice. In nanostructures, the segregation of the vacancies that led to short/medium-range order and even to long-range order is well studied by X-ray diffuse scattering and diffraction measurements,

respectively. The lattice modification in the nanostructured materials, which produced short-range and long-range interactions, can also be studied using Raman spectroscopy techniques. The ideal perovskite structure is cubic, and according to symmetry rules, no Raman activity is detected for this symmetry [7-9]. However, if many perovskites structure exhibit a (mean) cubic structure from the XRD point of view, the Raman activity is clearly observed. The bandwidth of the Raman band is generally much larger because of the short-range/orientational disorder in the material due to B substitution and oxygen vacancies. Actually, the band intensity is the best measure of the structure distortion of an ideal cubic lattice [7–9]. Further, the nanomaterials of desired physical and chemical properties can be achieved by controlling the size of core and shell in core/shell nanostructures. The core/shell nanostructures have attracted enormous amount of interest because of their unique optical, magnetic, and catalytic properties [2]. The binary CdO/MnO_2 nanostructures are very promising for applications in light emitting diode, electrochemical and magnetic properties [10, 11]. MnO_2 is one of the most attractive materials because of its ion exchange and catalytic behavior. It is widely used as catalysts [10] and electrode materials in Li/MnO_2 batteries [11] because of its energetic compatibility in a reversible lithium electrochemical system.

Here, a simple and low-cost method to synthesize pure CdO and CdO/MnO_2 (core/shell) nanostructures with different core (CdO) and shell (MnO_2) sizes has been presented. XRD and TEM measurements were carried out to study the structural and size/shape details of the synthesized samples. The evolution of phonon modes in

nanostructured CdO and CdO/MnO_2 (core/shell) nanostructures with different core/shell sizes has been investigated using Raman spectroscopic measurements.

4.2 Experimental Techniques

4.2.1 Synthesis

Pure CdO and CdO/MnO_2 (core/shell) nanostructures were synthesized at room temperature using a very simple and low-cost chemical method. For synthesizing desired nanostructures, $Cd(CH_3COO)_2.2H_2O$, $Mn(CH_3COO)_2.4H_2O$, and ammonia solution 25% (0.91gm/cc^3) chemicals have been procured from Sigma Aldrich and used as starting chemicals. All chemicals were used without further purification. In order to synthesize CdO/MnO_2 (core/shell) nanostructure, firstly, pure CdO nanostructure is synthesized and thereby mixing an appropriate amount of $Mn(CH_3COO)_2.4H_2O$ in the final solution, the desired product was obtained. For the synthesis of CdO nanostructures, 13.32 gm of $Cd(CH_3COO)_2.2H_2O$ was dissolved in distilled water for making 0.5M solution, and mixed solution is stirred for 30 min. During the stirring, ammonia solution was added drop wise into the mixed solution until the pH value is reached to 9.0. While adding the ammonia, a white precipitate was formed at the bottom of the solution. The stirring of the solution was continued for another 2 h. The white precipitate was finally settled down in 5 h. Thereafter, the solution was filtered and washed repeatedly with distilled water to remove unreacted materials. The obtained solid material was dried at ~100 °C and grinded to make a resulting powder. The grinded powder was calcined at 400 °C for 2 h to obtain the final product.

In order to synthesize CdO/MnO_2 nanostructures for different core and shell sizes, 0.1225 gm (x = 0.01), 0.3675gm (x = 0.03), 0.6125 gm (x = 0.05), and 0.8575 gm (x = 0.07) of $Mn(CH_3COO)_2.4H_2O$ were mixed to 0.5M aqueous solution of $Cd(CH_3COO)_2.2H_2O$. Further, the mixed solution is kept for stirring for 50 min, and ammonia solution is added drop wise during the stirring until the pH value is reached to 9.0. Subsequently, the solution at a fixed pH value (9.0) is kept for stirring for another 2.5 h. While stirring, a brown precipitate is formed. The rest of the process was kept same, as we have done for the synthesis of CdO nanostructures. The size of core and shell varies by changing the value of x. The stoichiometric ratios are in agreement with the size of core and shell of the synthesized (core/shell) nanostructures. The size of shell is increased with increasing the Mn concentration.

4.2.2 Characterization

The structural/crystalline phase analysis of the synthesized samples was carried out by Rigaku Smart Lab X-ray diffractometer equipped with a copper target and nickel filter. For the XRD measurements, the X-ray of wavelength 1.54 Å of CuKα operated at 30 kV and 30 mA was used. The structural details of the synthesized samples were further investigated through TEM measurements. Samples for transmission electron microscopy were deposited onto 300 mesh copper TEM grids coated with 50-nm carbon films. The samples were suspended in water and directly added drop wise to the grid. The excess amount of water was allowed to evaporate in air. The grids were examined with a Tecnai G20 S-Twin 2010 microscope with ultra high resolution microscope using a LaB6 filament

operated at 200 KeV. The Raman spectra of the synthesized samples were recorded at room temperature using a micro-Raman setup of Renishaw, UK, equipped with a grating of 2400 lines/mm and a Peltier cooled charge coupled device (CCD). The GRAM-32 software was used for data collection. The accumulation time for one window was selected as 60s, and five spectra were accumulated in each window. In one window, 800 cm^{-1} range was covered. The resolution of the spectrometer was ~ 1 cm^{-1}. A microscope from Olympus (Model: MX50 A/T) attached with the spectrometer focused the laser light onto the sample and collected the scattered light at 180° scattering geometry. The laser power at the sample was 5mW. The 514.5 nm line of Ar^{+} laser was used as an excitation source. The Raman spectra were collected in the spectral range of 200-1050 cm^{-1} that contained all Raman bands. In order to ensure the reproducibility of the Raman spectra, the Raman scattered signals were collected from ten different points of the samples, and from each point, we obtained almost the same Raman feature.

4.3 Results and Discussion

4.3.1 XRD

The XRD patterns of the synthesized samples are shown in Fig. 4.1. The XRD peaks have been indexed on the basis of the data available with the Joint Committee on Powder Diffraction Standards (JCPDS) card no. 73-2245. The XRD pattern has five prominent peaks corresponding to the cubic structure of CdO. These peaks were indexed as (111), (200), (220), (311), and (222) planes. In both, pure CdO and Mn doped CdO samples at x = 0.01, 0.03, and 0.05, the peak corresponding to (111) plane is more intense. Here, I

would like to note that the additional phases corresponding to Mn or any binary phase are not observed in the XRD pattern for any of the synthesized samples. The reduction in intensity and broadening of diffraction peaks by increasing Mn content suggest the nano crystalline nature of the samples. The average crystallite sizes (D) have been determined for the five observed planes in the patterns by applying Scherrer formula. The average value of crystallite size was found to be 21.7 nm for pure CdO nanostructures and 13.3, 12.8, 11.2, and 10.5 nm for $Cd_{1-x}Mn_xO$ (x = 0.01, 0.03, 0.05, and 0.07) nanostructures, respectively.

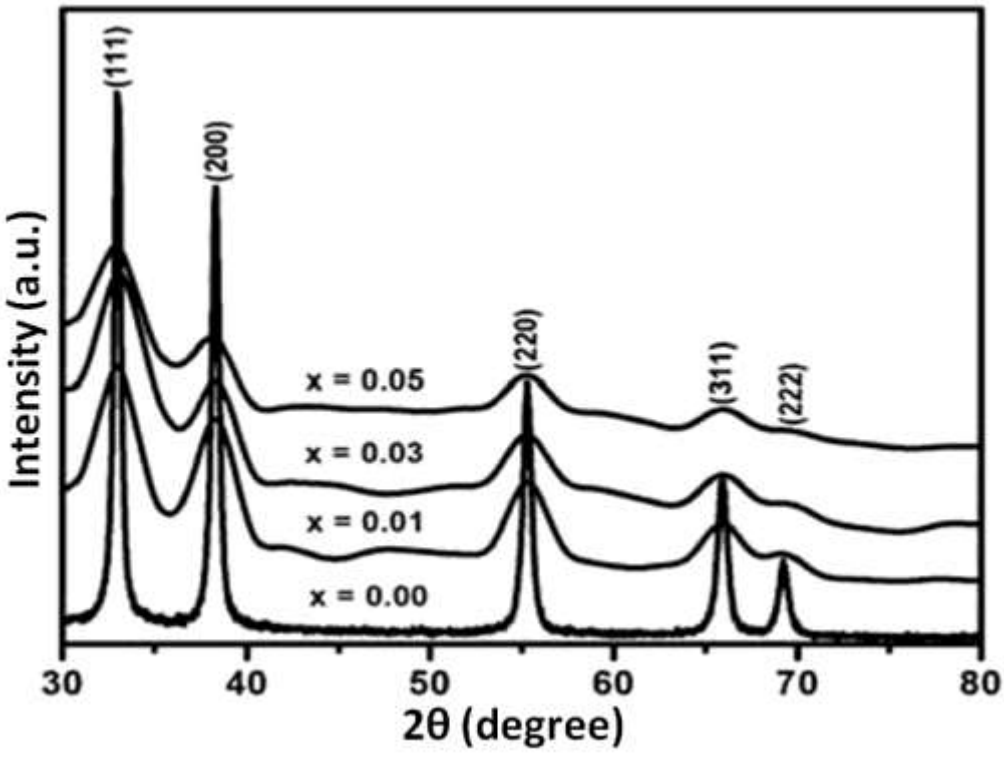


Fig. 4.1 Room temperature powder XRD patterns of $Cd_{1-x}Mn_xO$ (x = 0.00, 0.01, 0.03, and 0.05) nanostructures.

4.3.2 TEM

The pure and Mn doped nanostructures for x = 0.01, 0.03, 0.05, and 0.07 were further characterized by TEM measurements. The TEM micrographs of Mn doped CdO nanostructures for x = 0.01, 0.03, and 0.07 were presented in Fig. 4.2a-c, respectively. By looking at the TEM micrographs, as shown in Fig. 4.2a-c, it is quite interesting to note that the synthesized nanostructures have core/shell features with different core and shell sizes at each value of doping concentration (x) of Mn. We measured the size of core and shell at each value of x. The measured value of size of core and shell in core/shell nanostructures for each value of x is presented in Table 4.1. It is quite evident from the data presented in Table 4.1 that the size of shell is increased by ~ 4 nm from increasing the value of x from 0.01 to 0.07, which indicates that the shell of nanostructures may be Mn based crystalline phase such as MnO, α-Mn_2O_3, β-MnO_2, α-MnO_2, and α-Mn_3O_4. However, we could not observe any evidence of Mn-based crystalline phase, as mentioned earlier in the XRD pattern. In order to resolve this issue, we have performed a thorough literature survey for finding XRD information related to MnO, Mn_2O_3, MnO_2, and Mn_3O_4 phases [12]. By going through these articles, we found that MnO_2 phase has four XRD peaks, and it is very interesting to note that the 2θ value of these peaks is almost the same as the 2θ value of XRD peaks of CdO nanostructures reported in the present study; i.e. the XRD patterns of nanostructures, MnO_2 and CdO almost coincide to each other and made us difficult to distinguish the presence of these two phases in the synthesized core/shell nanostructures using XRD data.

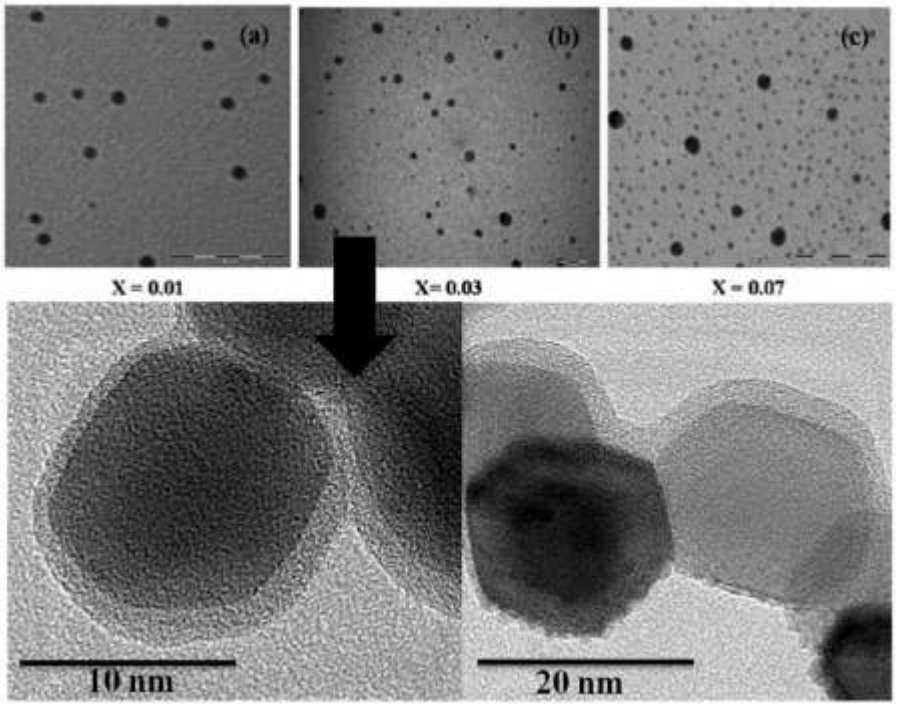


Fig. 4.2 Transmission electron microscopy micrographs of $Cd_{1-x}Mn_xO$ nanostructures: (a) x = 0.01, (b) x = 0.03, and (c) x = 0.07.

Table 4.1 Size of core (nm) and shell (nm) of CdO/MnO_2 (core/shell) nanostructures.

	$Cd_{1-x}Mn_xO$				
	x = 0	**x = 0.01**	**x=0.03**	**x = 0.05**	**x=0.07**
Core	21±2	12±2	9.5±2	6.5±1	4.5±1
Shell	00	1.3±0.1	3.3±0.4	4.5±1	5.3±1

4.3.3 Raman spectroscopy

In order to distinguish the presence of these two phases and also about gaining the information of core and shell materials in core/ shell nanostructures, we have carried out Raman measurements for pure CdO nanostructures and core/shell nanostructures

synthesized at x = 0.01, 0.03, 0.05, and 0.07 using 514.5 nm as the excitation wavelength. The Raman spectra of pure CdO nanostructures are recorded for the spectral range of 200-1050 cm^{-1}. The experimentally recorded Raman spectrum of pure CdO nanostructures along with the fitted one is presented in Fig. 4.3a. The Raman spectra of pure CdO nanostructures contain one broad intense feature spanning from 200 to 500 cm^{-1} and a weaker band located at ~ 940 cm^{-1}. One can easily notice by looking at the broad feature of pure nanostructures that it has asymmetrical feature and it seems that it consists of more than one Raman bands. In order to resolve the component Raman bands, the broad Raman feature that spanned from 200 to 500 cm^{-1} is fitted by Lorentzian functions. We obtained the best fit corresponding to the three Raman component bands at 268 ± 1, 305 ± 3, and 385 ± 3 cm^{-1}. In a recent study [5], the authors have observed a similar kind of broad feature that spanned from 200 to 450 cm^{-1} for CdO. In the study, the authors have performed Raman measurements on CdO thin film at low temperature (at 80 K). They found that the broad feature is essentially composed of three different bands centered at 265, 310, and 390 cm^{-1}. Thus, in the present study, the peak positions of the three fitted components are in good agreement with those observed experimentally by Cusco et al. [5] The Raman band centered at 268±1 is assigned to 2TA(L) mode, and the bands at 305 ± 3 and 385 ± 3 cm^{-1} are assigned to 2LA overtones at different high symmetry points of the Brillouin zone [5]. The wavenumebr positions and vibrational assignments of these Raman bands are given in Table 4.2.

The Raman spectra of the synthesized core/shell nanostructures of shell sizes 1.3,

3.3, 4.5, and 5.3 nm were recorded in the spectral range of 200-1050 cm^{-1} and presented in Fig. 4.3b. From Fig. 4.3b, one can easily notice that the intensity of broad feature and 2LO band (940 cm^{-1}), as we have observed in the Raman spectra of pure CdO nanostructure, is decreased gradually with increasing the shell size from 1.3 to 3.3 nm of core/shell nanostructures. Further, the two additional bands have also been appeared in the Raman spectra of core/shell nanostructures for each shell size compared with the Raman spectra of pure CdO nanostructure. To determine the peak positions of the Raman components that contributed to the broad feature for each shell size, the obtained Raman peaks at each shell size has been fitted using Lorentzian function, and experimental as well as fitted Raman spectra for shell sizes 1.3, 3.3, 4.5, and 5.3 nm are given in Fig. 4.3b. The peak positions of Raman bands at each shell size of the core/shell nanostructure obtained by fitting along with the band assignments are given in Table 4.2. The Raman band at 268 ± 1 cm^{-1} showing a blue shift of 14 cm^{-1} upon increase of shell size from zero to 5.3 nm. On the other hand, the Raman intensity keeps on decreasing consistently with increasing shell size from zero to 5.3 nm. The Raman band at 305 cm^{-1} is blue shifted by 5 cm^{-1} compared to its position in pure CdO nanostructure, and in this case also, the Raman intensity is decreased gradually with increase of shell size, and it becomes zero for core/shell nanostructure of shell size 4.5 nm. However, the Raman band at 385 cm^{-1} is red shifted by 23 cm^{-1} with the increase of shell size from 0 to 3.3 nm, and the intensity of the band is decreased with the increase of shell size, and the Raman band completely disappeared for the core/shell nanostructure of shell size 4.5 nm. The Raman band at 940 cm^{-1} (2LO) mode is red shifted

by 20 cm^{-1} with increasing the shell size from 0 to 3.3 nm and disappeared completely in case of core/shell nanostructure of shell size 4.5 nm. By the previous discussion, we would like to note that the Raman bands of pure CdO nanostructure centered at 305, 385, and 940 cm^{-1} disappeared completely for the core/shell nanostructure of shell size 4.5 nm. It is noteworthy to mention that by increasing the doping concentration of Mn from 0.01 to 0.07, the size of core is decreased from 12 to 6 nm, and the shell size is increased from 1.3 to 5.3 nm. Moreover, the overall size of the core/shell nanostructure is decreased. The blue shifting of Raman bands with increasing the shell size from zeo to 4.5 nm may be explained in terms of confinement effect in heterostructures, which induces a broadening and blue shift in Raman bands due to biaxial strain [2]. The disappearance of Raman bands for the core/shell nanostructure of shell size 4.5 nm indicates that CdO nanostructure is completely surrounded by the shell of sufficient thickness (~ 4.5 nm), which does not allow optical phonon of CdO (core) to participate in the Raman scattering process. Thus, the Raman features that has been observed in the Raman spectra of core/shell nanostructures of shell size more than 4.5 nm are basically belonging to Raman scattering from optical phonon of the shell (MnO_2) only. In view of the previous results and discussion on the Raman spectra of core/shell nanostructures, one can conclude that the CdO is situated at the core of core/shell nanostructures.

In the Raman spectra of core/shell nanostructures, two new Raman bands were observed at ~ 451 and ~ 665 cm^{-1} for shell size 1.3 nm compared to Raman bands observed for pure CdO nanostructures. Interestingly, the intensity of these additional Raman bands

is enhanced consistently with increasing the size of shell from 1.3 to 5.3 nm and these bands attain maximum intensity for the shell of size 5.3 nm. The enhancement in intensity of these bands with increasing shell size indicates that the shell could be composed of Mn based crystalline phases such as MnO, Mn_2O_3, MnO_2, and Mn_3O_4. Now, the question is how to determine that which Mn based crystalline phase is present as shell in core/shell nanostructures. The answer of this question could be addressed by assigning the two additional Raman bands peaking at ~ 451 and ~ 665 cm^{-1}. In order to assign these bands, we looked into earlier reported studies on Mn based oxides nanostructures [13-17]. Buciman et al. [14] had studied different crystalline phases of manganese oxide by Raman, Fourier transform infrared (FTIR), and XRD measurements. They observed two characteristics Raman bands at ~ 530 and ~ 665 cm^{-1} for MnO_2. Julien et al. [16] had also performed Raman spectroscopic measurements on different manganese oxide samples; they also found two characteristics Raman bands at ~ 538 and ~ 665 cm^{-1} corresponding to MnO_2. In another study, [17] the characteristics Raman features for MnO_2 are reported to be ~ 486 and ~ 665 cm^{-1}. In all these studies, the Raman bands centered at ~ 665 cm^{-1} is the same as we have observed in the present study. We could assign the Raman bands at ~ 451 and ~ 665 cm^{-1} as deformation of Mn-O-Mn and Mn-O stretching modes of MnO_2. It confirms that the shell of core/shell nanostructures is composed of MnO_2 nanostructures. Thus, in the present study, we have used Raman spectroscopy as an important characterizing tool to confirm the formation of CdO/MnO_2 (core/shell) nanostructures, which we could not confirm by XRD data.

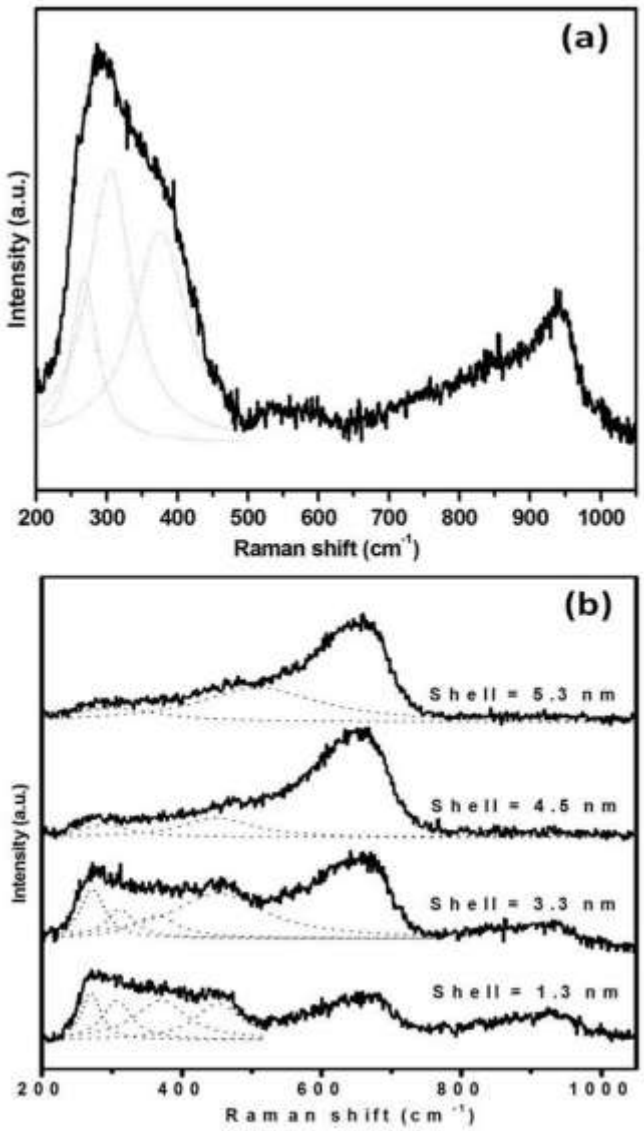


Fig. 4.3 (a) Room temperature experimental (solid line) and fitted (dotted line) Raman spectra of $Cd_{1-x}Mn_xO$ (x = 0.00) nanostructures recorded in the spectral range of 200–1050 cm^{-1}. (b) Fitted as well as recorded room temperature Raman spectra CdO/MnO_2 (core/shell) nanostructures of shell sizes 1.3, 3.3, 4.5 and 5.3nm in the spectral range of 200–1050 cm^{-1}.

Table 4.2 The peak positions (cm^{-1}) of Raman bands for pure CdO (x=0) nanostructures and CdO/MnO_2 (core/shell) nanostructures of shell size (1.3, 3.3, 4.5, and 5.3 nm).

$Cd_{1-x}Mn_xO$					Assignments	Ref.5, 14
x = 0	**x = 0.01**	**x = 0.03**	**x = 0.05**	**x = 0.07**		
268±1	270±1	272±1	380±1	282±1	2TA (L) (CdO)	265
305±3	307±2	310±1	-	-	2LA (CdO)	300
385±3	369±3	362±3	-	-	2LA(CdO)	390
	452±2	455±2	465±2	480±2	Deformation of Mn-O-Mn (MnO_2)	486
	665	658	658	653	Mn-O stretching	665
940	927	920	-	-	2LO (CdO)	940

4.4 Conclusion

In the present study, CdO/MnO_2 (core/shell) nanostructures have been synthesized by a simple and low cost chemical synthesis method. TEM micrographs confirm the formation of core/shell nanostructures, but by analyzing XRD spectra, it is very difficult to confirm the dual phase of CdO/MnO_2. It is due to the fact that peak positions of the XRD peak of CdO and MnO_2 almost coincide to each other. To resolve this problem, we have performed Raman spectroscopy measurements of the synthesized samples. The appearance and disappearance of characteristics Raman bands corresponding to MnO_2 and CdO phases in the Raman spectra of synthesized samples confirmed the formation of CdO/MnO_2 (core/shell) nanostructures. The presence of MnO_2 crystalline phase as shell in core/shell nanostructures is confirmed by the enhancement in intensity of Raman bands centered at ~

451 and ~ 665 cm^{-1} with increasing the shell size from 1.3 to 5.3 nm. The Raman bands at 451 and 665 cm^{-1} are assigned to the deformation of Mn-O-Mn and Mn-O stretching modes of MnO_2.

References

[1] G. Schaack, N. Uhle, Solid State Comm., 1976, **315**, 318.

[2] A. Ashrafi, K. Ostrikov, Appl. Phys. Lett., 2011, **98**, 133119.

[3] M. Srivastava, N. Vyas, A. K. Ojha, Vib. Spectrosc., 2011, **56**, 19.

[4] H. Zeng, W. Cai, B. Cao, J. Hu, Y. Li, P. Liu, Appl. Phys. Lett., 2006, **88**, 181905.

[5] R. Cusco, J. Lbanez, N. D. Amador, L. Artus, J. Z. Perez, V. M. Sanjose, J. Appl. Phys., 2010, **107**, 063519.

[6] S. R. Segal, S. L. Suib, L. Foland, Chem. Mater., 1997, **9**, 2526.

[7] G. Gouadec, P. Colomban, Prog. Cryst. Growth Ch. Mat., 2007, **53**, 1.

[8] P. Colomban, Quantum Matter., 2014, **3**, 361 and references cited there in.

[9] T. T. K. Chi, G. Gouadec, P. Colomban, G. Wang, L. Mazerolles, N. Q. Liemb, J. Raman Spectrosc., 2011, **42**, 1007.

[10] M. M. Thackeray, W. I. F. David, P. G. Bruce, J. B. Goodenough, Mater. Res. Bull., 1983, **18**, 461.

[11] J. Wang, E. Khoo, J. Ma, P. S. Lee, Chem. Commun., 2010, **46**, 2468 and references cited there in.

[12] L. D. Mishima, T. Ohtsuka, N. Sato, J. Electroanal. Chem., 1988, **243**, 219 and references cited there in.

[13] F. Buciuman, F. Patcas, R. Craciun, D. R. T. Zahn, Phys. Chem. Chem. Phys., 1999, **1**, 185.

[14] B. Ammundsen, G. R. Burns, M. Saiful, H. Kanoh, J. Roziere, J. Phys. Chem. B, 1999, **103**, 5175.

[15] C. Julien, M. Massot, R. B. Hadjean, S. Franger, S. Bach, J. P. P. Ramos, Solid State Ion., 2003, **159**, 345.

[16] S. B. Ma, K. Y. Ahn, E. S. Lee, K. H. Oh, K. B. Kim, Carbon, 2007, **45**, 375.

[17] C. M. Julien, M. Massot, C. Poinsignon, Spectrochimica Acta Part A, 2004, **60**, 689.

CHAPTER - 5

Controlled synthesis and magnetic properties of monodispersed cerium oxide nanoparticles

In this chapter, monodispersed cerium oxide (CeO_2) nanoparticles (NPs) of size 8.5 ± 1.0, 11.4 ± 1.0 and 15.4 ±1.0 nm were synthesized using the sol-gel method. Size dependent structural, optical and magnetic properties of as prepared samples were investigated by X-ray diffraction (XRD), scanning electron microscope (SEM), transmission electron microscope (TEM), ultraviolet-visible (UV-VIS) spectroscopy, Raman spectroscopy (RS) and vibrating sample magnetometer (VSM) measurements. The decrease in the value of optical band gap with increase of particle size may be attributed to the quantum confinement, which causes to produce localized states created by the oxygen vacancies due to the conversion of Ce^{4+} ions into Ce^{3+} ions at higher calcination temperature. The shift in the Raman peak could be due to lattice strain developed due to variation in particle size. Weak ferromagnetism at room temperature is observed for each particle size. The increase of saturation magnetization (Ms) and remanent magnetization (Mr) for larger particle size may be explained in terms of increased density of oxygen vacancies at higher calcination temperature.

5.1 Introduction

Nanostructured materials having a size of less than 100 nm, at least in one dimension, exhibit extraordinary optical, magnetic, electrical, thermal, and mechanical properties compared to the bulk material. Owing to the unique size and shape dependent physical and chemical properties, nanostructured materials have attracted considerable attention to the scientific community. The band gap of materials can be engineered by changing the shape and size to adapt the material for different technological applications. The large surface-to-volume ratio of nanostructures provides novel approach for developing a new generation of functional and smart materials, which opening up the opportunity to start a new era in the field of science and technology [1].

Cerium oxide (CeO_2), commonly known as ceria has a cubic structure. It is one of the most important oxides of the member of rare earth. In general, cerium forms two different types of oxide materials that are cerium (III) oxide, Ce_2O_3, called cerous and cerium (IV) oxide, CeO_2, called ceric [2-3]. Structurally, CeO_2 is found to be more stable than Ce_2O_3. In the previous studies [2-3], it has been observed experimentally that both of these oxidation states (Ce^{4+} and Ce^{3+}) of Ce strongly absorb ultraviolet light. The absorption peak in the spectral range 230-260 nm corresponds to Ce_2O_3 while CeO_2 absorbs the light in the spectral range 300-400 nm [2-3]. In the last few years, nanostructured CeO_2 in powder form has been broadly studied [4-6]. Additionally, CeO_2 nanomaterials have attracted wide interest to the research community due to their potential applications in various fields such as ultra violet filter and blocker [7-8], luminescent

material [9], polishing material [10], skin cancer treatment [11], solar cell [12], catalytic material [13], oxygen storage capacitor [14] and oxygen sensor [15].

In recent decade, diluted magnetic semiconductor (DMS) has attracted great attention from the worldwide scientists to investigate origin of ferromagnetism and its size dependence. Several efforts have been made to find out new kinds of magnetic nanostructures which can exhibit both, magnetic and semiconducting properties [16]. The ferromagnetic materials rich with semiconducting properties remove the difficulties associated with the injection of spins into nonmagnetic semiconductors [17]. Nowadays, diluted magnetic oxide (DMO) compounds are very famous for developing spintronics devices due to their unique property of utilizing electron spin in addition to charge for creating new functional materials beyond conventional semiconductors [18]. Such study to develop new material with room temperature ferromagnetism along with the semiconducting properties is very useful to engineer and design new spintronics devices like magnetic sensors, spin light emitting diodes, spin valves and ultra-fast optical switches [19]. CeO_2 is a chemically stable oxide with capacity to store or release oxygen due to the variation of the oxidation state from Ce^{4+} to Ce^{3+}. The variation of the oxidation state, CeO_2 can form stable oxygen vacancies in the matrix. These oxygen vacancies play an important role to produce magnetism in the oxide nanomaterials [20-21]. Coey et. al. [22] has suggested that the oxygen vacancies can make a significant contribution to enhance the ferromagnetism by changing the band structure of the host oxides. Sundaresan et. al. [17] has explained the ferromagnetism in CeO_2 NPs in terms of exchange interactions between

unpaired spins resulting from oxygen vacancies.

The size and shape dependent magnetic properties of CeO_2 NPs had been widely studied by many research group [23-25]. They observed ferromagnetism in pure spherical CeO_2 nanocrystals or cubes while bulk CeO_2 shows diamagnetic behavior. Liu et al. [23] has studied size dependent ferromagnetism in CeO_2 NPs. In this study, they found that the spherical CeO_2 NPs of particle size in the range of 200-500 nm show paramagnetic behavior while 5-20 nm size of spherical CeO_2 NPs show ferromagnetic behavior. The authors found that the room temperature ferromagnetism (RTFM) was observed only for the particle of size 20 nm with Ms value of 0.08 emu/gm. Recently, RTFM with Ms value of 0.12 emu/g of CeO_2 NPs prepared by thermal decomposition method has been reported [24]. The authors explained the ferromagnetism observed for CeO_2 NPs in terms of an increased value of the surface-to-volume ratio as the particle size is decreased and consequently the oxygen vacancy at the surface is increased. The oxygen vacancies create exchange interactions between the individual spin moments of Ce ions. Ge et al. [25] has observed ferromagnetism with an Ms value of 0.0057 emu/g of CeO_2 nanocubes having an average size of 5.3 nm. The authors suggest that the oxygen vacancies are mainly responsible for the RTFM in CeO_2 nanocubes. In order to use CeO_2 NPs for applications in various fields, it is necessary to produce ultrafine CeO_2 NPs with desired shape and size with a low degree of agglomeration and monodispersed size distribution. The nanocrystalline structure with monodispersed size distribution or low degree of agglomeration enhances the performance of the nanostructured materials.

In view of the above studies on CeO_2 NPs and their applications in various fields, a systematic report on size dependent change in optical and magnetic properties of CeO_2 NPs is still lacking. Furthermore, in addition to the role of shape and size in modifying the optical and magnetic properties of the nanostructured materials, the degree of distribution (dispersed nature of nanostructures) also affects these properties significantly. Therefore, it is thought worthwhile to perform a systematic study on the influence of size and dispersive nature on the optical and magnetic properties of CeO_2 NPs. In the present study, well dispersed CeO_2 NPs of various sizes have been prepared using a very simple and low cost sol-gel method. In order to vary the size of CeO_2 NPs, the sol-gel derived powder is calcined at 600˚, 700˚ and 800 ˚C. The size and shape of the synthesized powder samples were determined by analyzing the TEM and XRD data. The optical and magnetic properties of the synthesized samples were investigated by UV-VIS spectroscopy, Raman spectroscopy and VSM measurements. The author believes that the present study may provide a complete understanding of size dependence of both, optical and magnetic properties of highly dispersed CeO_2 NPs.

5.2 Experimental Techniques

5.2.1 Synthesis

Cerium ammonium nitrate and ammonium hydroxide were purchased from SRL, India and used without further purification. Cerium ammonium nitrate is used as main precursor for synthesizing CeO_2 NPs. 2.7 gm of cerium ammonium nitrate was dissolved in 100 ml deionized water to make a 0.05 M solution of cerium ammonium nitrate. The mixed

solution was kept for magnetic steering for 2 hours. While steering the mixed solution, 5ml of 1M ammonium hydroxide was added drop-wise to the solution. After mixing the ammonium hydroxide solution, the pH of the solution turned out to be 10. The steering of the mixed solution was continued for another 4 hours at 30 ^{0}C. The yellow color of cerium hydroxide CeO_2 was obtained as precipitate from the final solution. The yellow precipitate was washed several times and calcined at 600^0, 700^0 and 800 ^{0}C for 8 hours to obtain desired size of the synthesized samples. A schematic presentation of the reaction mechanism for the formation of different size of CeO_2 NPs has been illustrated in Fig. 5.1.

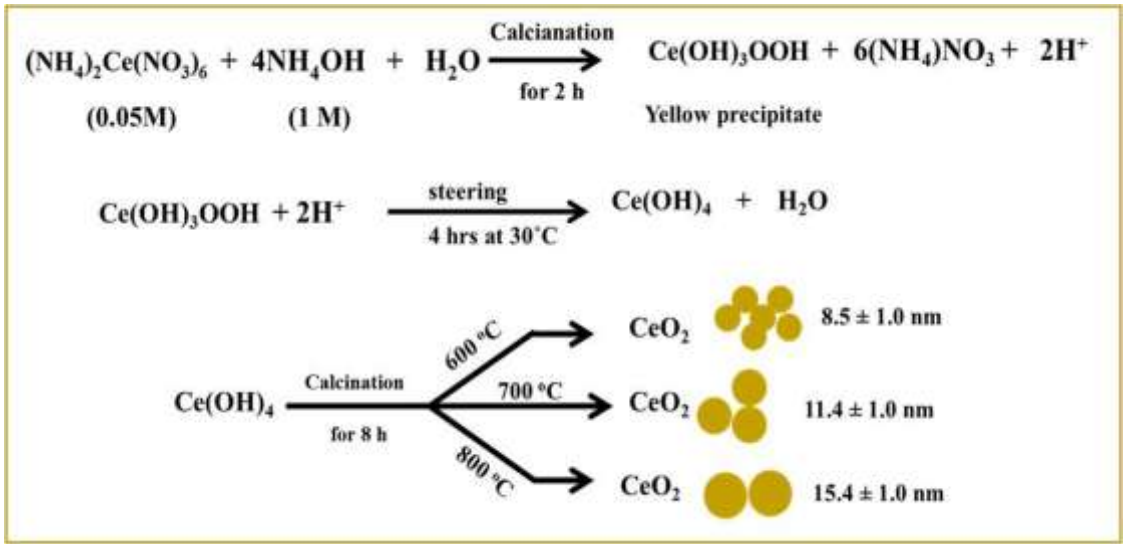


Fig. 5.1 Schematic representation of experimental process of CeO_2 nanostructures synthesized at 600˚, 700˚ and 800˚C.

5.2.2 Characterization

The synthesized powder samples calcined at 600^0, 700^0 and 800 ^{0}C were collected for analysis. The structural properties of the calcined samples were characterized by XRD with

CuKα radiation (λ = 1.54 A^0) in the 2θ range of 20^0-90^0. The XRD data were used to determine crystalline phase of the synthesized powder samples. Surface morphology of the synthesized product was examined through the field emission scanning electron microscope (FE-SEM) SIRIDN 2000. The detailed structural features like shape, size and dispersive behavior of the synthesized products were investigated by HR-TEM measurements using a TEM, Tecnai G20 S-Twin. The optical characterization of the synthesized samples was done using a Raman set-up (Renishaw, UK,) and UV-VIS spectroscopic measurements. The UV-VIS absorption spectra of the synthesized samples were obtained using PerkinElmer (Lambda35) UV-VIS spectrometer. The Raman measurements of the synthesized samples were performed at room temperature in the range of 400-500 cm^{-1} by using the 514.5 nm laser line of an Ar^+ ion laser. In order to study the magnetic properties of the synthesized samples, the magnetization measurements were done using VSM at room temperature.

5.3 Results and Discussion

5.3.1 XRD

The structural analysis of the prepared samples has been carried out based on the XRD pattern. The XRD patterns of powder samples calcined at 600^0 (i), 700^0 (ii) and 800^0C (iii) are shown in Fig. 5.2a. These XRD patterns are indexed with the JCPDS card no.81-0792. Nine diffraction peaks were observed at 2θ values, 28.46^0, 33.07^0, 47.45^0, 56.17^0, 59.08^0, 69.43^0, 76.52^0, 79.10^0 and 88.44^0 corresponding to reflections from the (111), (200), (220), (311), (222), (400), (331), (420) and (422) planes of the cubic crystalline phase of CeO_2.

The sharp and strong peaks indicate good crystallization of the samples. No additional peaks pointing to impurities were observed, which reveals the high purity of the synthesized samples. Here, it is interesting to note that the value of full width at half maximum (FWHM) of the most intense XRD peak corresponding to the (111) plane is increased with decreasing the calcination temperature. The increase of the FWHM of the XRD peak with decreasing calcination temperature is the signature for a formation of nano-sized CeO_2 [5]. Furthermore, the variation of the FWHM of the XRD peaks, as shown in Fig. 5.2b, with calcination temperature confirms the formation of CeO_2 NPs of various sizes. In addition to the change in FWHM with calcination temperature, the XRD patterns corresponding to the (111) plane of the samples calcined at 700 ^{0}C and 800 ^{0}C show a down shift in their 2θ values compared to the value observed for the sample calcined at 600 ^{0}C. The peak positions shift to the lower angle side with increasing the calcination temperature. It means that the spacing between the lattice planes corresponding to the peaks is changed. The increase of the intensities of the XRD peaks with increasing temperature from 600˚-800 ^{0}C indicates an improvement in crystalline quality of the synthesized samples. The crystallite sizes (D) have been estimated by applying the Scherrer formula: $D = 0.9\lambda / (\beta\cos\theta)$ where λ, β and θ are the X-ray wavelength, FWHM of the diffraction peak and the Bragg's diffraction angle, respectively. The average value of crystallite size was calculated to be ~ 9.0, ~ 11.0 and ~ 15.0 nm for the samples calcined at 600^0, 700^0 and 800 ^{0}C, respectively. The lattice parameters of CeO_2 nanostructures calcined at 600^0, 700^0 and 800 ^{0}C have been calculated using the following relation and the

calculated values are presented in Table 5.1.

$$d = a/(h^2+k^2+l^2)^{1/2}$$

here, d is the inter-planer spacing, a is the lattice constant and h, k, l are the miller indices of plane (111).

The value of lattice constant is decreased with increasing the calcinations temperature. It may be due to the fact that as the temperature increases, the Ce^{4+} ions reduce to Ce^{3+} ions and create a continuous series of disordered oxygen vacancies in the CeO_2 NPs [26]. As the synthesized CeO_2 NPs have cubic fcc fluorite structure, in which Ce^{4+} cations are situated at each corner as well as at the six faces of the cube. Each Ce^{4+} cation is surrounded by eight O^{2-} anions and each O^{2-} anion is coordinated with four Ce^{4+} cations. As temperature increases, the number of O^{2-} anions decreases from eight to seven and introduces Ce^{3+} ions into the crystal lattice by creating oxygen vacancies. The ionic radius (1.034 Å) of Ce^{3+} is higher than that of Ce^{4+} ion (0.92 Å). It leads to distortion of the crystal lattice and resulting the change in Ce-O bond length [27]. Phokha et al. [28] reported that the lattice constants are decreased with increasing crystallite size. According to them, the introduction of Ce^{3+} ions into the crystal lattice, which have a higher ionic radius (1.034 Å) compared with the Ce^{4+} ions (0.92 Å), causes a reduction of the lattice constants. The introduction of Ce^{3+} ions is also responsible for the lattice distortion by introducing a change of the inter-planar spacing with changing particle size, as we have observed in the present study. It confirms that the lattice undergoes a strain effect when the size is reduced. This is in good agreement with an earlier report [22].

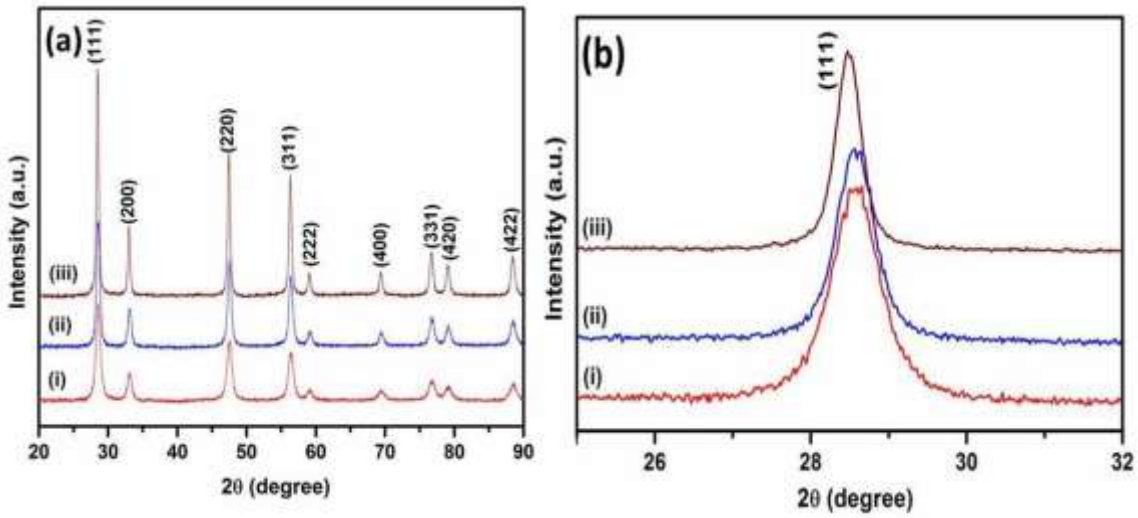


Fig. 5.2 (a) XRD pattern of CeO_2 nanostructures synthesized at (i) 600˚, (ii) 700˚ and (iii) 800˚C. (b) magnified XRD spectra showing the shifting of (111) plane with increasing calcination temperature.

Table 5.1 Calculated values of particle size, lattice constants and optical band gap of CeO_2 NPs synthesized at different calcination temperatures.

Calcination temperature (˚C)	Crystallite size using XRD (nm)	Particle size using TEM (nm)	Particle size using Raman (nm)	Lattice constant (Å)	Optical Band Gap (eV)
600	9.0	8.5 ± 1	9.63	5.412	3.88
700	11.0	11.4 ± 1	15.61	5.382	3.80
800	15.0	15.4 ± 1	21.33	5.347	3.71

5.3.2 TEM and SEM

Fig. 5.3a-b shows surface morphology of CeO_2 NPs investigated through FE-SEM micrographs. It can be seen that particles consist of spherical grains with size in the range of 5-15 nm. The shape and size of the CeO_2 NPs synthesized at different calcination temperature were further investigated through TEM micrographs. The TEM micrographs of CeO_2 NPs calcined at 600^0 and 800 ^{0}C are presented in Fig. 5.3c and 5.3f, respectively. By looking at the TEM micrographs, it is quite apparent that the NPs were highly dispersed in nature and the shape of NPs was nearly spherical. HR-TEM micrograph [Fig. 5.3d] of the nanoparticles shows well defined lattice fringes with an interplanar spacing of 0.32 nm and 0.28 nm which correspond to (111) and (200) planes, respectively. The average value of particles size was determined by a histogram as shown in Figs. 3e and 3g. The particle size of the CeO_2 NPs calcined at 600^0, 700^0 and 800 ^{0}C was calculated to be 8.5 ± 1 11.4 ± 1 and 15.4 ± 1 nm, respectively (see Table 5.1). The particle size estimated using the TEM micrographs are in good agreement with the values of the crystallite size calculated using the XRD data.

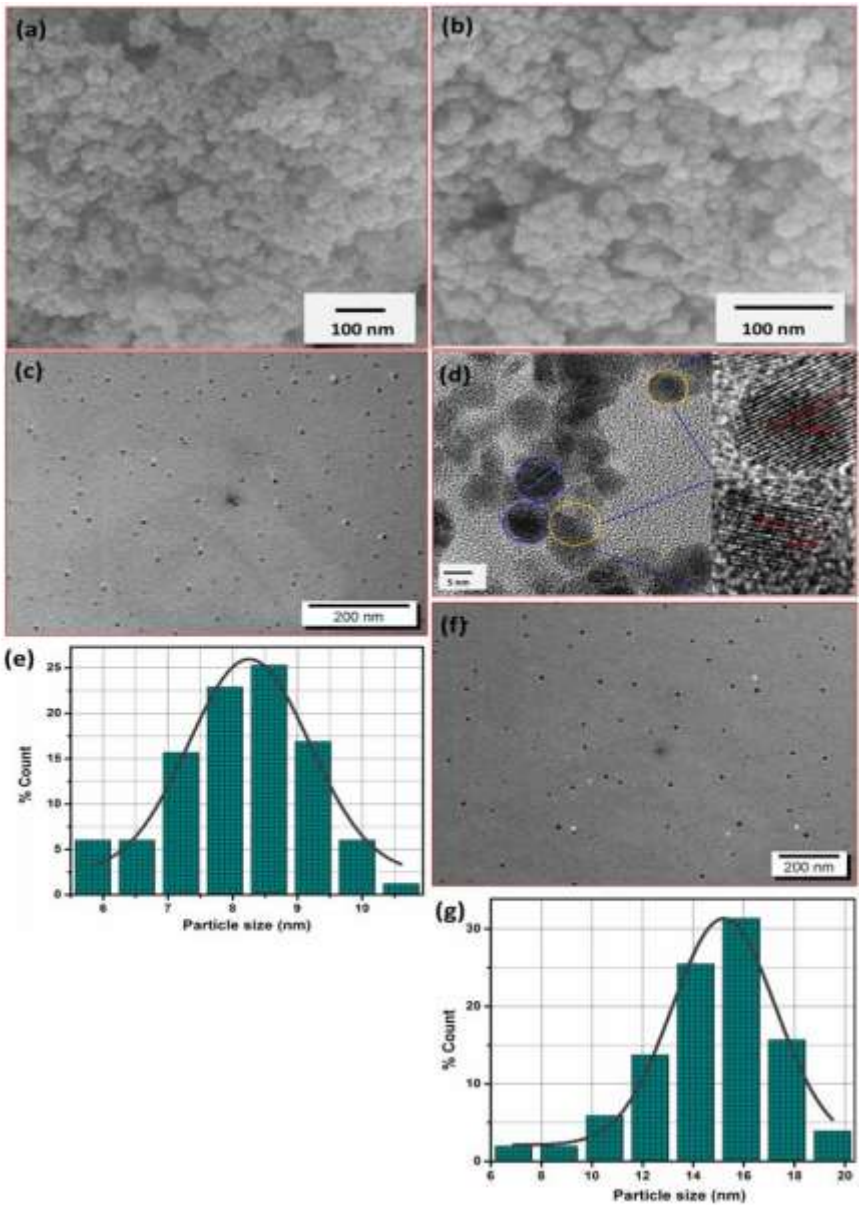


Fig. 5.3 SEM micrograph of CeO_2 nanostructure synthesized at 600˚ (a) at low magnification and (b) at high magnification, (c) TEM micrographs, (d) HR-TEM micrograph and histogram of CeO_2 NPs synthesized at (e) 600˚ (f) TEM micrograph and (g) histogram of CeO_2 nanostructure synthesized at 800˚C.

5.3.3 UV-VIS spectroscopy

In order to study the size dependent variation of the optical band gap of the CeO_2 NPs, UV-VIS absorption spectroscopy was carried out. The samples calcined at 600^0, 700^0 and 800 ^{0}C were dispersed in ethanol for performing the UV-VIS. absorption measurements. The absorbance spectra of all three samples were recorded in the spectral range 200-800 nm. The absorption spectra of CeO_2 NPs calcined at 600^0 (8.5 ± 1nm), 700^0 (11.4 ± 1 nm) and 800 ^{0}C (15.4 ± 1 nm) are shown in Fig. 5.4a. The absorption maxima are observed at ~300, ~315 and ~325 nm for the particle size 8.5 ± 1.0, 11.4 ± 1.0 and 15.4 ± 1.0 nm, respectively. It is pertinent to note that the absorption maximum shows a significant red shift with increasing particle size. This implies that the optical band gap is reduced when particle sizes become smaller. The UV-VIS data are used to estimate the optical band gap of CeO_2 NPs calcined at 600, 700, and 800 ^{0}C by extrapolating the linear portion of $(\alpha h\nu)^2$ vs hν plots to intercept the photon energy axis as shown in Fig. 5.4b-d. The value of optical band gap for the CeO_2 sample calcined at 600, 700 and 800^0C is calculated to be 3.88, 3.80 and 3.71 eV, respectively. The decrease in optical band gap may be due to the increase of particle size of CeO_2 nanoparticles due to presence of oxygen vacancy as defects. The optical band gap calculated for various sizes of NPs are given in Table 5.1. Phokha et al. [28] had calculated the optical band gap for various sizes of CeO_2 NPs starting from 9.43 ± 1 to 15.6 ± 1 nm and the values were reported to be in the range of 3.0 to 3.1 eV. In the study, they found that the optical band gap is increased with increasing particle size, which contradicts to our results. Additionally, we would like to note that the change of the optical

band gap reported by Phokha et al. [28] is rather small (0.1 eV). Supporting our findings, also Tsunekawa et al. [30] reported that the optical band gap, in general, increased with decreasing particle size due to the confinement effect. Phokha et al. [28] have explained the increase of optical band gap with increasing particle size in terms of change in cerium valence due to the presence of oxygen vacancies at surface of the NPs. In the present study, the optical band gap was found to decrease with increasing particle size, which is well in accordance with the quantum confinement effect as described by the following relationship:

$$E_g = E_g^0 + [h^2/8\mu R^2] - [1.8e^2/4\pi\varepsilon R]$$

where E_g^0 is the energy band gap for the bulk material, h is the Planck's constant, R is the radius of the nanoparticles, $1/\mu = 1/m_e + 1/m_h$ with m_e and m_h being the electron and hole effective masses, respectively, e is the electronic charge and ε is the dielectric constant [31]. The value of optical band gap reported in this work is relatively higher than that of the earlier reports [32-33] for the same range of particle size. Our result is consistent with the values reported by Masui et al. [34]. They also have observed that the value of direct band gap is decreased with increasing the particle size of CeO_2 NPs. CeO_2 belongs to a rare earth class oxide, which shows charge transfer transitions, and it is a common phenomenon to all rare earth ions. Thus, the optical properties of CeO_2 NPs are determined by charge transfer transitions that can be identified by broad absorption bands [26]. Patsalas et al. [35] have reported that the band gap of CeO_2 NPs changes with change of Ce^{3+} concentration. As the particle size increases, the concentration of Ce^{3+} also increases,

which causes to decrease band gap of CeO_2 NPs. In the present study, the decrease of band gap with increasing particle size could be due to (i) the quantum confinement effect as described by the above equation and/or (ii) the increase of the concentration of Ce^{3+} ions in the CeO_2 NPs at higher calcination temperature. The higher concentration of Ce^{3+} ions may create localized energy states within the band gap due to the presence of oxygen vacancies, causing a red shift of the optical band gap energy with increase of particle size.

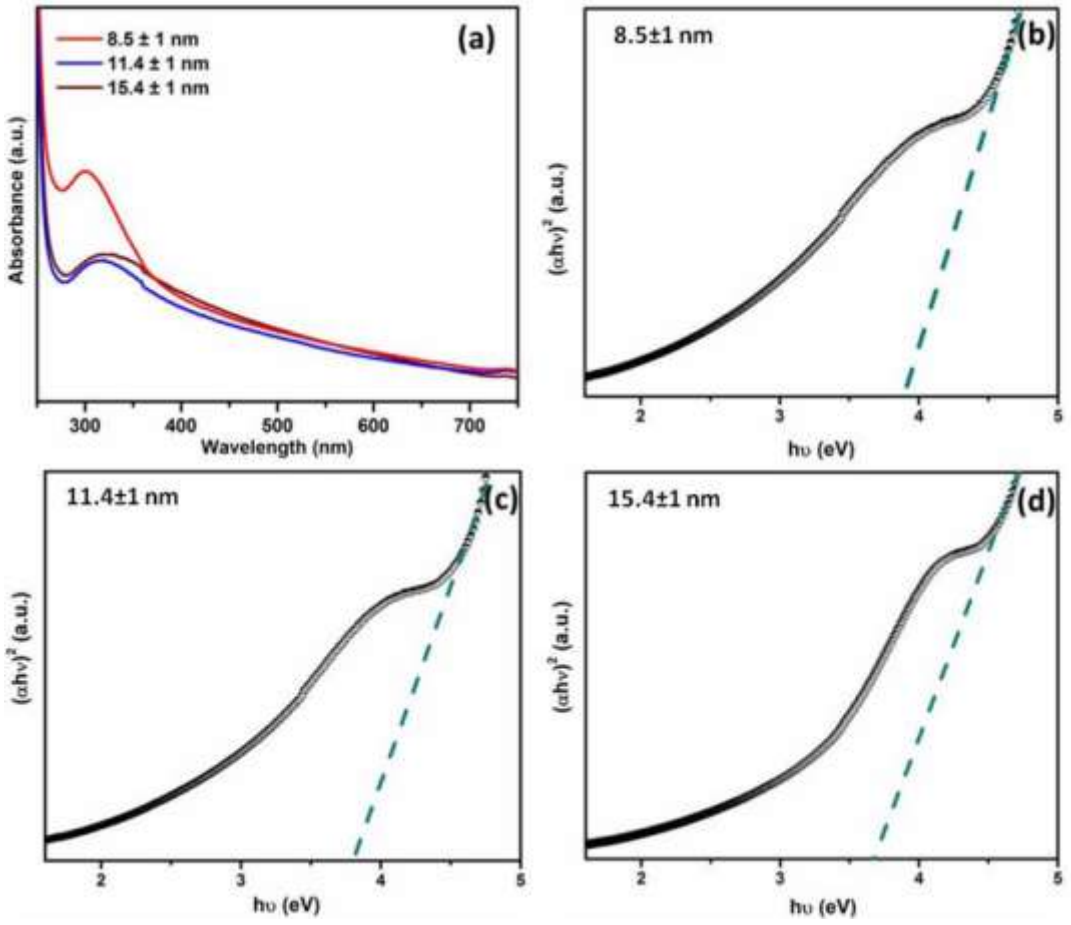


Fig. 5.4 (a) Room temperature UV-VIS spectra of CeO_2 NPs for the particle size 8.5±1, 11.4±1 and 15.4±1 nm and (b-d) tauc plots for determination of optical band gap.

5.3.4 Raman spectroscopy

Raman spectroscopy is a nondestructive tool for assessing the quality of crystalline materials. Since, Raman spectra yield the vibrational energies of the molecules, they allow for an investigation of structures on a molecular level and, therefore, Raman spectroscopy is of great importance for characterizing the materials, especially to nanostructured samples. A small change in structure can easily be seen by looking at the Raman features of the materials. The Raman spectra of CeO_2 NPs of particle sizes 8.5 ± 1.0, 11.4 ± 1.0 and 15.4 ±1.0 nm recorded for a spectral range of 400-500 cm^{-1} are presented in Fig. 5.5a-b. The Raman spectra of all the samples were measured using an excitation wavelength of 514.5 nm and an excitation power at the sample of 8 mW. An 180^0 scattering geometry was used to collect the Raman scattered signal from the powder sample in a micro Raman setup equipped with a 50 X objective. In order to see the effect of particle size on the Raman bands, the Raman spectra of bulk CeO_2 material has also been recorded. The Raman spectra recorded for particle sizes 8.5 ± 1.0, 11.4 ± 1.0 and 15.4 ±1.0 nm showed a peak at ~ 461, ~ 462 and ~ 463 cm^{-1}, respectively. These Raman peaks are assigned to the first order longitudinal optical phonon mode (1LO). No any other peak was observed in the Raman spectrum of bulk CeO_2, as it was observed by Spanier et al. [36]. The appearance of single Raman peak for each particle size confirms the formation of CeO_2 NPs with very high crystallinity. The 1LO line belongs to a triply degenerate F_{2g} symmetric breathing mode of the oxygen atoms around the cerium ions [37]. Since, the Ce-O_8 vibrational unit is

very sensitive to any disorder in the oxygen sublattice, the Raman line observed is a direct measure of the sublattice quality [32, 38-40].

The asymmetrical feature appeared in the Raman peak towards the lower wavenumber side for the CeO_2 NPs compared to its bulk form indicate that the synthesized particles are in nano scale regime. It is in good agreement with the XRD results. The Raman peak at ~ 461 cm^{-1} shifts to higher wave number by 3 cm^{-1} with increasing the particle size from 8.5 to 15.4 nm. This shift of the Raman band with particle size may be due to the change of the Ce-O_8 bond length resulting from the lattice distortion. Other factors, such as phonon confinement and variations in phonon relaxation, may also be responsible for the shift of the Raman band to higher vibrational energies and its line broadening [41]. The effect of the particle size of the CeO_2 NPs on the Raman spectra is reflected by the enhanced asymmetrical feature towards the low-wavenumber side of the Raman peaks. Both, the line broadening and increase of asymmetry may be attributed to the reduction of the phonon life time in the nano crystalline regime [42-43]. Other possible explanations for the observed features of the appearance of asymmetry in Raman peak are phonon confinement, strain, size distribution, defects and changes of the phonon relaxation with particle size [36]. In case of bulk materials, the phonon at q=0 exclusively participates in the Raman scattering. However, as the dimensions are reduced down to the nanometer regime, the scattering volume in the reciprocal space is increased, which causes a relaxation of this selection rule for Raman scattering. In order to explain the size dependence of shape of Raman peak for nanostructured materials, Richter et al. [44] used a

Gaussian weighting function to model Raman scattering at wave vectors way from the zone center in low dimension materials. For a spherical nanostructure, the Raman intensity profile can be modeled by using following equation [36].

$$I(\omega, L) = \int \frac{\exp\left(\frac{-q^2 L^2}{8\beta}\right)}{\left[\omega - \{\omega_i(q) + \Delta\omega_i(q, L)\}\right]^2 + (\Gamma/2)^2} d^3q$$

where Γ is the FWHM of the bulk Raman peak, q is the wave vector, and $\omega_i(q)$ is the phonon dispersion for the selected mode. The particle size of the CeO_2 nanostructures can also be estimated by FWHM from the Raman bands using the following equation [39, 40, 45] (results are given in Table 5.1):

$$\Gamma(\text{cm}^{-1}) = 10 + \frac{124.7}{L}$$

where $\Gamma(\text{cm}^{-1})$ is the FWHM of Raman active mode and L is the particle size of the nanostructure. The particle size of the samples calcined at 600, 700 and 800 ^{0}C has also been calculated using the Raman data with the help of above equation and the values thus calculated are given in Table 5.1. The particle size calculated by Raman data is slightly overestimated compared to the particle size calculated from XRD and TEM measurements. In general, a narrow Raman peak points to a nanostructure with perfect crystal structure while a broad Raman line indicates polycrystalline nature of the sample [46]. Judging from the Raman spectra depicted in Fig. 5.5, one can suggest that the synthesized NPs are highly crystalline and relatively impurities free, which is reflected by the small line width and

rather symmetric line profiles. The shifting of the peaks may be ascribed to the particle size effect [47]. This phenomenon plays a noteworthy character in determining the different properties of nano crystals by changing the energy states of the surface atoms [48-49].

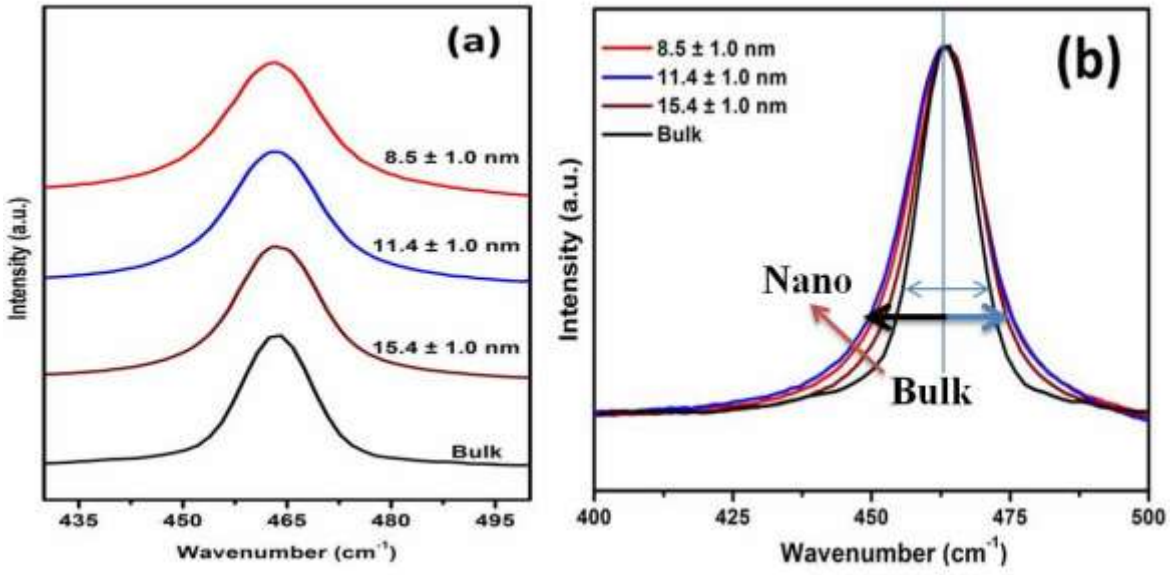


Fig. 5.5 (a) Raman spectra of CeO_2 NPs for the particle size 8.5±1, 11.4±1 and 15.4±1 nm and (b) appearance of asymmetrical features in the Raman peak with increasing particle size.

5.3.5 Magnetic properties

In order to explore the size dependent magnetic properties of the synthesized CeO_2 NPs, magnetic hysteresis measurements were carried out using VSM at room temperature with a magnetic field ranging from -1.5 T to +1.5 T. The M-H curves for various sizes of CeO_2 NPs are shown in Fig. 5.6a-c. The hysteresis loop does not saturate up to the maximum applied magnetic field values (1.5 T). The non-saturation of the hysteresis loop up to

applied magnetic field of 1.5 T indicates that the synthesized samples are only weakly ferromagnetic in nature at room temperature. The values of the magnetic parameters such as the saturation magnetization (M_s), the remanent magnetization (M_r) and the coercivity (H_c) for the CeO_2 NPs of particle size 8.5 ± 1.0, 11.4 ± 1.0 and 15.4 ±1.0 nm were calculated using the hysteresis curves of the respective size and the results are presented in Table 5.2. The values of anisotropy constant (K) and magneton number (n_B) have also been calculated for the CeO_2 NPs using the following equations, respectively [50] and values thus obtained are also given in Table 5.2.

$$H_c = \frac{0.96K}{Ms} \text{ and } n_B = \frac{M.wt \times M_s}{5585}$$

The calcination temperature is an important factor during the synthesis for varying the size of NPs. It affects the crystallinity as well as the size of the synthesized samples. Therefore, the variation of the calcination temperature during the synthesis may cause changes in size and morphology of the sample, which finally make an impact on the values of magnetic parameters listed above. In fact, the change in magnetic behavior of the NPs arises from the antagonism between size and shape anisotropy of the NPs [50]. The value of H_c is increased consistently with increasing the particle size from 8.5 to 15.4 nm. It may be due to the enhanced anisotropy caused by the increased crystallinity at higher calcination temperatures. The high value of H_c at high calcination temperature directly reflects the single crystalline nature of the material, which has a noticeable influence on the magnetic properties of the NPs. It is well known that the symmetrically shaped nanoparticles, such

as sphere-like structures which only have little shape anisotropy exhibit crystalline anisotropy due to single crystalline nature which influences the value of coercivity [51]. The increase in the value of the magneton number (n_B) with particle size also points to the enhancement of the magnetic properties of CeO_2 NPs. The value of Ms is increased from 2.6 x 10^{-3} to 16.5 x 10^{-3} emu/g by increasing the particle size from 8.5 to 15.4 nm. These values are higher than that of the Ms value reported in literature for pure CeO_2 NPs [17, 24]. Sundaresan et al. [17] reported RTFM with an Ms value of ~ 1.9 x 10^{-3} emu/g for CeO_2 NPs of particle size ~ 15 nm. Here, we would like to note that in the present study the value of Ms obtained for same particle size is significantly higher (8 times) than that of Ms value reported in earlier study [17]. The increase of Ms value with particle size implies that the CeO_2 NPs are gradually become a strong magnet as the particle size is increased from 8.5 to 15.4 nm. Further, the value of the Mr is also increased consistently from 0.7 x 10^{-3} to 5.7 x 10^{-3} emu/g by increasing the size of the NPs. By looking at the data presented in Table 5.2, it is quite clear that the magnetic parameters, Ms, Mr and Hc, depend significantly on size and structure of the CeO_2 NPs [52]. The increased values of Ms and Mr with increasing the particle size of CeO_2 NPs may also be explained in terms of high density of oxygen vacancies (defects) on nanostructured surface at higher calcination temperatures. As it was already discussed above that at higher calcination temperatures, the Ce^{4+} ions change to Ce^{3+} ions and, as a consequence, a high number of oxygen vacancies are induced in the lattice. This high concentration of Ce^{3+} ions may be responsible for the presence of more oxygen vacancies in the samples, which causes more coupling between

the individual magnetic moments of the Ce ions, leading to an increase of the Ms value with the increase of particle size [38]. When the Ce^{4+} changes to Ce^{3+}, an unpaired spin of f orbits of Ce atom is generated that gives rise to the net spin and thus, magnetism is induced [53]. The RTFM may arise due to spin coupled from a nearest-neighbor interaction by double exchange (Ce^{3+}-O-Ce^{4+}) or super exchange (Ce^{3+}-O-Ce^{3+}) mechanism by charge transfer transition between O (2p) and Ce (4f) energy bands [54]. Ge et al. [25] had reported that the oxygen vacancies are responsible for the generation of magnetic moment by polarizing spins of f electrons of cerium (Ce) ions located around the oxygen vacancies, which results ferromagnetism in pure CeO_2 nanoparticles. These authors showed theoretically that there is no magnetic moment in CeO_2 without oxygen vacancies, which confirms the paramagnetic behavior of CeO_2 at room temperature. In the present study, we have discussed in the XRD section that the number of oxygen vacancies is increased as calcination temperature is increased. Thus, the possible mechanism to explain the RTFM of CeO_2 NPs and the increase of Ms value with increasing particle size is the oxygen vacancies present in the CeO_2 matrix that induce ferromagnetic coupling originating from the exchange interaction between $4f^1$ spin of Ce^{3+} and oxygen vacancies [17-18].

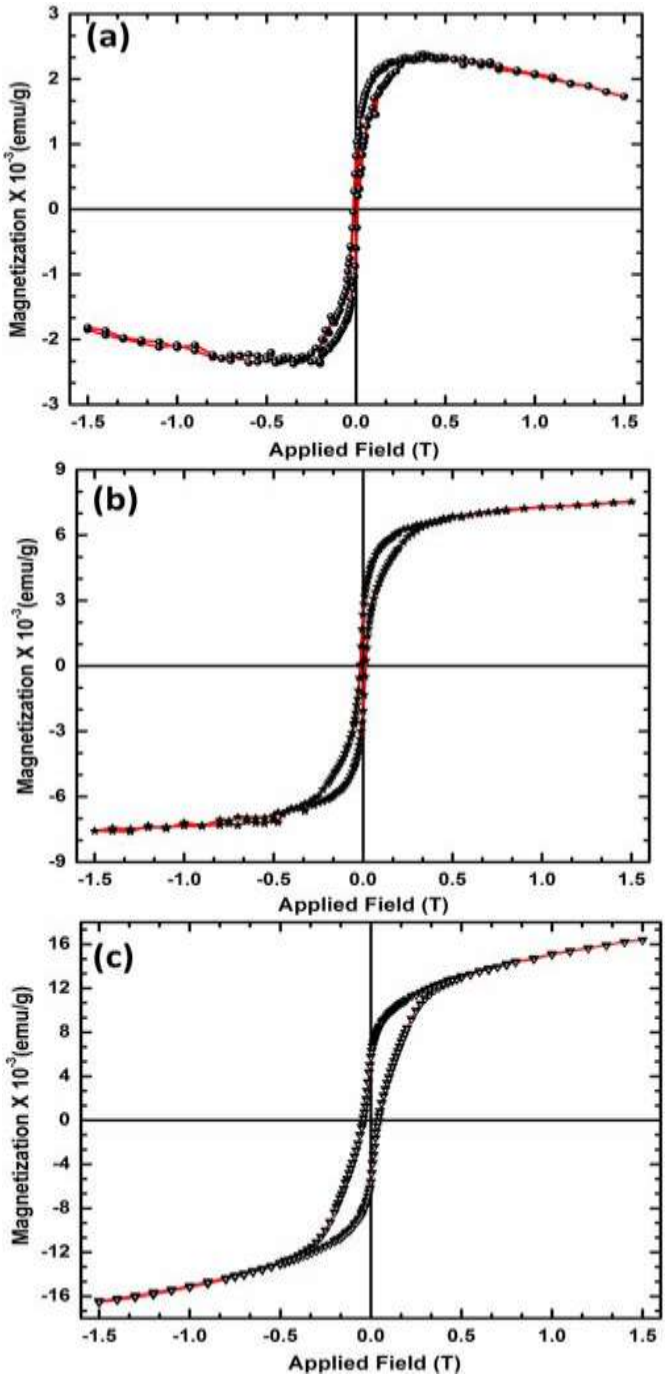


Fig. 5.6 Room temperature M-H curve of CeO_2 NPs for the particle size (a) 8.5±1, (b) 11.4±1 and (c) 15.4±1 nm, respectively.

Table 5.2 Calculated values of magnetic parameters; Ms, Mr, Hc, K and n_B of CeO_2 NPs of sizes 8.5 ± 1.0, 11.4 ± 1.0, 15.4 ± 1.0 nm.

Particle size (nm)	Saturation Magnetization Ms (emu/g)	Remnant Magnetization Mr (emu/g)	Coercive Field Hc (Oe)	Anisotropy constant K (erg/g)	Magneton number n_B (μ_B)
8.5 ± 1.0	2.6×10^{-3}	0.7×10^{-3}	111	0.301	0.08×10^{-3}
11.4 ± 1.0	7.8×10^{-3}	2.2×10^{-3}	144	1.170	0.24×10^{-3}
15.4 ± 1.0	16.5×10^{-3}	5.7×10^{-3}	415	7.132	0.50×10^{-3}

5.4 Conclusion

Monodispersed spherical CeO_2 nanoparticles of size 8.5 ± 1.0, 11.4 ± 1.0 and 15.4 ± 1.0 nm have been synthesized by the sol-gel method. Structural, optical and magnetic properties of as-prepared samples were investigated by XRD, TEM, SEM, UV-VIS, Raman and VSM measurements. The UV-VIS study shows a red shift of the absorption maximum, i.e. the decrease of optical band gap, with increasing particle size. This may be explained in terms of quantum confinement effect. Further, it could also be due to additional localized states created by the oxygen vacancies, which arise from the conversion of Ce^{4+} to Ce^{3+} ions at higher calcination temperature. Raman spectra show a weak asymmetrical feature in Raman peak at ~ 461 cm^{-1} (1LO) with reduction of particle size, which is a clear indication for the formation of nano-sized CeO_2. VSM measurements revealed that the synthesized CeO_2 NPs are weak ferromagnetic in nature. The values of the Ms, Hc and Mr are increased with increasing particle size. This may be due to different

effects; (i) the variation of calcination temperature may change the size and morphology of the sample. This finally would make an impact on the values of magnetic parameters, which can be confirmed by the increased value of anisotropy constant (K) of ~ 6.8 erg/g with increasing particle size, (ii) the higher concentration of oxygen vacancies is coupled to an increased number of Ce^{3+} ions that activate more coupling between the individual magnetic moments of the Ce ions (iii) the oxygen vacancies may also produce magnetic moment by polarizing spins of the f electrons of the cerium (Ce) ions located around the oxygen vacancies.

References

[1] B. C. Viana, O. P. Ferreira, A. G. S. Filho, C. M. Rodrigues, S. G. Moraes, J. M. Filho, O. L. Alves, J. Phys. Chem. C, 2009, **113**, 20234.

[2] A. Medalia, B. Byrne, Anal. Chem., 1951, **23**, 453.

[3] Z. Y. Hu, S. Haneklaus, G. Sparovek, E. Schnug, Commun. Soil Sci. Plan., 2006, **37**, 1381.

[4] F. Zhang, S.-W. Chan, J. E. Spanier, E. Apak, Q. Jin, R. D. Robinson, I. P. Herman, Appl. Phys. Lett., 2002, **80**, 127.

[5] C. Hu, Z. Zhang, H. Liu, P. Gao, Z. L. Wang, Nanotechnology, 2006, **17**, 5983.

[6] H. Gu, M. D. Soucek, Chem. Mater., 2007, **19**, 1103.

[7] T. Pirmohamed, J. M. Dowding, S. Singh, B. Wasserman, E. Heckert, A. S. Karakoti, J. E. S. King, S. Seal, W. T. Self, Chem. Commun., 2010, **46**, 2736.

[8] V. K. Ivanov, A. B. Shcherbakov, A. V. Usatenko, Russ. Chem. Rev., 2009, **78**, 855.

[9] A. H. Morshed, M. E. Moussa, S. M. Bedair, R. Leonard, S. X. Liu, N. El-Masry, Appl. Phys. Lett., 1997, **70**, 1647.

[10] C. Korsvik, S. Patil, S. Seal, W. T. Self, Chem. Commun., 2007, **14**, 1056.

[11] S. M. Hirst, A. S. Karakoti, R. D. Tyler, N. Sriranganathan, S. Seal, C. M. Reilly, Small, 2009, **5**, 2848.

[12] M. Lira-Cantu, F. C. Krebs, Sol. Energy Mater. Sol. Cells, 2006, **90**, 2076.

[13] J. Kašpar, P. Fornasiero, M. Graziani, Cat.Today, 1999, **50,** 285.

[14] N. Kakuta, N. Morishima, M. Kotobuki, T. Iwase, T. Mizushima, Y. Sato, S. Matsuura, Appl. Surf. Sci., 1997, **121/122** 408.

[15] P. Kaminski, T. Suzuki, H. U. Anderson, Sensors Actuat. B-Chem., 2003, **95,** 73.

[16] H. S. Nalwa (ed.), Magnetic Nanostructures, 2nd edn., American Scientific Publishers, Los Angeles, 2009.

[17] A. Sundaresan, P. Bhargav, N. Rangarajan, U. Siddesh, C. Rao, Phys. Rev. B, 2006, **74** , 161301.

[18] M. Venkatesan, C.B. Fitzgerald, J. M. D. Coey, Nature, 2004, **430**, 630.

[19] H. S. Saini, M. Singh, A. H. Reshak, M. K. Kashyap, Comput. Mater. Sci., 2013, **74**, 114.

[20] S. Asˇkrabic´, Z. Dohcˇevic´-Mitrovic´, A. Kremenovic´, N. Lazarevic´ , V. Kahlenberg, Z. V. Popovic´, J. Raman Spectrosc., 2012, **43**, 76.

[21] J. M. D. Coey, M. Venkatesan, C. B. Fitzgerald, Nat. Mater., 2005, **4**, 173.

[22] J. M. D. Coey, M. Venkatesan, P. Stamenov, C. B. Fitzgerald, L. S. Dorneles, Phys.

Rev. B, 2005, **72**, 024450.

[23] Y. Liu, Z. Lockman, A. Aziz, D. J. Macmanus, J. Phys. Condens. Matter, 2008, **20**, 165201.

[24] S. Y. Chen, Y. H. Lu, T. W. Huang, D. C. Yan, C. L. Dong, J. Phys. Chem. C, 2010, **114**, 19576.

[25] M. Y. Ge, H. Wang, E. Z. Liu, J. F. Liu, J. Z. Jiang, Y. K. Li, Z. A. Xu, H. Y. Li, Appl. Phys. Lett., 2008, **93,** 062505.

[26] P. O. Maksimchuk, A. A. Masalov, Y. V. Malyukin, J. Nano- Electron. Phys., 2013, **5**, 01004.

[27] S. Deshpande, S. Patil, S. V. N. T. Kuchibhatla, S. Seal, Appl. Phys. Lett., 2005, **87**, 133113.

[28] S. Phokha, S. Pinitsoontorn, P. Chirawatkul, Y. Poo-arporn, S. Maensiri, Nanoscale Res. Lett., 2012, **7**, 425.

[29] Q. Y. Wen, H. W. Zhang, Y. Q. Song, Q. H. Yang, H. Zhu, J. Q. Xiao, J. Phys.: Condens. Matter, 2007, **19**, 246205.

[30] S. Tsunekawa, J. T. Wang, Y. Kawazoe, A. Kasuya, J Appl. Phys., 2003, **94**, 3654.

[31] A. K. Chawla, S. Singhal, S. Nagar, H. O. Gupta, R. Chandra, J. Appl. Phys., 2010, **108**, 123519.

[32] S. Maensiri, C. Marsingboon, P. Loakul, W. Jareonboon, V. Promarak, P. L. Anderson, S. Seraphin, Cryst. Growth Des., 2007, **7**, 950.

[33] H. I. Chen, H. Y. Chang, Ceramic Int., 2005, **31**, 795.

[34] T. Masui, K. Fujiwara, K. Machida, G. Adachi, T. Sakata, H. Mori, Chem. Mater., 1997, **9**, 2197.

[35] P. Patsalas, S. Logothetidis, L. Sygellou, S. Kennou, Phys. Rev. B, 2003, **68**, 113308.

[36] J. E. Spanier, R. D. Robinson, F. Zhang, S.-W. Chan, I. P. Herman, Phys. Rev. B, 2001, **63**, 245407.

[37] J. R. McBride, K. C. Hass, B. D. Poindexter, W. H. Weber, J. Appl. Phys., 1994, **76**, 2435.

[38] S. Phoka, P. Laokul, E. Swatsitang, V. Promarak, S. Seraphinc, S. Maensiri, Mater. Chem. Phys., 2009, **115,** 423.

[39] I. Kosacki, T. Suzuki, V. Petrovsky, H. U. Anderson, P. Colomban, Solid State Ionics, 2002, **149**, 99.

[40] I. Kosacki, V. Petrovsky, H. U. Anderson, P. Colomban, J. Am. Ceram. Soc., 2002, **85**, 2646.

[41] E. K. Goharshadi, S. Samiee, P. Nancarrow, J. Colloid Interface Sci., 2011, **356**, 473.

[42] S. H. Lee, Z. Y. Lu, S. V. Babu and E. Matijevic, J. Materials Res., 2002, **7**, 2744.

[43] C. Laberty-Robert, J. W. Long, E. M. Lucas, K. A. Pettigrew, R. M. Stroud, M. S. Doescher, D. R. Rolison, Chem. Mater., 2006, **18**, 50.

[44] H. Richter, Z. P. Wang, L. Ley, Solid state Commum., 1981, **39,** 625.

[45] W. H. Weber, K. C. Hass, J. R. McBride, Phys. Rev. B, 1993, **48**, 178.

[46] P. Nandakumar, C. Vijayan, M. Rajalakshmi, A. K. Arora, Y. V. G. S. Murti, Physica E, 2001, **11,** 377.

[47] D. S. Chuu, C. M. Dai, Phys. Rev. B, 1992, **45**, 11805.

[48] Q. Jiang, H. X. Shi, M. Zhao, J. Chem. Phys., 1999, **111**, 2176.

[49] C. C. Yang, S. Li, Phys. Rev. B, 2007, **75**, 165413.

[50] M. Srivastava, A. K. Ojha, S. Chaubey, P. K. Sharma, A. C. Pandey, Mater. Sci. Eng. B, 2010, **175**, 14.

[51] M. Srivastava, J. Singh, M. Yashpal, A. K. Ojha, J. Nanosci. Nanotechnol., 2010, **12**, 6248.

[52] M. Srivastava, A. K. Ojha, S. Chaubey, J. Singh, P. K. Sharma, A. C. Pandey, J. Alloys Compd., 2010, **500**, 206.

[53] P. Schio, F. Vidal, Y. Zheng, J. Milano, E. Fonda, D. Demaille, B. Vodungbo, J. Varalda, A. J. A. Oliveira, Phys. Rev. B, 2010, **82**, 094436.

[54] S. Y. Chen, C. H. Tsai, M. Z. Huang, D. C. Yan, T. W. Huang, A. Gloter, J. Phys. Chem. C, 2011, **116,** 8707.

CHAPTER - 6

In-situ synthesis of reduced graphene oxide decorated with highly dispersed ferromagnetic cadmium sulfide nanoparticles and its photocatalytic activity on methylene blue dye under ultraviolet irradiation

In this chapter, a facile one step in-situ solvothermal synthesis method has been used to prepare pure cadmium sulfide (CdS) nanoparticles (NPs), graphene oxide (GO), reduced graphene oxide (rGO) and rGO decorated with highly dispersed CdS NPs. The optical properties of the synthesized samples have been investigated using ultraviolet-visible (UV-VIS) spectroscopy, photoluminescence (PL) spectroscopy and Raman spectroscopy (RS) techniques and a comparative analysis of the results obtained by these techniques have been done. The presence of two distinct Raman peaks in 2D band indicates that the synthesized rGO may be composed of double layers. The room temperature ferromagnetism (RTFM) of CdS NPs decorated over rGO is decreased compared to pure CdS NPs. The rGO-CdS nanocomposites show enhanced photocatalytic activity for photodegradation of methylene blue (MB) dye compared to pure CdS NPs, GO and rGO. Due to enhanced photocatalytic activity of rGO-CdS nanocomposites, it may be used for many practical applications in future nanotechnology.

6.1 Introduction

Among the various carbon based materials, the graphene is a new class of two dimensional (2D) honey comb structure consisting of a mono layer network of sp^2 hybridized carbon atoms. This mono layer of carbon atoms can be wrapped, rolled and stacked to make different structures with various dimensionalities such as; fullerene (0D), carbon nanotubes (1D) and graphite (3D), respectively [1]. The unique single layer network of sp^2 hybridized carbon atoms of graphene opens up new applications in various fields such as; nanoelectronics, biosensors and photovoltaic devices [2]. Since its discovery [3] in 2004, graphene has made an ultimate impact in numerous areas of science and technology due to its remarkable high electron mobility, extremely large surface area, high thermal conductivity, good mechanical stability [4] and low cost simple fabrication process as well as the ability to functionalize its surface easily. These exceptional features of graphene have made it to utilize as a promising supporting material to decorate and stabilize inorganic semiconductor nanostructures to improve its properties for wider applications.

Among various semiconductor materials, cadmium sulfide (CdS) is an important semiconductor with a direct band gap of 2.40 eV. The narrow band gap value (2.40 eV) compared to other metal oxides has made it, as a promising candidate for applications in the field of photocatalysis and optoelectronics [5]. The electron (e^-) - hole (h^+) pair generated by the irradiation of light has made it as a suitable catalyst for enhancement of photocatalytic activity. But, the rapid recombination of the e^-- h^+ pair is a major obstacle that restricts the photocatalytic performance of CdS NPs. In order to enhance the

photocatalytic performance of CdS NPs, the e^-- h^+ pair recombination time for CdS NPs can be delayed and the photogenerated charges can effectively be separated by decorating CdS NPs over the materials with high surface area. On the basis of above discussions, it is reasonable to believe that rGO-CdS nanocomposites should show improved photocatalytic activity. The rGO serves as an excellent platform for CdS NPs based on its high specific surface area and a superior electrical conductivity [6]. The rGO-CdS nanocomposites were studied previously by many research groups [7-8]. However, in these studies the authors have paid attention only to see the photodegradation of dye. They did not study the magnetic and emission properties of rGO-CdS nanocomposites. Further, in most of the studies, the photocatalytic activity of rGO-CdS nanocomposites are reported for organic dyes with visible light only while in best of our knowledge, the photocatalytic activity of rGO-CdS nanocomposites on MB dye under UV light has not been reported yet.

In recent years, grapheme based nanocomposites have been subject of great research interest due to their novel physical and chemical properties [9]. The nanocomposites of graphene with semiconducting materials are capable to generate remarkable properties such as; high specific surface area, high mobility and unique tunable band gap. The composite materials have been recognized as a material of enormous potential that provide superior performance for various specific applications such as; electro-catalysis, supercapacitors, high performance lithium ion batteries etc [6]. In addition, the photogenerated e^-- h^+ pairs with high charge separation efficiency are obtained due to the decoration of semiconductor nanoparticles of controlled shape and size

over well segregated graphene layers. The graphene decorated with semiconductor nanostructures is usually prepared by in-situ growth process such as hydrothermal/solvothermal method in which GO is used as starting material. The oxygen containing functional groups are responsible to control the decoration of nanoparticles on graphene layers without aggregation [6]. GO has a similar structure, as of graphite, in which the plane of carbon atoms is attached by oxygen containing functional groups. These oxygen containing functional groups are responsible to expand the interlayer distance of graphite sheets and to make the sheets hydrophilic. Further, the reduction of GO provide graphene based semiconductor composites with well charge separation capability.

The graphene and its nanocomposites with semiconducting metal oxides have been synthesized and their physical and chemical properties have been well studied by the various research group [8-10]. However, a systematic report on optical and magnetic properties of graphene decorated with well dispersed CdS NPs and its photocatalytic activity on methylene blue (MB) dye under UV irradiation has not been studied yet. In view of above discussed studies on graphene and its nanocomposites with transition metal oxides and chalcogenides and its applications in various fields, it is thought worthwhile to synthesize graphene decorated with well dispersed CdS NPs by a simple synthesis approach and study their optical, magnetic and photocatalytic properties.

Thus, in the present work, I have reported a facile in-situ synthesis approach to decorate CdS NPs with a high degree of dispersion on rGO sheets. The structural, optical

and magnetic properties of CdS NPs decorated over rGO sheets have been investigated by XRD, HR-TEM, UV-VIS spectroscopy, PL spectroscopy, Raman spectroscopy and VSM measurements. The composition of elements present in the synthesized samples was confirmed by the energy-dispersive X-ray spectroscopy (EDX) measurements. In addition to structural, optical and magnetic properties, the photocatalytic response of the synthesized product has also been investigated over MB dye under UV irradiation. The optical, magnetic and photocatalytic properties of pure CdS NPs and those decorated over rGO sheets have been studied and possible mechanism for enhanced photocatalytic activity has also been proposed.

6.2 Experimental Techniques

6.2.1 Synthesis

The synthetic approaches, generally used to prepare graphene based nanocomposites, are mixing of solution, sol-gel and in-situ growth like hydrothermal or solvothermal methods. Actually, two or more methods out of above mentioned synthetic strategy are generally shared to manufacture the graphene based semiconductor nanocomposites. In the present work, in-situ growth of graphene decorated with CdS NPs have been done using solvothermal method using GO as precursors for graphene, and cadmium acetate with sodium sulphide, as precursor for CdS. Ethylenediamine was used as a chelating agent to form highly dispersed CdS NPs. Hydrazine hydrate (N_2H_4) has been used to convert GO into rGO that serves as a support to decorate CdS NPs over rGO sheets. Fig.6.1 demonstrates the scheme of synthesis procedure used to synthesize rGO-CdS

nanocomposites. The in-situ growth processes like, hydrothermal or solvothermal is an effective method for the preparation of graphene based semiconductor nanocomposites with inimitable advantages. In this process, the mixed solution of precursors of graphene and metal compound, functionalized GO and metal salts, respectively, are loaded with or without reducing agents in an autoclave for thermal treatment. During the thermal treatment, graphene based semiconductor nanocomposites is fabricated simultaneously by converting GO into rGO. The presence of oxygen containing functional groups like epoxy, carbonyl, carboxyl and hydroxyl on GO provide the nucleation sites for evenly and mono-dispersed growth of semiconductor NPs on rGO sheets without agglomeration [11].

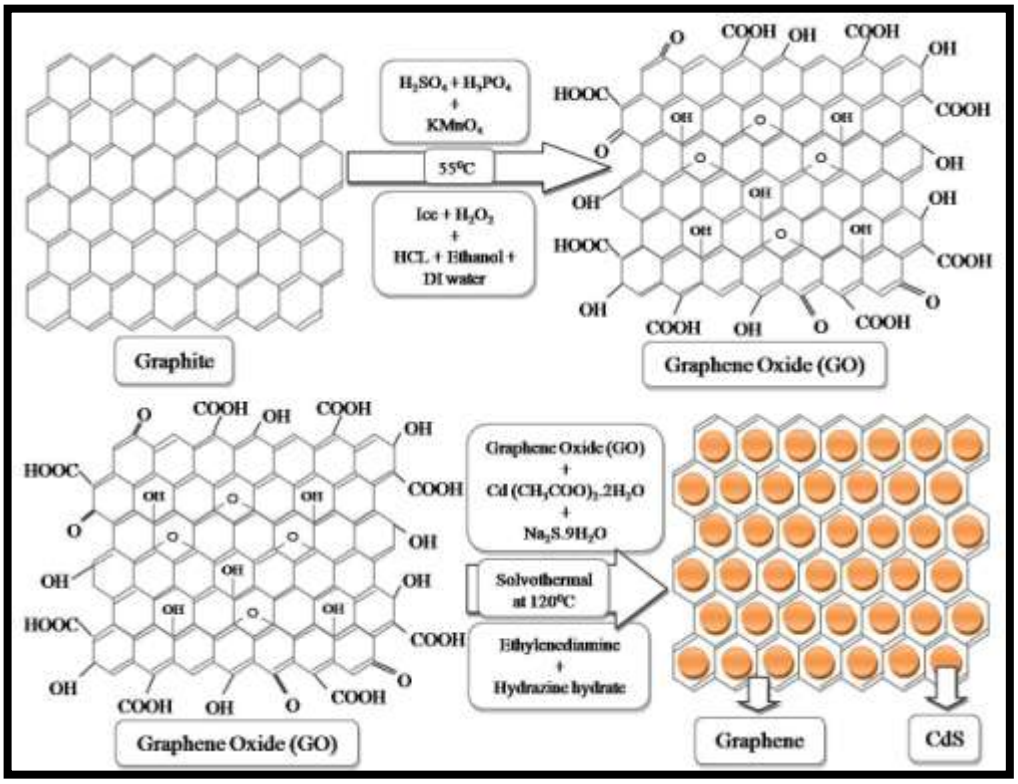


Fig. 6.1 Schematic illustration of the synthesis of rGO-CdS nanocomposites.

6.2.1.1 Synthesis of GO

GO was synthesized using an improved method [12] with some modifications. In general, a mixture of concentrated H_2SO_4 (360 ml) and H_3PO_4 (40 ml) was prepared in a conical flask. The graphite powder (3gm) was mixed slowly into mixture of concentrated H_2SO_4/H_3PO_4 while stirring. The homogeneous solution was made by vigorous stirring for 15 min. Thereafter, the conical flask containing homogeneous solution of concentrated H_2SO_4/H_3PO_4 and graphite was kept in a water bath. 18gm of $KMnO_4$ was added very slowly under vigorous stirring and maintained a temperature of 35˚C of the resultant solution. After mixing of $KMnO_4$ nicely, the water bath was removed and the resultant solution was then heated to 55˚C and stirred for 12 h to complete the oxidation of graphite. During oxidation reaction, the color of the mixture turned out to be dark brown. The reaction was cooled to room temperature after vigorous stirring for 12 h and poured ice, which again produces exothermic reaction by showing purple color of the mixed solution. To stop the oxidation process, 30% H_2O_2 solution was added gradually till the color of the mixed solution turned to bright yellow that indicate a high oxidation level of graphite. The obtained slurry was centrifuged at 4000 rpm for 1 h, and the supernatant was removed. The precipitate was then washed with 200 ml of water, 200 ml of 30% HCl, and 200 ml of ethanol in succession until a pH of 5 was achieved. The remaining solid material was then dried overnight at 40˚C. The obtained desired brown solid powder of GO was collected and stored for further use.

6.2.1.2 Synthesis of rGO

rGO was synthesized by a facile in-situ solvothermal method. For synthesis of rGO, as synthesized brown solid powder of GO (0.02gm) was first dispersed into 40 ml double distilled water under mild condition. The dispersed GO was then exfoliated by using ultrasonication for 1 h, and then 10µl hydrazine hydrate (N_2H_4) were added drop wise into the above mentioned solution under ultrasonication. Thereafter, the solution was transferred to a 50 ml of Teflon lined autoclave and heated at 120°C for 12 h. The autoclave was then cooled to room temperature. Now, the obtained precipitate was washed with double distilled water and ethanol until a pH of 5 of the solution was achieved. The remaining solid material was dried at 60˚C and the resulting black powder of rGO sheets was collected for further use.

6.2.1.3 Synthesis of pure CdS NPs

In order to synthesize pure CdS NPs, 0.533gm (0.05M) of cadmium acetate dihydrate, $Cd(CH_3COO)_2.2H_2O$ was mixed in 40 ml of ethylenediamine ($C_2H_8N_2$) and stirred the resultant solution. Further, 0.480gm (0.05M) of sodium sulfide ($Na_2S.9H_2O$) was added slowly to the obtained solution under vigorous stirring. The resultant solution was then kept for further stirring until the solution was turned to light yellow. Now, the solution was transferred to a 50 ml of Teflon lined autoclave and heated it at 120°C for 12 h. The autoclave was then cooled to room temperature. Now, the obtained precipitate was washed with distilled water and ethanol until a pH of 5 of the resultant solution was achieved. The remaining solid material was dried at 60˚C. The yellow powder of CdS NPs was collected

for further use.

6.2.1.4 Synthesis of rGO decorated with CdS NPs

One step in-situ synthesis of rGO decorated with CdS NPs has been done using solvothermal method. In order to perform in-situ synthesis of rGO sheets decorated with CdS NPs, 0.02gm of GO was first dispersed in 40 ml of $C_2H_8N_2$ solution and stirred the solution. The dispersed GO was then exfoliated by ultrasonication of the solution for 1 h, and then 10µl N_2H_4 was added drop wise into the solution under ultrasonication. Further, 0.533gm (0.05M) of cadmium acetate dihydrate, $Cd(CH_3COO)_2.2H_2O$ and 0.480gm (0.05M) of sodium sulfide, $Na_2S.9H_2O$ was added slowly one by one into the prepared solution under vigorous stirring. The resultant solution was then kept for further stirring until the solution was turned to blackish light yellow. Thereafter, the resultant solution was transferred to a 50 ml of Teflon lined autoclave and heated at 120°C for 12 h. The autoclave was then cooled to room temperature. Now, the obtained precipitate was washed with double distilled water and ethanol until the pH value of solution is reached to 5. The remaining solid material was dried at 60˚C. The dried blackish dark yellow powder was then characterized using different experimental techniques.

6.2.2 Characterization

The crystalline phase of the synthesized samples was analyzed by XRD (Rigaku Smart Lab X-ray diffractometer) with CuKα radiation (λ=0.154 nm). The shape and size of the synthesized samples were investigated by HR-TEM (TEM, Tecnai G20 S-Twin) measurements. EDX measurements were also done for elemental analysis using a Leo1530

VP field emission electron microscope. Raman spectra of the synthesized samples were recorded using Renishaw invia Raman spectrometer in the spectral range 150-2700 cm^{-1} with an excitation wavelength of 633 nm of an Ar ion laser with a power ~ 5 mW at the sample to study structural as well as optical properties. UV-VIS spectroscopy (PerkinElmer (Lambda 55) UV-VIS spectrometer) was performed to obtain absorption feature of the synthesized products in the spectral range 225-675 nm. PL emission spectra were also recorded using 320 nm excitation wavelength by PerkinElmer LS55 Fluorescence spectrometer to study the emission behavior of the materials. VSM measurements were done to study the magnetic properties of the synthesized samples at room temperature using VSM (ADE-DMS, model EV-7USA).

6.2.3. Photocatalysis

In order to study the photocatalytic properties of the synthesized samples over MB dye under UV irradiation, the aqueous solution of MB dye was prepared using the steps as shown in Fig. 6.2 for photocatalytic measurements. The photodegradation of MB dye was evaluated by irradiation of UV light of wavelength 254 nm. For photocatalytic measurements, 50 mg of rGO sheets decorated with CdS NPs, as a photocatalyst, was dispersed in 50 ml aqueous solution such that its concentration in the solution turns out to be 10^{-5} M. The obtained dispersed solution was stirred in the dark for 30 min to achieve the adsorption equilibrium. The solution is exposed to UV light of wavelength 254 nm for 70 min. After each 10 min, the solution is taken out from the UV chamber for recording the UV-VIS absorption spectra to determine the residual concentration of MB dye.

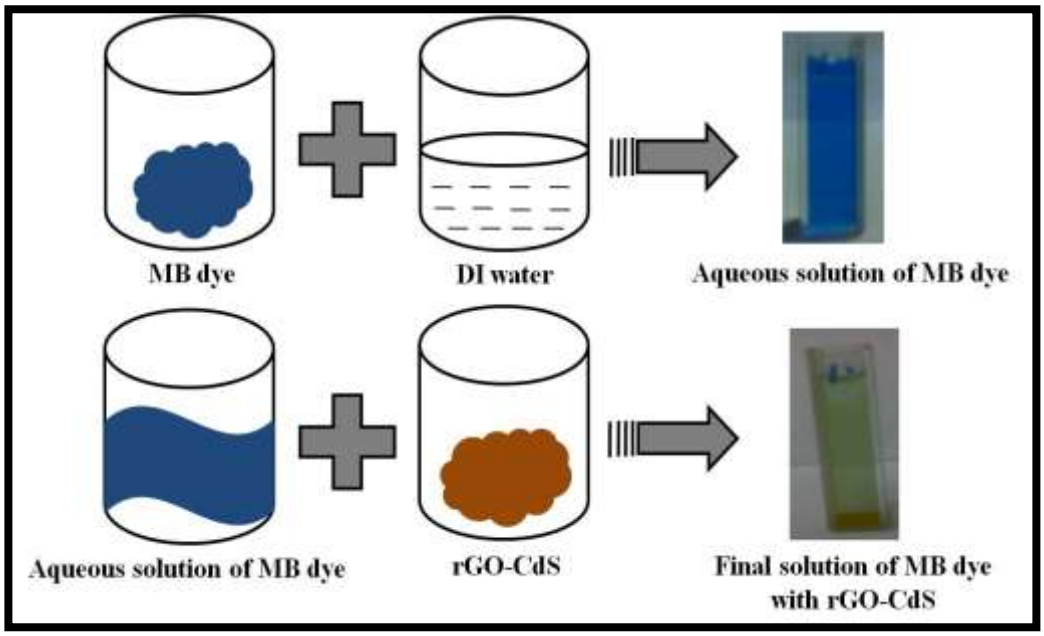


Fig. 6.2 Schematic illustration of the sample preparation for studying the photocatalytic activity.

6.3 Results and Discussion

6.3.1 XRD

The XRD patterns of graphite, GO, rGO and rGO decorated with CdS NPs are shown in Fig. 3. It can be seen from Fig. 6.3a-c that the graphite, GO and rGO have characteristic peaks at 2θ = 26.42˚ (JCPDS No. 41-1487), 9.59˚ and 25.15˚ corresponding to (002) plane with the value of d-spacing 0.336, 0.921 and 0.353 nm, respectively. The longer values of d-spacing for GO compared to graphite is attributed to the presence of oxygen containing functional group formed during the oxidation process. The presence of functional group in GO is responsible to lose stacks of layers effectively [13]. The large interlayer distance of GO was attributed to the formation of hydroxyl, epoxy, carbonyl and carboxyl groups in its

structure [14]. The XRD pattern reveals that GO sheets have been successfully exfoliated from the raw graphite and after solvothermal reduction, almost all GO sheets have been transformed into rGO with significantly less functionalities. The broad nature of (002) peak of rGO indicates that the samples are composed with few layers of rGO sheets [15]. Fig. 6.3d represents the XRD pattern of rGO decorated with CdS NPs. The peaks located at $2\theta = 26.84, 30.60, 43.85, 51.94, 54.44$ and 64.78° are distinctly indexed to the reflection from (111), (200), (220), (311), (222) and (400) crystal planes of cubic phase of CdS (JCPDS No.89-0440) NPs, respectively. No peak corresponding to any impurity phase was detected in the XRD pattern. The broadening and sharp intensity of diffraction peaks indicate that the grain size of CdS NPs may be in nanoscale with good crystallinity. The XRD pattern of rGO decorated with CdS NPs does not contain the characteristic diffraction peak of rGO. It might be due to low intensity compared to the intensity of CdS peaks or the presence of few layers in the rGO sheets [16]. It is also well known that the decorated NPs may prevent the restacking of graphitic carbon sheets. Hence, the characteristic diffraction peak of the layered structure of rGO may disappear. The grain size of CdS NPs decorated over rGO surface is calculated to be 15 ± 2 nm.

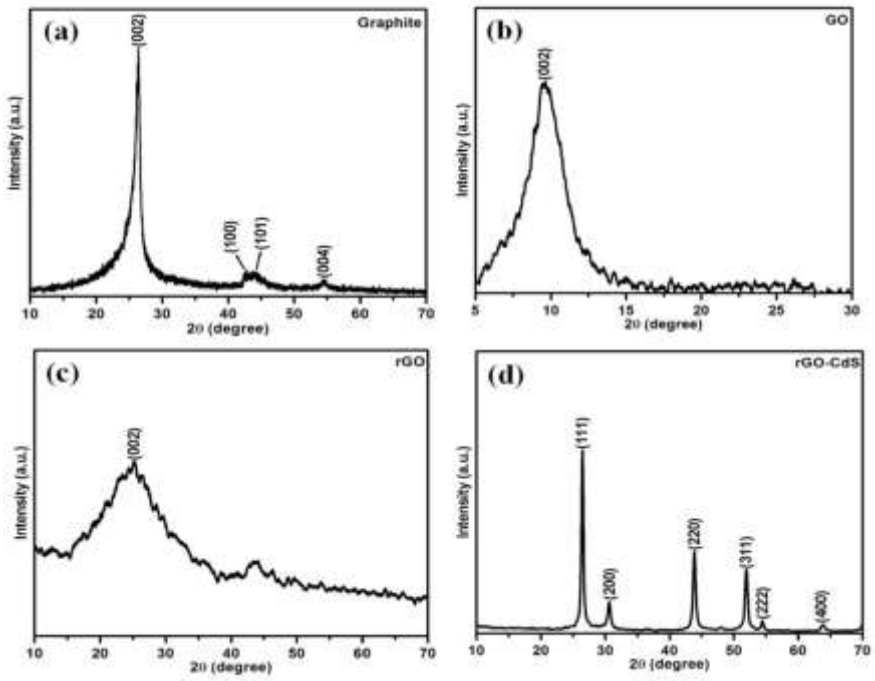


Fig. 6.3 XRD pattern for (a) graphite (b) GO (c) rGO and (d) rGO-CdS nanocomposites.

6.3.2 TEM, HR-TEM, SAED and EDX

TEM and HR-TEM measurements were carried out for as prepared rGO decorated with CdS NPs to resolve their features in nanoscale domain. The structural characterization of rGO-CdS nanocomposites have been done by HR-TEM and TEM measurements. The size of synthesized samples of CdS NPs decorated over rGO sheets was also estimated by TEM analysis. Fig. 6.4a shows the representative HR-TEM image of the rGO-CdS nanocomposites. The Fig. 6.4b-f shows the representative TEM images of the rGO-CdS nanocomposites at different resolution. Fig. 6.4a reveals that there is a good interfacial contact between rGO sheets and CdS NPs. It could be expected that such an intimate interfacial contact for rGO-CdS nanocomposites favor the photogenerated charge carrier

transfer process across the interface between CdS NPs and rGO sheets upon irradiation of UV light. It could assist to enhance the photocatalytic activity of rGO-CdS nanocomposites.

Fig. 6.4b-f clearly reveals that the distribution of CdS NPs over rGO sheets is homogeneous and monodispersed. Moreover, no free CdS NPs are detected outside the range of the rGO sheets. It is also obvious that the smooth and thin surface of rGO sheets is densely covered by CdS NPs with uniform size and shape. These results further confirm that the CdS NPs have been successfully decorated over rGO sheets. Fig. 6.4g shows the SAED pattern of as prepared rGO-CdS nanocomposites which clearly demonstrate that the ring pattern is appeared due to cubic crystal phase of CdS NPs and also nicely matched with the XRD results. Fig. 6.4h shows the histogram of particle size of CdS NPs decorated over rGO sheets. By TEM measurements, the average particle size of CdS NPs decorated over rGO sheets is calculated to be 17±5 nm. This value is in good agreement with the crystallite size of CdS NPs calculated by XRD data. Fig. 6.4i represents the results of EDX measurements. By looking at Fig. 6.4i, one can say that the synthesized samples are impurity free. The elements present in in-situ synthesized samples are C, Cd, S and O. The presence of oxygen (O) may be due to the oxygen containing functional group even after reduction of GO to rGO. It means that the GO has not been completely transformed to reduced rGO. All above discussions obviously indicate that the solvothermal method is very effective one step in-situ approach to decorate CdS NPs over rGO sheets with high density and good crystallinity.

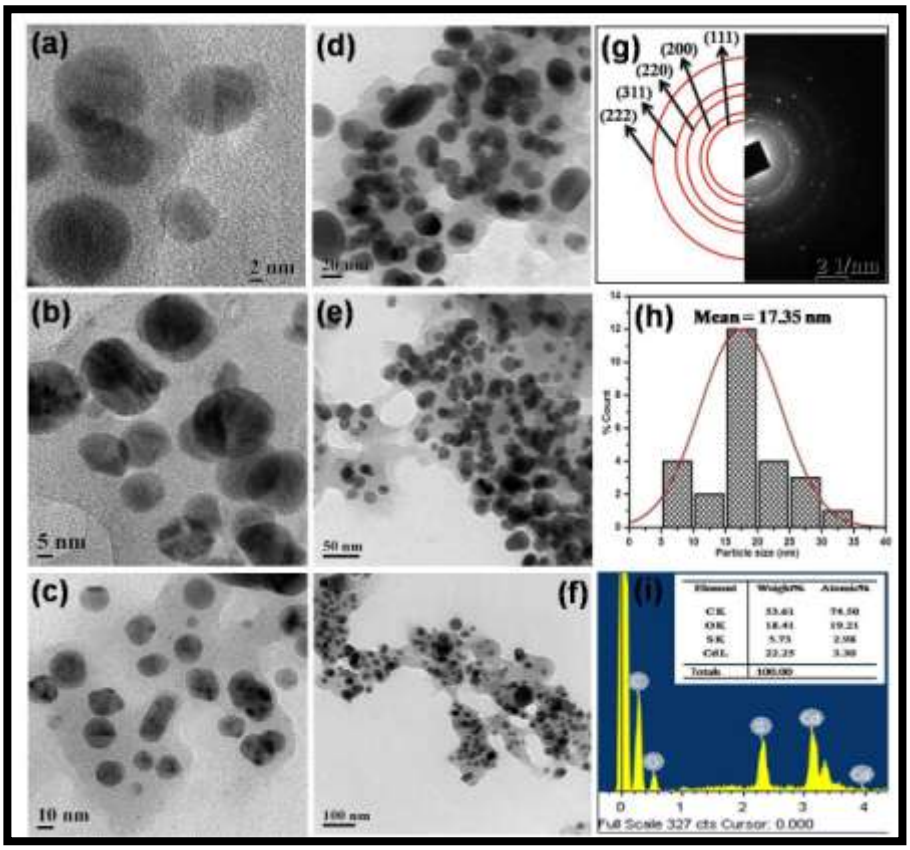


Fig. 6.4 (a) HR-TEM image of rGO-CdS nanocomposites (b-f) TEM images of rGO-CdS nanocomposites at different resolutions (g) SAED pattern of the rGO-CdS nanocomposites (h) histogram of rGO-CdS nanocomposites (i) EDX spectrum of rGO-CdS nanocomposites.

6.3.3 Raman spectroscopy

Raman spectroscopy is an effective and non-destructive experimental technique which has been mostly used to find structural information of carbon-based materials [17]. In order to get structural information of carbon-based materials from its Raman spectra, the G and D bands and their overtones are mainly used. The G band, resulting from the stretching of sp^2

carbon pairs, is the characteristic of sp^2 hybridized carbon atom network and it corresponds to the optical E_{2g} phonons at the Brillouin zone center [18]. The D band is Raman active only due to the defect present in the sample and assigned to breathing mode of k-phonon of A_{1g} symmetry [17]. The intensity ratio of D and G bands (ID/IG) could give the information of degree of disorder and average size of the sp^2 domains present in the samples [19]. Hence, it is believed that Raman spectra of carbon based materials with the G and D bands are very sensitive to defects, disorder and domain size.

Fig. 6.5 shows the Raman spectra of the GO (black), rGO (red), CdS (green) and rGO-CdS nanocomposites (blue) recorded in the spectral range 150-2700 cm^{-1}. The Raman spectra of GO, rGO and rGO-CdS nanocomposites revealed characteristics D (defect) and G (graphite) bands. The Raman spectra of GO contains D and G bands located at ~ 1320 and ~ 1566 cm^{-1}, respectively whereas in rGO, these bands are appeared at ~ 1325 and ~ 1575 cm^{-1}. In addition to D and G bands, a broad low intensity 2D band located at ~ 2657 cm^{-1} is also observed in the Raman spectra of GO. The 2D band is originated due to double resonance transition resulted due to the production of two phonons with opposite momentum [20]. It is interesting to note that the Raman spectrum of rGO has two distinct peaks in place of broad 2D band, as it has been observed in the Raman spectrum of GO. However, the intensity of these two Raman peaks of rGO turns out to be different. The splitting of 2D band into two nicely distinct Raman peaks in rGO-CdS nanocomposites indicate that the synthesized rGO is composed of two sheets [21]. Further, two well distinct Raman peaks almost at same wavenumber position of rGO decorated with CdS NPs have

been observed, as it is observed in rGO. The intensity of these two peaks is relatively high than that of rGO. The splitting of 2D band into two well resolved peaks of almost same intensity in Raman spectrum of rGO decorated with CdS NPs may be explained in terms of perturbation induced double resonance scattering process. The decoration of CdS NPs on rGO surface may develop strain on rGO sheets that ultimately causes to split 2D band into different peaks depending upon the presence of sheets in rGO-CdS nanocomposites [21]. The change in structure upon transformation of GO into rGO due to chemical reduction can be confirmed by looking at the peak shift of the Raman bands. The up shift of G band in Raman spectrum of rGO indicates the deoxygenating of GO [22], which is a general feature of reduction of GO into rGO. The increased value of ID/IG of rGO than that of GO indicates the increase of sp^2 domain due to the restoration of damaged sp^2 carbon conjugation during GO preparation and the average size of the sp^2 domains is decreased after reduction of GO into rGO [23]. Further, the ratio ID/IG is inversely proportional to the crystallite size [18]. The increased ID/IG value of rGO upon reduction of GO into rGO has been reported in earlier study [23].

Raman spectrum of rGO-CdS nanocomposites contains two characteristic Raman bands of CdS at ~ 288 and ~ 580 cm^{-1}. The observed peak position is same as it has been observed in case of pure CdS NPs. The Raman bands at ~ 288 and ~ 580 cm^{-1} correspond to the first-order (1LO) and second-order (2LO) longitudinal optical (LO) phonon modes of CdS NPs. Zeiri et al. [24] had reported that bulk CdS has two characteristic Raman bands at ~ 300 and ~ 600 cm^{-1} corresponding to the first-order (1LO) and second-order

(2LO) phonon modes. In the present study, these two bands are shifted to lower wavenumber side that could be due to presence of rGO sheets [25]. The presence of characteristic graphitic bands with characteristic bands of CdS NPs confirms the formation of rGO-CdS nanocomposites, which could not be confirmed by analyzing the XRD data. Raman spectra of rGO-CdS nanocomposites revealed that there is no any significant change in the shape of spectral line and position of G band compared to rGO. However, the peak position of D band is changed significantly. The change in position of D band may be due to the lattice distortion caused by incorporation of CdS NPs over the rGO sheets. The decrease in ID/IG value for rGO-CdS nanocomposites compared to rGO indicates that the number of layers in rGO sheets is decreased without decreasing the average size of the sp^2 domain. The lower ID/IG ratio also indicates a better defect repair mechanism for rGO-CdS nanocomposites [26].

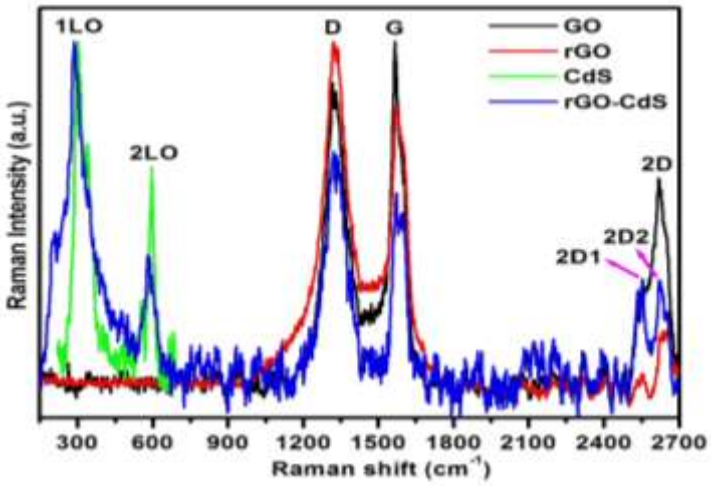


Fig. 6.5 Raman spectra of GO (black), rGO (red), CdS (green) and rGO-CdS nanocomposites (blue).

6.3.4 UV-VIS spectroscopy

UV-VIS spectroscopy is an important optical characterization technique for studying graphene and graphene based semiconductor nanocomposites. Fig. 6.6 shows the UV-VIS absorption spectra of as synthesized graphene (black), CdS (red) and rGO-CdS nanocomposites (green). The absorption spectra are recorded in the spectral range 225-675 nm. All the samples were dispersed in ethanol to record the absorption spectra. It can be seen from Fig. 6.6 that the rGO has an absorption peak at ~ 258 nm along with an additional absorption peak at ~ 228 nm. A similar type of additional peak along with characteristic feature at ~ 265 nm had also been observed for graphene in earlier study [27]. The position of characteristic peak of rGO (~ 258 nm) is slightly less compared to its reported value [27] of ~ 265 nm. The peak at ~ 258 nm is attributed to the excitation of π-plasmon of graphitic structure [27]. The blue shift of characteristic absorption peak by 8 nm in rGO compared to its standard value may be caused due to the presence of few layers in rGO sheets. It is very interesting to note that the absorption peak of CdS NPs is also found to be at ~ 258 nm. Further, in case of rGO-CdS nanocomposites, the broad absorption edge at ~ 510 nm was also observed in comparison to pure CdS NPs. The broad feature at ~ 258 nm in rGO-CdS nanocomposites may be due to strong coupling between rGO sheets and CdS NPs due to their intimate interface contact (see HR-TEM image) and homogeneous distribution of CdS NPs on graphene layer [28]. The additional peak at ~ 228 nm in case of rGO may be due to defects created by oxygen containing functional group present in the rGO. The presence of oxygen, as defects, has already been confirmed by

EDX measurements.

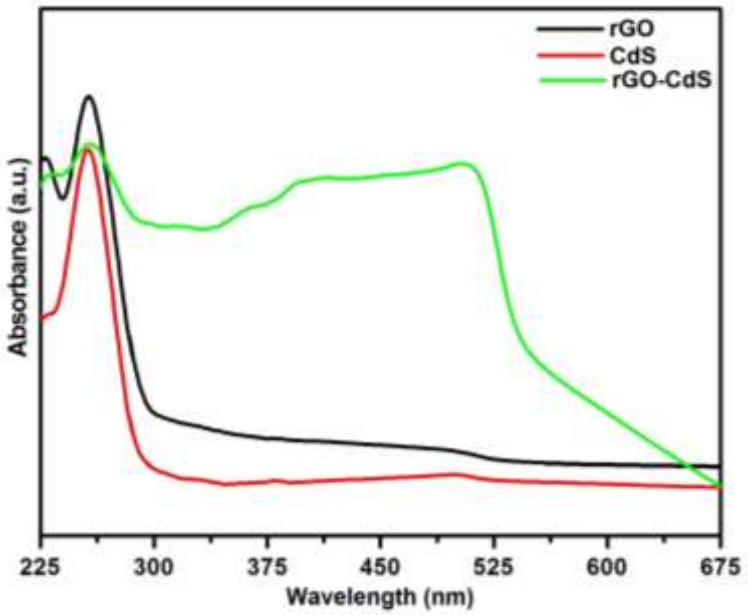


Fig. 6.6 UV-VIS spectra of rGO (black), CdS (red) and rGO-CdS nanocomposites (green).

6.3.5 PL spectroscopy

PL spectroscopy is an important tool to study the effect of graphene on recombination of photogenerated e^- - h^+ pairs produced by pure CdS NPs. Fig. 6.7 shows the PL spectra of pure CdS NPs and rGO-CdS nanocomposites dispersed in ethanol at room temperature. PL measurements were carried out using excitation wavelength of 320 nm. The emission spectra were recorded for the spectral range 350-550 nm. From Fig. 6.7, it can be seen that pure CdS NPs have two distinct emission bands at ~ 410 and ~ 430 nm along with two shoulder bands at ~ 460 and ~ 530 nm. The position and shape of the emission bands of rGO-CdS nanocomposites (see Fig. 6.7) were analogous with CdS NPs except the disappearance of emission band at ~ 530 nm. In comparison to the intensity of emission

bands of pure CdS NPs, the intensity of emission bands of rGO-CdS nanocomposites is found to be less relative to pure CdS NPs. The emission band located at ~ 410 nm was assigned to the trapping effect of photogenerated e^- and h^+ after their recombination whereas the emission band at ~ 430 nm may be due to a small fraction of weakly trapped e^-- h^+ pair excitons [29]. In another study [30], the emission band at ~ 410 nm is assigned to CdS excimer band-to-band emission. Spanhel et al. [31] had reported that the emission band at ~ 460 nm is appeared due to the recombination of excitons and/or shallowly trapped e^-- h^+ pairs that causes the band edge luminescence between 450-500 nm. The broad emission band centered at ~ 530 nm may be due to the transition of electrons from defect states, as formed by S atom of CdS NPs, to the valance band (VB) of CdS NPs [32]. The decrease in PL intensity is attributed due to the band alignment at the interface of rGO sheets and CdS NPs. The position of conduction band at – 4eV for pure CdS NPs and the Fermi level of graphene at – 4.42 eV is energetically favorable [33] and responsible for efficient transfer of excited electron from conduction band (CB) of CdS NPs to rGO sheets. As a result, the charge recombination process got delayed than that of pure CdS NPs. Thus, the decrease of intensity of emission bands for rGO-CdS nanocomposites indicates the good interfacial interaction between rGO sheets and CdS NPs [10]. These results demonstrate that the rGO-CdS nanocomposites may effectively improve their optoelectronic and photocatalytic activity compared to pure CdS NPs due to effective charge separation and efficient charge transport from CdS NPs to rGO sheets and vice-versa [33].

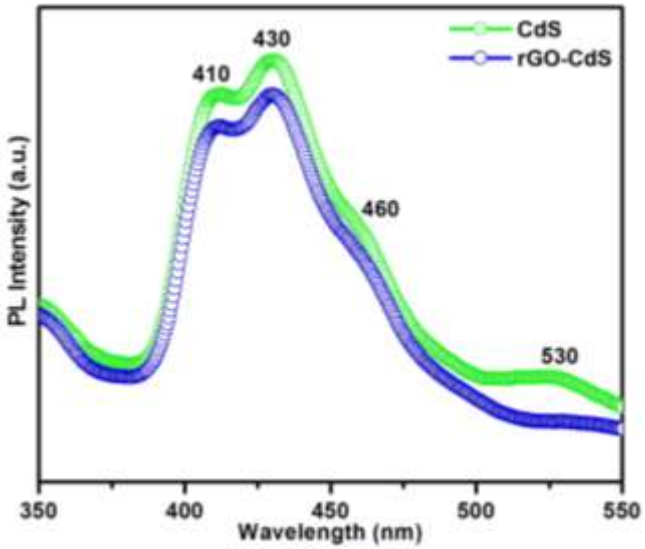


Fig. 6.7 PL spectra of pure CdS NPs (green) and rGO-CdS nanocomposites excited by 320 nm wavelength.

6.3.6 Photodegradation of MB dye

Photocatalysis is a process in which e^-- h^+ pairs are generated from semiconductor surface when materials are exposed to light. In the aqueous solution, adsorbed H_2O/OH^- functional group act as an electron donor to yield hydroxyl radicals (·OH) while adsorbed oxygen acts as an electron acceptor to form oxygen peroxide radical ($O_2^{\bullet-}$). These strongly oxidized species degrade organic compounds into small molecules. The rGO based semiconductor nanocomposites show improved photocatalytic activity. It could be due to (i) the rGO sheets have high electron mobility that makes it to act as an efficient electron acceptor and provide a better channel to transport excited electrons from semiconductor NPs to rGO sheets that obstructed recombination of the photogenerated e^-- h^+ pairs (ii) the rGO has large surface area that provides more active adsorption sites for the molecule to enlarge the

reaction space and photocatalytic reaction centres [34].

In the present work, the decoration of CdS NPs over rGO sheets have better degradation ability compared to the pure CdS NPs. The photocatalytic activity of rGO-CdS nanocomposites for photodegradation of MB dye has been carried out with the help of UV-VIS spectrometer under UV light irradiation of 254 nm excitation wavelength. Fig. 6.8a shows UV-VIS spectra of the photodegraded MB dye with rGO-CdS nanocomposites after irradiation of mixed solution by UV light for 70 min at a regular interval of 10 min. The photodegradation efficiency of rGO, pure CdS NPs and rGO-CdS nanocomposites to degrade MB dye is analyzed by calculating C/C_0 ratio with the help of UV-VIS spectra, where C is the concentration of MB dye after the irradiation of UV light for time t and C_0 is the concentration before the irradiation of UV light. The calculated value of C/C_0 for the mixed solution is plotted with irradiation time and shown in Fig. 6.8b. It can be seen from Fig. 8b that there is no any significant change in the concentration of MB dye after the irradiation of UV light in the absence of photocatalysts. However, it can be observed that the MB dye is slightly degraded in the presence of rGO sheets due to its large adsorption ability. It suggests that the degradation of MB dye is resulted due to the mixing of rGO sheets as photocatalyst under UV light irradiation. The pure CdS NPs are found to exhibit relatively low photodegradation efficiency than that of rGO and rGO-CdS nanocomposites. It could be due to (i) the rapid recombination rate of e^- - h^+ pairs (ii) CdS NPs have tendency to aggregate due to instability that reduces the surface area and consequently the photocatalytic performance is also reduced.

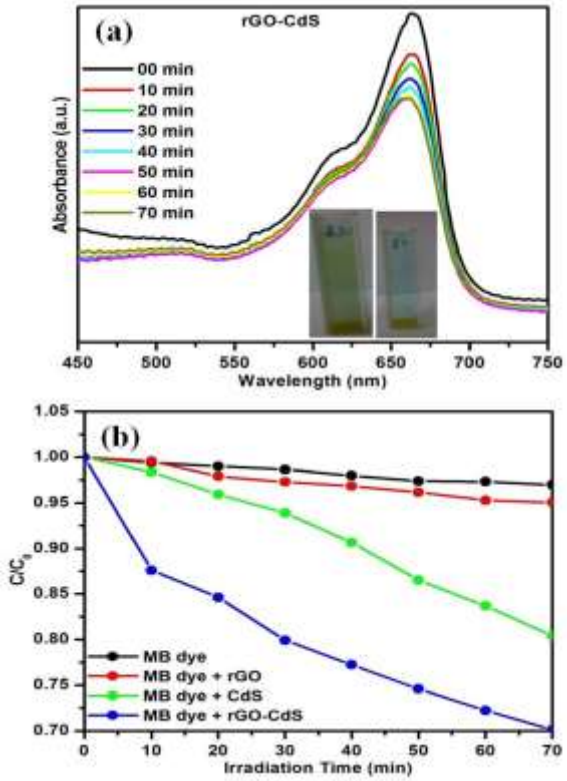


Fig. 6.8 (a) Absorption spectra of the solution of MB dye mixed with rGO-CdS nanocomposites under exposure of UV light (b) degradation of MB dye with rGO, pure CdS NPs and rGO-CdS nanocomposites as photocatalyst in terms of relative concentration (C/C_0) of MB dye vs irradiation time.

In order to overcome these problems and to improve the photocatalytic efficiency of pure CdS NPs, its decoration on rGO sheets may be a better option. It is obvious from Fig. 6.8b that the rGO-CdS nanocomposites revealed higher photodegradation of MB dye than that of pure CdS NPs and rGO sheets. The improved photodegradation activity of rGO sheets decorated with CdS NPs can be attributed to the large surface area of rGO sheets that provides a transport channel for fast transfer of excited electrons from CB of

CdS NPs to rGO sheets that further delay the recombination time of e^-- h^+ pairs. The delay in recombination time provides appropriate time to OH^- (present in the aqueous solution) to take holes from the VB of CdS NPs to form more hydroxyl radicals (·OH) and accelerate the degradation process due to high oxidation potential for the oxidation of organic dye molecules [2]. The delay in recombination process is well supported by the results of PL spectra, as shown in Fig. 6.7. From PL spectra, it is obvious that the PL intensity of emission bands and full width at half of the maximum (FWHM) of rGO-CdS nanocomposites is relatively less than that of pure CdS NPs. It indicates that the recombination of photogenerated e^-- h^+ pairs is efficiently obstructed by the growth of CdS NPs over rGO sheets.

A schematic diagram to understand the charge transfer mechanism in rGO-CdS nanocomposites under UV light irradiation is shown in Fig. 6.9a. When aqueous solution of synthesized material is illuminated by the UV light in presence of water containing dissolved oxygen and organic molecules, the degradation of organic molecules takes place. The mechanism for the enhanced photocatalytic activity of CdS NPs decorated over rGO sheets is explained in terms of delay in recombination time of e^-- h^+ pairs. After the irradiation of mixed solution by UV light, e^- of the VB are excited to CB of CdS NPs by leaving h^+ in the VB. In absence of rGO sheets, electrons of CB come down quickly to VB due to its short life time and instability of excited states that results less efficiency for photocatalytic activity of pure CdS NPs. Once rGO sheet is introduced to CdS NPs, it plays the role of electron acceptor and transporter to obstruct the recombination of

photogenerated e^-- h^+ pairs efficiently. As a consequence, more free charge carriers are available to form reactive species in the solution. The electrons of CB of CdS NPs can easily be transferred to carbon atoms of rGO sheets due to an intimate interfacial contact between rGO sheets and CdS NPs. An et al [33] has reported that the positions of CB and VB of CdS NPs are lying at – 4 eV and – 6.5 eV (used vacuum level as a reference), respectively whereas the work function of rGO is found reported to – 4.42 eV, which is just below to the position of CB of CdS NPs. Thus, when there is an intimate interfacial contact between rGO sheets and CdS NPs, the electrons of CB of CdS can easily be transferred to rGO and delay the recombination time of e^-- h^+ pairs. Meanwhile, the π-π stacking interaction between rGO sheets and MB dye plays an important role in the adsorption of MB dye on the surface of rGO sheets [35]. In addition, MB dye molecules are also adsorbed on the surface of the CdS NPs. These adsorbed MB dye molecules on the surface of CdS NPs convert to MB* (excited state) [36]. After excitation by UV irradiation, MB* dye molecules directly inject electrons to the CB of CdS NPs and thereafter, the electrons move toward the rGO sheet (see Fig. 6.9b) due to higher work function of rGO than CdS NPs. These transferred electrons will react with dissolved O_2 molecules. As a result, the amount of oxygen peroxide radical $O_2^{\bullet -}$ is increased. On the other hand, h^+ of VB of CdS NPs are taken by OH^- derived from aqueous solution and formed ·OH radicals that has high oxidation potential for the oxidation of organic dye molecule. These radical ions degrade the MB dye to small molecules such as; CO_2 and H_2O.

The detailed mechanism for the degradation of MB dye can be understood by the following steps:

$$CdS + h\nu\ (E > Eg) \rightarrow CdS\ [h^+\ (VB) + e^-\ (CB)]$$

$$O_2 + e^-\ (CB) \rightarrow O_2^{\bullet -}$$

$$H_2O + h^+ \rightarrow H^+ + OH^-$$

$$OH^- + h^+\ (VB) \rightarrow \cdot OH$$

$$MB + \cdot OH + O_2^{\bullet -} \rightarrow CO_2 + H_2O + \ldots\ etc.$$

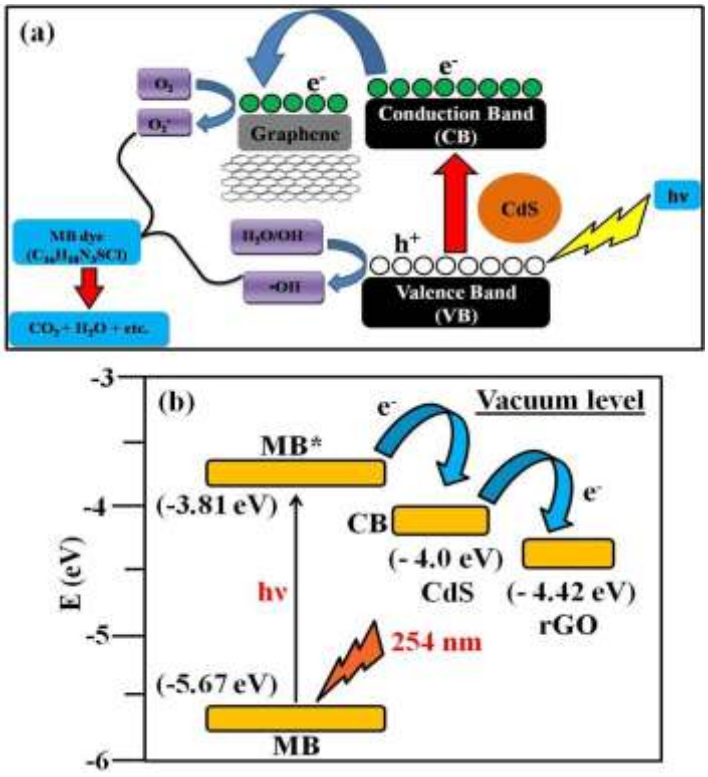


Fig. 6.9 (a) Schematic presentation of photodegradation of MB dye with rGO-CdS nanocomposites (b) energy diagram showing transfer of electron from MB dye to CdS NPs and rGO sheets.

6.3.7 Magnetic properties

In order to study the magnetic properties of pure CdS NPs and CdS NPs decorated over rGO sheets, VSM measurements have been done at room temperature under the applied magnetic field in the range of -15000Oe to +15000Oe. The diamagnetic signal of the sample holder was subtracted from the measured magnetic signal of the samples. The variation of magnetization vs. applied field for pure CdS NPs and rGO sheets decorated with CdS NPs are shown in Fig. 6.10a and 6.10b, respectively. The presence of hysteresis loop suggests that the synthesized CdS NPs and rGO-CdS nanocomposites are weak ferromagnetism. The presence of a nonzero coercivity also demonstrates the room temperature ferromagnetism (RTFM) behavior of the synthesized samples [37]. The value of coercivity (Hc) and saturation magnetization (Ms) for pure CdS NPs was found to be 233 Oe and 0.03 emu/g, respectively. However, in case of rGO-CdS nanocomposites, the value of Hc and Ms was found to be 259 Oe and 0.01 emu/g, respectively. Thus, the value of Hc for pure CdS NPs is found to be slightly less than that of its value of rGO-CdS nanocomposites while the Ms value is slightly more than that of rGO-CdS nanocomposites. The increased value of Hc for rGO-CdS nanocomposites demonstrates that graphene based chalcogenide materials may be a prospective candidate for the high density information storage application [37]. The decreased Ms value for rGO-CdS nanocomposites compared to pure CdS NPs may be due to the presence of spin disorder on the rGO surface and surface oxidation [37]. The insets of Fig. 6.10a and 6.10b reveal an enlarged hysteresis loop for a smaller field range -500Oe to +500Oe. The presence of

ferromagnetism in pure CdS NPs is generally considered due to presence of crystal defects confined to the surface of NPs [38] that often grown on the boundary and surface of the synthesized NPs. Yang et al. [38] has suggested that the value of Ms strongly depends on the crystalline size of the sample and the concentration of sulfur vacancies. They reported that the value of Ms is decreased from 0.0187 to 0.0012 emu/g by increasing the crystallite size of CdS NPs from 4.0 to 5.5 nm. Further, it is also reported [39] that the sulfur vacancies play a vital role in developing RTFM in pure CdS NPs. Wang et al. [40] has reported that the RTFM in rGO may be attributed to itinerant electron magnetism rather than super exchange magnetic coupling interaction between spins like molecule-based magnets. A number of studies [40-41] had been done on magnetic behavior of rGO and in these studies it has been reported that the ferromagnetic behavior of rGO could be due to presence of various defects on rGO surface. Radovic et al. [42] has reported that the removal of functional group would introduce various defects such as; vacancies and topological defects on rGO surface with unpaired electrons, as spin units. The stability of unpaired electrons, as spin units, in these structures is mainly due to the large π-conjugation between the carbon atoms [40]. The origin of RTFM in rGO may be due to the nucleation of magnetic moment in the defective sp^2 carbon samples. The GO has many functional group such as; C – O – C, C – OH, – COOH and C = O. The reduction of GO with hydrazine would remove some of the group and restore some of the damaged sp^2 carbon conjugation during sample preparation. The long range ordered magnetic spin units present on the rGO surface are confined via intramolecular interaction/lattice interaction

between the rGO sheets, which results RTFM in rGO [38]. The decrease in Ms value for rGO-CdS nanocomposites compared to pure CdS NPs may be due to the intra-molecular interaction between the magnetic domains of CdS NPs and magnetic domains of spin units present on rGO sheets. The presence of intra-molecular interaction between the magnetic domains in case of CdS NPs decorated over rGO sheets causes to align the magnetic moments in same direction. As a result, the Ms value of CdS NPs decorated over rGO sheets turns out to be less than that of pure CdS NPs. A schematic presentation for the alignment of the magnetic domains of pure CdS NPs and rGO-CdS nanocomposites has been given in Fig. 6.11. As discussed above, pure CdS NPs and rGO sheets have RTFM due to presence of defects in their structures. Therefore, it is also expected that composites of both material should show RTFM. The defects in the synthesized sample of rGO and rGO decorated with CdS NPs can be verified by Raman spectra (Fig. 6.5) that contains a prominent D peak, which becomes active due to the presence of defects in the structures. Hence, graphene based CdS nanocomposites may be a proficient alternative for many important applications in spintronics, magneto-resistance and high memory storage devices etc [40].

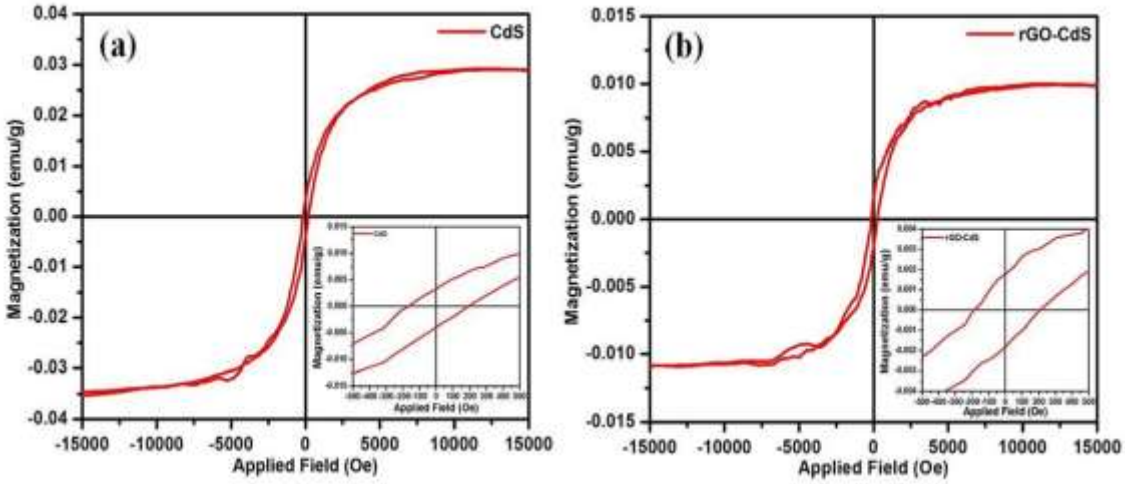


Fig. 6.10 (a) Room temperature M-H curve of pure CdS NPs (b) Room-temperature M-H curve of rGO-CdS nanocomposites. The inset in each figure shows M-H curves with applied field of -500 Oe < H < +500 Oe.

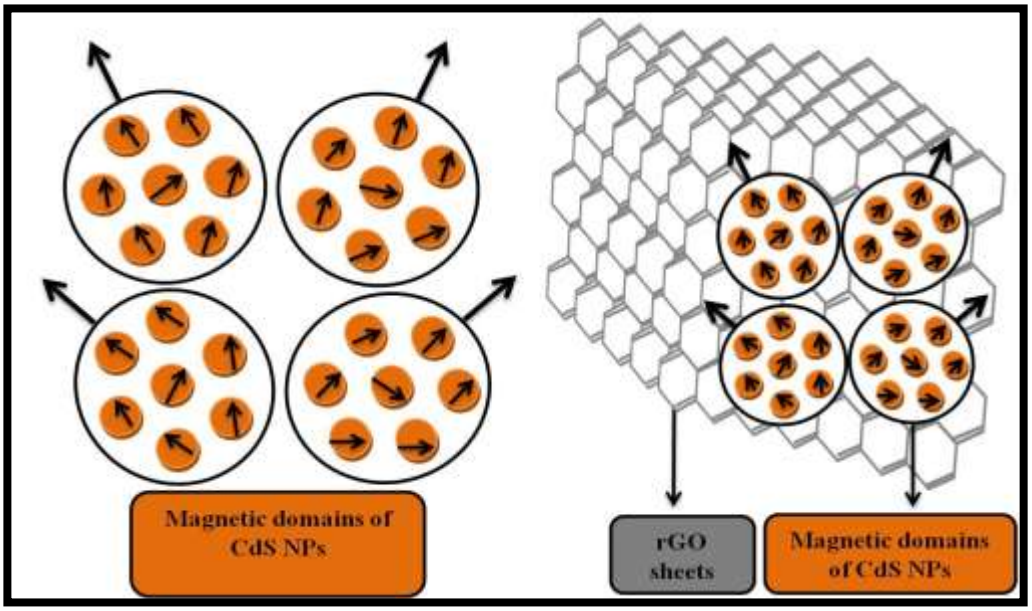


Fig. 6.11 Mechanism of RTFM in pure CdS NPs and rGO-CdS nanocomposites.

6.4 Conclusion

CdS NPs, rGO and rGO decorated with ferromagnetic CdS NPs have been synthesized using a facile in-situ solvothermal method. The in-situ solvothermal method is very effective to decorate well dispersed and stable CdS NPs. It has been observed that the GO serves as an excellent precursor for the in-situ growth of rGO-CdS nanocomposites. The decrease in the intensity of emission bands of rGO-CdS nanocomposites suggests the efficient transfer of electrons from CdS NPs to rGO sheets that restricts the recombination of e^-- h^+ pairs compared to pure CdS NPs. This effect can improve the photocatalytic activity of pure CdS NPs for photodegradation of MB dye. The as prepared rGO-CdS nanocomposites have good stability and better performances for the photodegradation of MB dye under UV light irradiation. The increase in the photodegradation efficiency can be attributed to the presence of rGO sheets that effectively delays the recombination of e^-- h^+ pairs and successfully stabilize CdS NPs. The magnetic study reveals that the coercivity of rGO-CdS nanocomposites is increased than that of pure CdS NPs. It suggests that the incorporation of rGO to CdS NPs has made it a suitable candidate for application in high memory storage device.

References

[1] A. K. Geim, K. S. Novoselov, Nat. Mater., 2007, **6**, 183.

[2] S. Kaveri, L. Thirugnanam, M. Dutta, J. Ramasamy, N. Fukata, Ceramics, International, 2013, **39**, 9207.

[3] K. S. Novoselov, A. K. Geim, S. V. Morozov, D. Jiang, Y. Zhang, S. V. Dubonos, I. V.

Grigorieva, A. A. Firsov, Science, 2004, **306**, 666.

[4] S. Park, R. S. ruoff, Nanotechnology, 2009, **4**, 217.

[5] S. Pan, X. Liu, New J. Chem., 2012, **36**, 1781.

[6] Z. Gao, N. Liu, D. Wu, W. Tao, F. Xu, K. Jiang, Appl. Surf. Sci., 2012, **258**, 2473.

[7] X. Li, C. Hu, X. Wang, Y. Xi, Appl. Surf. Sci., 2012, **258**, 4370.

[8] X. Wang, H. Tian, Y. Yang, H. Wang, S. Wang, W. Zhengand, Y. Liu, J. Alloys Compd., 2012, **524**, 5.

[9] C. Xu, X. Wang, J. W. Zhu, J. Phys. Chem. C, 2008, **112**, 19841.

[10] C. Nethravathi, T. Nisha, N. Ravishankar, C. Shivakumara, M. Rajamathi, Carbon, 2009, **47**, 2054.

[11] N. Li, G. Liu, C. Zhen, F. Li, L. Zhang, H. M. Cheng, Adv. Funct. Mater., 2011, **21**, 1717.

[12] D. C. Marcano, D. V. Kosynkin, J. M. Berlin, A. Sinitskii, Z. Sun, A. Slesarev, L. B. Alemany, W. Lu, J. M. Tour, ACS Nano, 2010, **4**, 4806.

[13] D. Pan, S. Wang, B. Zhao, M. Wu, H. Zhang, Y. Wang, Z. Jiao, Chem., Mater., 2009, **21**, 3136.

[14] J. Che, L. Shen, Y. Xiao, J. Mater. Chem., 2010, **20**, 1722.

[15] C. Nethravathi, M. Rajamathi, Carbon, 2008, **46**, 1994.

[16] Y. Zhang, N. Zhang, Z. -R. Tang, Y.-J. Xu, ACS Nano, 2012, **6**, 9777.

[17] A. C. Ferrari, J. Robertson, Phys. Rev. B, 2000, **61**, 14095.

[18] F. Tuinstra, J. L. Koenig, J. Chem. Phys., 1970, **53**, 1126.

[19] D. Jhang, X. Jhang, Y. Chen, C. Wang, Y. Ma, Electrochimica Acta, 2012, **69**, 364.

[20] D. C. Elias, R. R. Nair, T. M. G. Mohiuddin, S. V. Morozov, P. Blake, M. P. Halsall, A. C. Ferrari, D. W. Boukhvalov, M. I. Katsnelson, A. K. Geim, K. S. Novoselov, Science, 2009, **323**, 610.

[21] O. Frank, M. Mohr, J. Maultzsch, C. Thomsen, I. Riaz, R. Jalil, K. S. Novoselov, G. Tsoukleri, J. Parthenios, K. Papagelis, L. Kavan, C. Galiotis, ACS nano, 2011, **5**, 2231.

[22] H. Hu, X. Wang, F. Liu, J. Wang, C. Xu, Synth. Met., 2011, **161**, 404.

[23] S. Stankovich, D. A. Dikin, R. D. Piner, K. A. Kohlhaas, A. Kleinhammes, Y. Jia, Y. Wu, S. T. Nguyen, R. S. Ruoff, Carbon, 2007, **45**, 1558.

[24] L. Zeiri, I. Patla, S. Acharya, Y. Golan, S. Efrima, J. Phys. Chem. C, 2007, **111**, 11843.

[25] M. Pal, N. R. Mathews, P. Santiago, X. Mathew, J. Nanopart. Res., 2012, **14**, 916.

[26] S. D. Perera, R. G. Mariano, K. Vu, N. Nour, O. Seitz, Y. Chabal, K. J. Balkus Jr, ACS Catal., 2012, **2**, 949.

[27] X. Shen, J. Wu, S. Bai, H. Zhou, J. Alloys Compd., 2010, **506**, 136.

[28] J. Wu, S. Bai, X. Shen, L. Jiang, Appl. Surf. Sci., 2010, **257**, 747.

[29] W. Wang, I. Germanenko, M. S. El-Shall, Chem. Matter, 2002, **14**, 3028.

[30] L. Spanhel, M. Haase, H. Weller, A. Henglein, J. Am. Chem. Soc., 1987, **109**, 5649.

[31] L. Spanhel, M. A. Anderson, J. Am. Chem. Soc., 1990, **112**, 2278.

[32] R. M. Nirmal, K. Pandian, K. Sivakumar, Appl. Surf. Sci., 2011, **257**, 2745.

[33] X. An, X. Yu, J. C. Yu, G. Zhang, J. Mater. Chem. A, 2013, **1**, 5158.

[34] J. C. Yu, J. Yu, W. Ho, Z. Jiang, L. Zhang, Chem. Mater., 2002, **14**, 3808.

[35] Y. Luo, S. Fan, N. Hao, S. Zhong, W. Liu, CrystEngComm, 2015, **17**, 503.

[36] H. Seema, K. C. Kemp, V. Chandra, K. S. Kim, Nanotechnology, 2012, **23**, 355705.

[37] B. Li, H. Cao, J. Yin, Y. A. Wu, J. H. Warner, J. Mater. Chem., 2012, **22**, 1876.

[38] Z. Yang, D. Gao, Z. Zhu, J. Zhang, Z. Shi, Z. Zhang, D. Xue, Nanoscale Research Letters, 2013, **8**, 17.

[39] D. Gao, G. Yang, J. Zhang, Z. Zhu, M. Si, D. Xue, Appl. Phys. Lett., 2011, **99**, 052502.

[40] Y. Wang, Y. Huang, Y. Song, X. Zhang, Y. Ma, J. Liang, Y. Chen, Nano Lett., 2009, **9 (1)**, 220.

[41] M. A. H. Vozmediano, M. P. Lopez-Sancho, T. Stauber, F. Guinea, Phys. Rev. B, 2005, **72**, 155121 and references cited therein.

[42] L. R. Radovic, B. Bockrath, J. Am. Chem. Soc., 2005, **127**, 5917.

CHAPTER - 7

One pot in-situ synthesis of reduced graphene oxide decorated with highly dispersed ferromagnetic cadmium oxide nanoparticles for enhanced photocatalytic degradation of methylene blue dye under ultraviolet irradiation

In this chapter, one pot in-situ synthesis of cadmium oxide (CdO) nanoparticles (NPs), reduced graphene oxide (rGO), and rGO-CdO nanocomposites using hydrothermal method has been reported. The photocatalytic activity of the synthesized products is investigated for the photodegradation of methylene blue (MB) dye under ultraviolet irradiation. The structural and optical properties of pure CdO, rGO, and rGO-CdO nanocomposites were investigated by X-ray diffraction (XRD), energy dispersive X-ray (EDX) spectrometer, high resolution transmission electron microscopy (HR-TEM), Raman spectroscopy (RS), ultraviolet-visible (UV-VIS) spectroscopy and photoluminescence (PL) spectroscopy measurements. The room temperature photocatalytic measurements showed that 80% of MB dye is degraded by adding the rGO-CdO nanocomposites as a catalyst to the dye solution. The room temperature ferromagnetism (RTFM) of CdO NPs is increased by decorating them over rGO sheets, which may be attributed to the short range magnetic interaction between magnetic moments of CdO NPs and spin units present on the rGO sheets.

7.1 Introduction

Graphene is a two dimensional (2D) single layer of carbon atoms [1]. It has been established as a novel material due to its extraordinary large surface area (2,630 m^2/g) [2], high electron mobility (200,000 cm^2/Vs) [3], high thermal conductivity (~5,000 W/mK) [4], excellent mechanical stability (Young's modulus ~1,100 GPa and fracture strength 125GPa) [5] and interesting transport phenomena such as; the quantum Hall effect [6]. These exceptional features of graphene have made it a promising candidate to be used in various fields of technology such as; energy storage [2], liquid crystal devices [7], transparent electrodes [8] and electromechanical resonators [9]. The Vander Waals and π-π stacking interactions lead to a restacking tendency among individual graphene sheet during reduction. It is easy to obtain few layers graphene rather than single layer graphene. The restacked structure would lead to a great loss of effective surface area of graphene, which limits the wide applications of graphene for advancement of future technology [10]. The aggregation problem can be minimized by decreasing π-π stacking interaction through incorporation of nanoparticles on graphene sheets [11].

Cadmium oxide (CdO) is an n-type metal oxide semiconductor with a direct band gap of 2.3 eV and an indirect band gap of 1.36 eV [12]. Recently, CdO nanoparticles (NPs) have attracted considerable attention from the scientific community due its potential applications in solar cells, flat-panel display and developing new sensing devices [12]. It can also be used as an alternative for electrode material [13]. Graphene based low dimensional metal oxide nanocomposites have been emerged as a rising star on the horizon

of materials science. It has attracted a lot of attention to the world wide scientists due to its ability to combine the properties of graphene and metal oxide NPs. In addition to the technological application, the graphene based metal oxide nanocomposites have been now considered as a promising material due to its unique properties and great potential for application in many areas of science and technology, particularly to solve the problems of energy crisis and environmental issues [11,14].

Aromatic pollutants are widely present in the effluent from the pesticide, photochemical and other industries and due to its high solubility in water, it can easily be transported to environment and may cause serious problem to our health. Recently, a great effort has been made to decompose organic pollutants in waste water by advanced oxidation process such as; photocatalytic, electrocatalytic, and Fenton oxidation method [15]. The removal of dyes from polluted streams is essential to avoid any hazardous and harmful effects towards environment and human health. The graphene has been evolved as a promising candidate for constructing high performance photocatalysts due to its unique structure, electronic and physicochemical properties. Different types of metal oxide semiconductor such as; tin oxide (SnO_2) [16], titanium oxide (TiO_2) [17] and its nanocomposites with reduced graphene oxide (rGO) [18] have been widely used to degrade different types of organic molecules. For enhanced photocatalytic activity, generally, narrow optical band gap (2.0 - 4.0 eV) semiconductors are used. However, in best of our knowledge, the synthesis of rGO-CdO nanocomposites has not been reported yet. The investigation on different properties of rGO-CdO nanocomposites should be

encouraged to enlighten hidden potential of material by combining both, graphene and CdO NPs for the advancement of future technology, particularly in the area of photocatalysis.

I have selected CdO to make rGO-CdO nanocomposites due to its small band gap compared to other metal oxides such as; TiO_2 (3.0 eV) [19], zinc oxide (ZnO) (3.4 eV) [20], and SnO_2 (3.6 eV) [16].The small band gap energy of CdO has made it to overcome the need of irradiation of any kind (ultraviolet or visible) radiation for the degradation of dye in aqueous solution through photocatalysis. In photocatalysis, the electron of valence band (VB) is excited to the conduction band (CB) by absorbing the photons incident on it and the excited electron is responsible for the dissociation of water molecules to form free hydroxyl radicals (OH^-), which is further responsible for the mineralization of organic pollutants [21]. But, the rapid recombination of electron (e^-) - hole (h^+) pairs limits the charge separation and causes to decrease the photodegradation efficiency of the metal oxide NPs [22]. In order to get best photocatalytic performance of CdO NPs, rGO may be tried to use as a support material. The rGO has superior characteristics such as; high conductivity and high specific surface area, which are crucial parameters for separating the charges of excited state semiconductors. It causes to decrease the recombination rate of e^--h^+ pairs [22]. The excited electrons of semiconducting materials can be stabilized in the network of carbon atoms and further by reacting with the dissolved oxygen, it generates oxidative radicals for photodegradation [22]. Therefore, a variety [18]of graphene based metal oxide nanocomposites, as photocatalysts, has been developed for the degradation of

organic and inorganic pollutants.

In view of the above studies on synthesis of graphene based metal oxide nanocomposites and its application in different fields of science and technology, particular to the field of photocatalysis, I have synthesized rGO-CdO nanocomposites to show photo sensitizer role of rGO sheets on CdO NPs. In order to ensure the strong interfacial contact between rGO sheets and CdO NPs for fascinating the transfer of electrons between rGO sheets and NPs upon light irradiation, the CdO NPs are in-situ grown over the rGO sheets via a simple and low cost hydrothermal method. In the present study, it has been found that the introduction of rGO sheets enhances the photocatalytic activity of CdO NPs significantly. Compared to the pure CdO NPs, the rGO-CdO nanocomposites showed enhanced photocatalytic efficiency and photostability of CdO NPs for the degradation of methylene blue (MB) dye under ultraviolet (UV) irradiation. Therefore, it is believed that pure CdO NPs and its nanocomposites with rGO have a great potential to solve environmental problems such as; water treatment and degradation of long organic molecules. The structural, morphological and elemental analysis of the synthesized nanocomposites was studied by XRD, HR-TEM and EDX analysis. The optical properties of the synthesized products were investigated by UV-VIS, PL and Raman spectroscopy techniques. The magnetic properties of pure CdO NPs and rGO-CdO nanocomposites were also investigated at room temperature by VSM measurements.

7.2 Experimental Techniques

7.2.1 Synthesis

In the present work, one step facile in-situ hydrothermal method has been used to prepare GO-CdO nanocomposites using GO as precursor for rGO, and cadmium acetate, as precursor for CdO. N_2H_4 was used to convert GO into rGO with formation of CdO NPs simultaneously on rGO sheets. Graphical illustration of synthesis of CdO NPs over rGO sheets is shown in Fig. 7.1.The hydrothermal is an effective and in-situ approach for the fabrication of rGO based semiconductor nanocomposites with unique advantage over other existing synthesis methods. In this method, the mixed solution of functionalized GO and metal salts as precursors for rGO and metal compound, respectively, are loaded with reducing agent in an autoclave for thermal treatment. During thermal treatment, rGO based semiconductor nanocomposites are produced simultaneously by converting GO into rGO. The presence of oxygen containing functional groups like epoxy, carbonyl, carboxyl and hydroxyl on GO are responsible for anchoring uniform and monodispersed attachment of CdO NPs on rGO sheets without agglomeration [23].

7.2.1.1 Synthesis of GO

GO was synthesized using an improved method [24] with some modifications. In general, a mixture of concentrated H_2SO_4 (360 ml) and H_3PO_4 (40 ml) was prepared in a conical flask. The graphite powder (3gm) was mixed slowly into the mixed solution of concentrated H_2SO_4 and H_3PO_4 while stirring. The homogeneous solution was made by vigorous stirring for 15 minutes. Thereafter, the conical flask containing homogeneous

solution of concentrated H_2SO_4/H_3PO_4 and graphite was kept in a water bath and 18gm of $KMnO_4$ was added very slowly under vigorous stirring at 35˚C. After mixing of $KMnO_4$, the water bath was removed and the resultant solution was then heated to 55˚C and stirred it for 12 h to complete the oxidation process of graphite. During oxidation reaction, the color of the mixed solution turns out to be dark purplish-green to dark brown. The reaction was cooled to room temperature after vigorous stirring for 12 h and poured ice (~ 400 ml) into the solution, which again produces exotherm by showing purple color of the mixed solution. To stop the oxidation process, 30% H_2O_2 solution was added gradually till the color of the mixed solution turned to bright yellow. It indicates a high oxidation level of graphite. The obtained slurry was centrifuged at 4000 rpm for 1 h, and the supernatant was removed. The precipitate was then washed with 200 ml of water, 200 ml of 30% HCl, and 200 ml of ethanol in succession until pH of the solution turns out to be 5. The remaining solid materials were then dried overnight at 40˚C. The obtained brown solid powder of GO was collected and stored for further use.

7.2.1.2 Synthesis of rGO

rGO was synthesized by a facile one step in-situ hydrothermal method. In a typical experiment, as synthesized brown solid powder of GO (0.02 mg) was first dispersed into 40ml double distilled water under mild stirring. The dispersed GO was then exfoliated by using ultrasonication for 1 h. 10µl N_2H_4 was added drop wise into the above mentioned solution under ultrasonication. Thereafter, the solution was transferred to a 50 ml of Teflon lined autoclave and heated at 160°C for 12 h. The autoclave was then cooled to room

temperature. Now, the obtained precipitate was washed with double distilled water and ethanol until the pH of solution turns out to be 5. The remaining solid materials was dried at 60˚C and the resulting black powder of rGO was collected for further use.

7.2.1.3 Synthesis of CdO NPs

CdO NPs were also synthesized by one step in-situ hydrothermal method. For synthesizing CdO NPs, 0.533gm (0.05M) of $Cd(CH_3COO)_2.2H_2O$ was mixed in 40 ml of deionized water and stirred the resultant solution to make it homogeneous. Further, 10µl N_2H_4 was added slowly to the resultant solution under vigorous stirring. The resultant solution was then kept for further stirring for 1h. Thereafter, the solution was transferred to a 50 ml of Teflon lined autoclave and heated at 160°C for 12 h. The autoclave was then cooled to room temperature. Now, the obtained precipitate was washed with double distilled water and ethanol until the pH of solution turns out to be 5. The remaining solid material was dried at 60˚C followed by calcinations at 400ºC for 2h. The resulting brown powder of CdO NPs was collected for further use.

7.2.1.4 Synthesis of rGO decorated with CdO NPs

In order to synthesize rGO decorated with well dispersed and stable CdO NPs (rGO-CdO nanocomposites), in-situ hydrothermal method is used. In a typical synthesis of rGO-CdO nanocomposites, 0.02gm of GO was first dispersed in 40 ml of deionized water and stirred it to make homogeneous solution. The dispersed GO was then exfoliated by using ultrasonication for 1 h, and then 10µl N_2H_4 was added drop wise into the solution under ultrasonication. Thereafter, 0.533g (0.05M) of $Cd(CH_3COO)_2.2H_2O$ was added slowly into

the prepared solution under vigorous stirring. The resultant solution was then kept for further stirring until the solution was mixed uniformly. Thereafter, the solution was transferred to a 50 ml of Teflon lined autoclave and heated at 160°C for 12 h. The autoclave was then cooled to room temperature. Now, the obtained precipitate was washed with double distilled water and ethanol until the pH of solution is reached to 5. The remaining solid material was dried at 60˚C followed by calcinations at 400ºC for 2h. The dried blackish brown powder was then characterized using different experimental techniques.

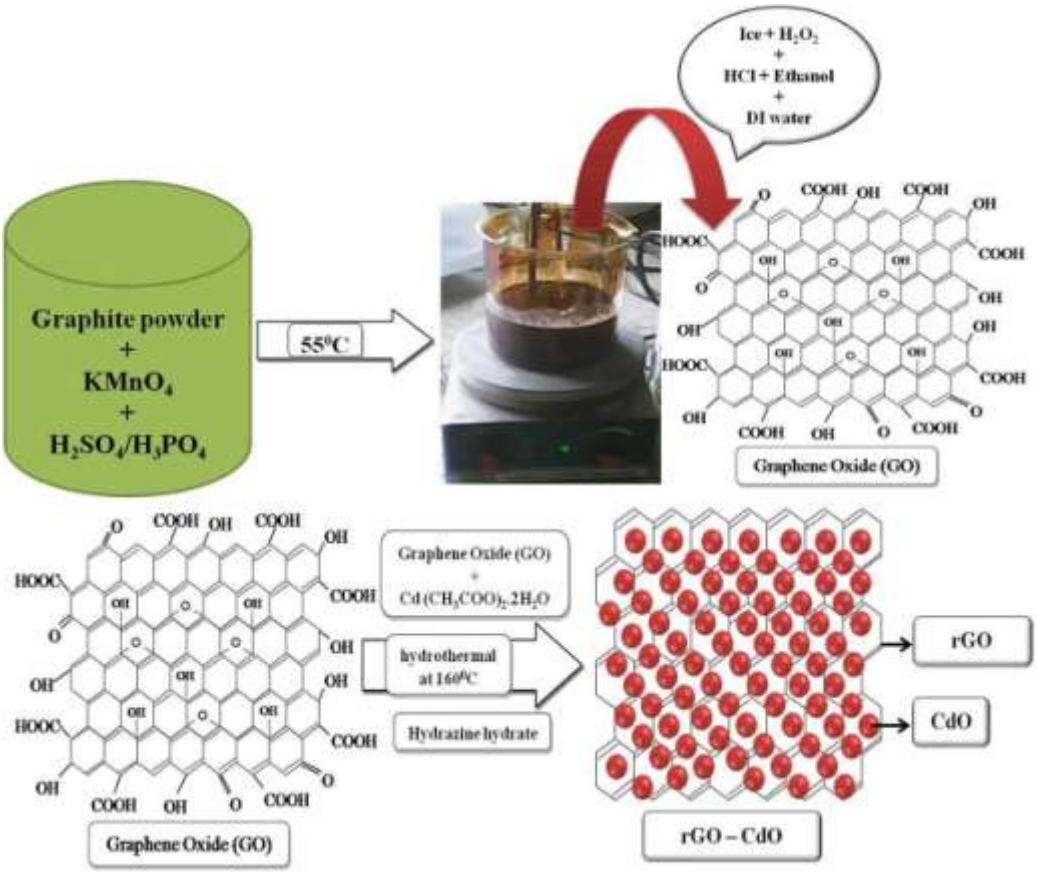


Fig. 7.1 Graphical illustration of the synthesis of rGO-CdO nanocomposites.

7.2.2 Characterization

The structural features of pure CdO NPs and rGO-CdO nanocomposites have been investigated by XRD using Rigaku Smart Lab X-ray diffractometer (CuKα radiation). The shape and size of CdO NPs decorated over rGO sheets were investigated by HR-TEM measurements using Tecnai G20 S-Twin. The elemental analysis is done using a Leo1530 VP field emission electron microscope. The optical absorption and emission properties of pure CdO NPs and rGO-CdO nanocomposites were investigated using UV-VIS (PerkinElmerLambda35 UV-VIS spectrometer) and PL spectroscopy (PerkinElmerLS55 Fluorescence spectrometer), respectively. The absorbance spectra were recorded in the spectral range 200-800 nm whereas the emission spectra were recorded in the spectral range350-550 nm. The Raman spectra of the synthesized products were recorded in the spectral range 150-2700 cm^{-1} to explore structural as well as optical properties of prepared products using Renishaw invia Raman spectrometer. VSM measurements were done to explore magnetic properties of the as prepared samplesusing VSM (ADE-DMS, model EV-7USA). Besides this, photocatalytic activity of pure CdO NPs, rGO and rGO-CdO nanocomposites was also investigated for the degradation of MB dye under UV light irradiation.

7.2.3 Photocatalytic activity

The photodegradation of MB dye was evaluated under UV light irradiation of wavelength 254 nm using UV-VIS absorption measurements. For photocatalytic activity measurements, 50 mg of rGO-CdO nanocomposites, as a photocatalyst, was dispersed in

50 ml of 10^{-5} M aqueous solution of MB dye. The obtained dispersion was stirred in the dark for 30 min to achieve adsorption equilibrium with dye molecules. Thereafter, the final solution was irradiated with UV light of wavelength 254 nm with mercury lamp for photodegradation. The UV-VIS absorption spectra of the exposed solution were recorded at regular interval of time to determine the residual concentration of degraded MB dye.

7.3 Results and Discussion

7.3.1 XRD

In order to determine the crystalline structure and phase of the synthesized products, XRD measurements were done. The XRD patterns of GO, rGO, pure CdO NPs and rGO-CdO nanocomposites are shown in Fig. 7.2a-d. The broad and intense peak of GO at $2\theta = 9.51^{\circ}$ correspond to reflection from (002) crystal plane. The interlayer spacing (0.923 nm) of GO was found to be much larger than that of graphite (0.336 nm). It may be due to the attachment of oxygen containing functional group with the graphite sheets [25].The oxygen based functional group attached at both sides of the graphite sheets create atomic defects in the graphite structure and tend to exfoliate it to a few layer of GO in an aqueous medium. The diffraction peak of rGO was found at $2\theta = 25.5^{\circ}$ corresponding to (002) plane and the peak corresponding to (002) plane of GO is almost disappeared. It indicates the successful reduction of GO to rGO [26].The interlayer spacing of rGO is found to be 0.353 nm, which is slightly higher than that of graphite (0.336 nm). It indicates there restoration of destroyed network of carbon atoms after reduction. The diffraction peaks of rGO-CdO nanocomposites are same as those observed for pure CdO NPs at ~32.98°,

~38.27˚, ~55.26˚, ~65.91˚, ~69.24˚ originated due to reflection(111), (200), (220), (311), (222) planes of cubic phase of CdO (JCPDS No. 73-2245). The sharp intensity of diffraction peaks of pure CdO NPs and rGO-CdO nanocomposites suggest that the synthesized products have high crystallinity. No such peak corresponding rGO has been detected in XRD spectra of the nanocomposites. It further suggests that the GO was successfully reduced [27].The (111) peak of nocomposites is relatively broader than that of pure CdO NPs. The broadening of (111) peak suggests that the lattice structure of CdO is distorted by interaction with rGO sheets. The crystallite size of CdO NPs decorated over rGO sheets was calculated using Scherrer formula and its average value of size is found to be ~ 5 nm.

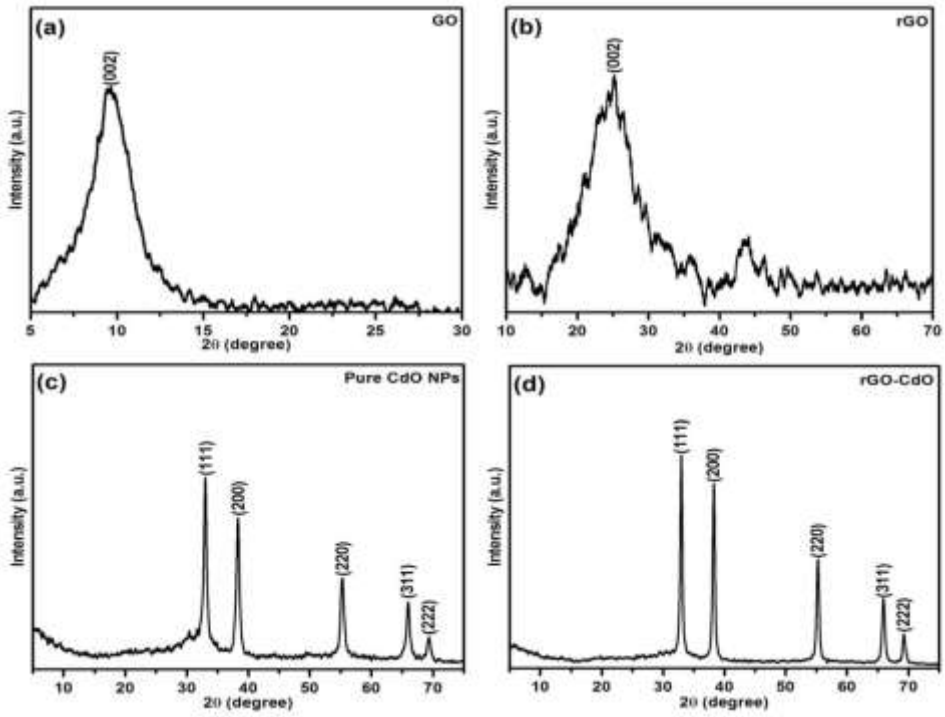


Fig. 7.2 XRD patterns for (a) GO (b) rGO (c) CdO NPs and (d) rGO-CdO nanocomposites.

7.3.2 HR-TEM and EDX

The hetero-structures of synthesized nanocomposites were verified by HR-TEM measurements. HR-TEM micrographs of rGO-CdO nanocomposites taken at different resolutions are shown in Fig. 7.3a-f. These micrographs show that the CdO NPs are well dispersed on rGO sheets. It can also be seen that the CdO NPs occupy most of the available surface area of rGO sheets, giving much higher loadings of CdO NPs in the nanocomposites. As seen in the Fig. 7.3a, the average size of the CdO NPs is calculated to be ~5 nm. It is also obvious that CdO NPs are intimately enveloped on rGO layers with visible wrinkles. These visible wrinkles suggest that the rGO sheets are composed of single or few layers [27]. This type of interfacial contact is favorable for effective charge transfer that restricts the fast recombination of e^- and h^+. I believed that such well anchored CdO NPs on rGO surface could prevent the restacking of rGO layers and enhance the stability of rGO sheets [27]. This property of rGO-CdO nanocomposites is quite useful for optoelectronics and photocatalytic applications. Additionally, the SAED pattern, as shown in Fig. 7.3g, shows that the formed rings belong to cubic structure of CdO, which is in good agreement with the XRD results. The elemental analysis of the nanocomposites was carried out by EDX spectra. EDX spectra, as shown in Fig. 7.3h, confirm that the synthesized samples are impurity free and only three intense peaks were observed. These peaks correspond to constituent elements of rGO-CdO nanocomposites like carbon (C), cadmium (Cd) and oxygen (O) atoms. The histogram, as shown in Fig. 7.3i, suggests that the particle size distribution of CdO NPs on rGO sheets is narrow with the average particle

size of ~ 5 nm. This result is consistent with the value calculated using XRD data. All these experiments authenticate explicitly that CdO NPs have been successfully decorated over the rGO sheets.

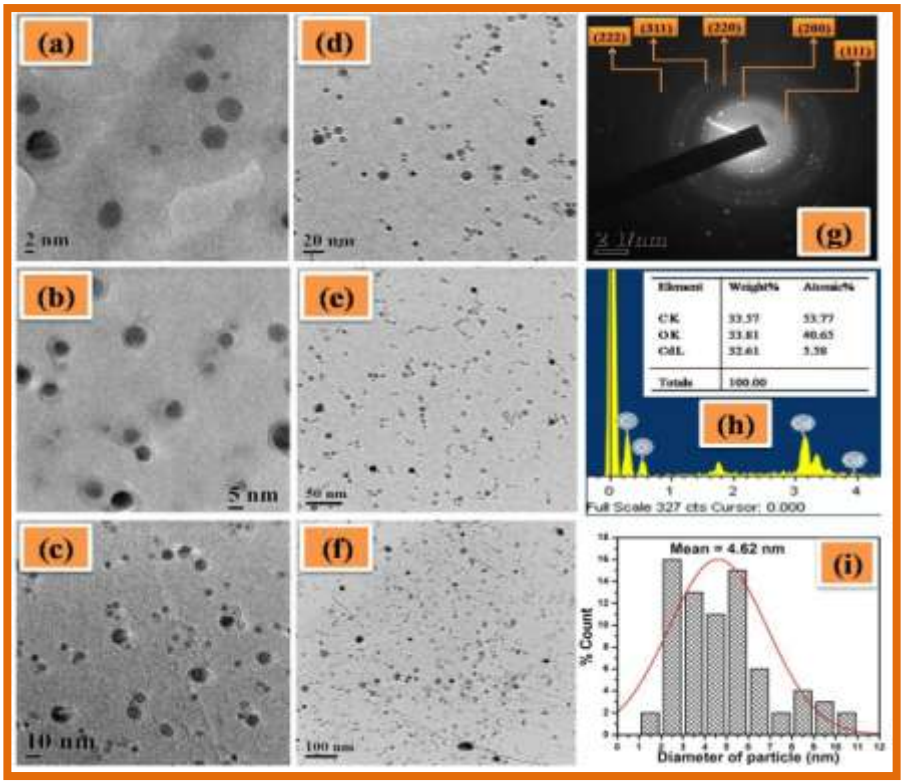


Fig. 7.3 (a-f) HR-TEM image of rGO-CdO nanocomposites, (g) SAED pattern of rGO-CdOnanocomposites (h) EDX spectrum of rGO-CdO nanocomposites (i) histogram of particle size distribution of CdO NPs decorated over rGO sheets.

7.3.3 Raman spectroscopy

Raman spectroscopy is a very convenient and nondestructive technique for the characterization of carbon based materials [28]. Fig. 7.4 shows the Raman spectra of GO (black), rGO (red), pure CdO NPs (green) and rGO-CdO (blue) nanocomposites recorded

in the spectral range 150-2700 cm^{-1}. The Raman spectra of GO show two bands at ~1343 and ~1598 cm^{-1} that correspond to D and G bands of graphite, respectively. While in rGO, these two bands are appeared at ~1328 and ~1573 cm^{-1}. The shifting in peak position of D and G bands in rGO as compared to GO suggests the structural change of the synthesized material after reduction. The G peak corresponds to the E_{2g} phonon at the Brillouin zone center whereas the D peak corresponds to the breathing modes of sp^2 atoms and requires a defect for its activation. However, the most prominent feature in rGO is the appearance of second order 2D band at ~2658 cm^{-1} [28].The 2D band is originated due to double resonance process. The position and shape of the 2D band are key parameters to investigate the number of layers in GO and rGO. The sharp nature of 2D band at ~2658 cm^{-1} indicates more contribution from single layered sheet in the prepared samples [29]. From Raman spectra, as shown in Fig. 7.4, it is found that the intensity ratio, ID/IG of rGO (1.04) is higher than that of GO (0.98). This implies that the average size of sp^2 domain is decreased upon reduction of GO into rGO. It confirms the formation of pores (as defects and disorders) in the rGO layers. Further, the intensity ratio I2D/IG (0.14) of rGO is decreased than that of GO (0.38), which suggests that the GO is highly reduced to rGO [27]. Raman spectrum of pure CdO NPs shows Raman bands at ~297, ~387 and ~832 cm^{-1}. Kumar and Ojha [12] has reported that the Raman bands at ~297 and ~387 cm^{-1} are assigned to 2TA(L) and 2LA(L) mode. The Raman peak appeared at ~387 cm^{-1} may be due to high two phonons density of states in the spectral range 300-450 cm^{-1} and it may probably arise from 2LA overtones at different high symmetry points of the Brillouin zone.

According to selection rules, both TO and LO modes are dipole forbidden and therefore all features in the spectrum can be attributed to second order Raman scattering process. The Raman peak appeared at ~ 832 cm^{-1} is assigned to 2LO (L) [30]. Besides, characteristics Raman features corresponding to rGO, Raman spectra of rGO-CdO nanocomposites show only one broad Raman peak at ~387 cm^{-1}. It is attributed to the CdO NPs decorated over the rGO sheets. This is in good agreement with HR-TEM results where CdO NPs are well anchored on rGO surface. The remarkable shift in D band of rGO-CdO nanocomposites may be due to softening of the optical phonons resulting due to the decoration of well dispersed CdO NPs over the surface. The higher ID/IG ratio (1.17) in rGO-CdO nanocomposites than that of GO (0.98) and rGO (1.04) indicates that the average size of sp^2 domain is decreased in rGO-CdO nanocomposites.

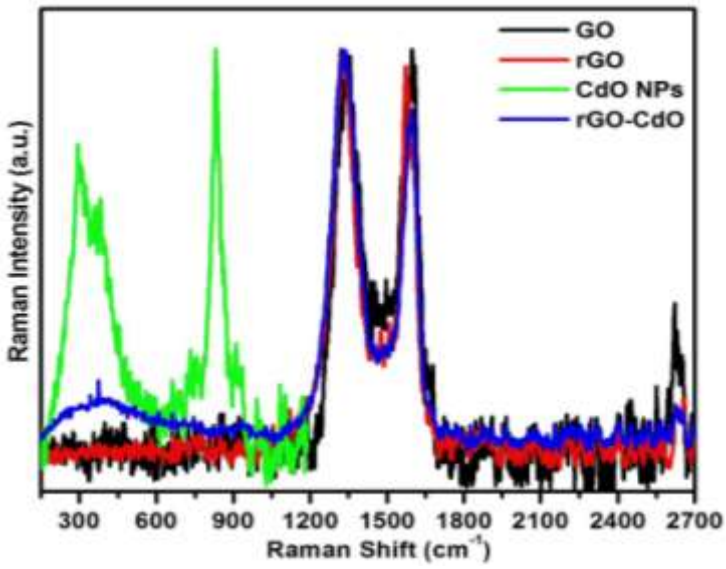


Fig. 7.4 Raman spectra of GO (black), rGO (red), CdO NPs (green) and rGO-CdO nanocomposites (blue).

7.3.4 UV-VIS spectroscopy

From the well packed structure of sp^2 bonded carbon atoms of rGO, it is expected that the rGO-CdO nanocomposites will absorb delocalized π bond of the organic compounds in the aqueous solution. Once the light is absorbed by the rGO-CdO nanocomposites, the organic compounds could be degraded by the photocatalytic activity of CdO NPs decorated over the rGO sheets. In order to understand the absorption behavior of the synthesized products, UV-VIS absorption spectra of rGO, pure CdO NPs and rGO-CdO nanocomposites have been recorded in the spectral range 200-800 nm and shown in Fig. 7.5. The absorption spectrum of rGO shows two prominent peaks at ~228 and ~258 nm. A similar type of additional peak at ~223 nm along with characteristic absorption peak at ~265 nm had also been observed for rGO in earlier study [31].The absorption peak observed at ~258 nm is blue shifted by 7 nm compared to its reported value in rGO. The blue shifting of absorption peak is generally attributed to the excitation of π-plasmon of graphitic structure [31]. It may also be due to number of graphene layers present in the rGO sheets. The additional peak at ~228 nm may be due to oxygen containing functional group present in rGO. It could also be confirmed by the presence of D band in the Raman spectra of rGO (see Fig. 7.4). It is reported that the Raman spectra of high quality rGO do not show D band [32].The bulk CdO is a semiconducting material with direct band gap of 2.3 eV (539 nm) and indirect band gap of 1.36 eV (912 nm) [12].The absorption spectra of pure CdO NPs, as shown in Fig. 7.5, show two absorption peaks at ~ 232 and ~278 nm. The absorption peak at ~232 nm may be due to inter band transition from deep level electrons of VB while

the peak at ~278 nm is due to quantum confinement effect. These two absorption peaks show blue shift compared to its position in bulk CdO. The blue shift of the absorption peak compared to bulk CdO can be explained by the theory of effective-mass approximation developed by Brus [33].In another study, it is reported that the absorption between 250 and 350 nm may be due the ligand-to-metal charge-transfer transitions [12].The UV-VIS absorption spectra reported in previous study [34] on II-VI semiconductor nanostructures indicate that the shoulder exciton peak is associated with the size distribution of NPs. It is obvious by looking at Fig. 7.5 that the position of absorption peaks for rGO-CdO nanocomposites is almost same as the peak position of pure CdO NPs. The broadening in the absorption peaks of rGO-CdO nanocomposites revealed a strong coupling between rGO sheets and CdO NPs.

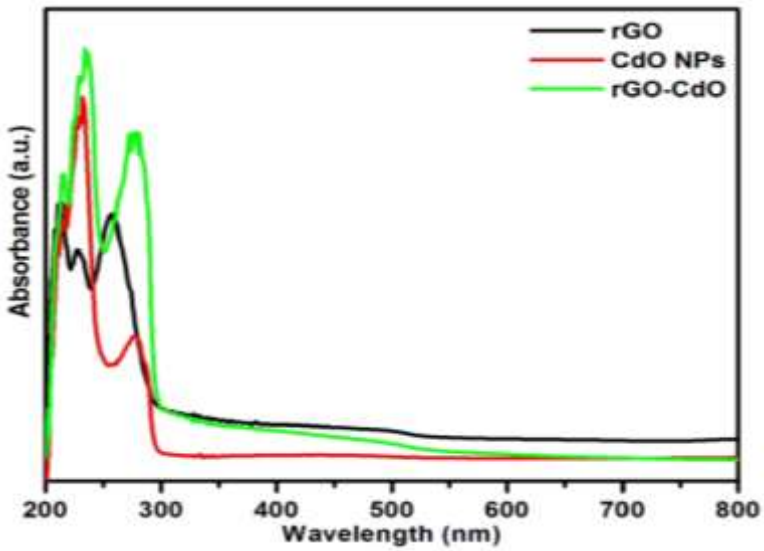


Fig. 7.5 UV-VIS spectra of rGO (black), CdO NPs (red) and rGO-CdO nanocomposites (green).

7.3.5 PL spectroscopy

The PL spectroscopy of the synthesized products was performed at room temperature to study the emission behavior of the samples excited by 320 nm wavelength. The PL spectra of pure CdO NPs and rGO-CdO nanocomposites excited by 320 nm excitation wavelength are shown in Fig. 7.6. The PL spectrum of as prepared pure CdO NPs shows two emission bands at ~410 and ~430 nm. .A broad shoulder band at ~460 nm was also observed in the PL spectra of both, pure CdO NPs and rGO-CdO nanocomposites. The shape and position of the emission band at ~410, ~430 and ~460 nm of rGO-CdO nanocomposites are same as that of pure CdO NPs except the change in intensity. It may be due the fact that both, pure CdO NPs and rGO-CdO nanocomposites are prepared by hydrothermal method at same conditions [35].The emission peak at ~ 430 nm might be attributed to the combination of e^- from the CB and h^+ from the VB [36] whereas the emission peak at ~410 nm is assigned to band edge or near band edge emission [34]. Dong and Zhu [34] has reported that the CdO NPs show strong emission peak at ~ 400 or ~ 460 nm, depending on the particle size under excitation wavelength of 350 nm. The broad intense peak at ~ 460 nm is attributed to the surface-state emission or deep trap emission [34].It has been found that the PL intensity of rGO-CdO nanocomposites is decreased in comparison to intensity of pure CdO NPs. It suggests that the decrease in intensity may be due to interfacial charge transfer from CdO NPs to rGO sheets. It also provides an additional channel to transport charge carriers [35].The decrease in full width at half of the maximum (FWHM) for rGO-CdO nanocomposites compared to pure CdO NPs indicate the enhancement of recombination

time of e^{-}-h^{+} pairs. This property of rGO-CdO nanocomposites may be useful for optoelectronics and photodegradation of organic compounds.

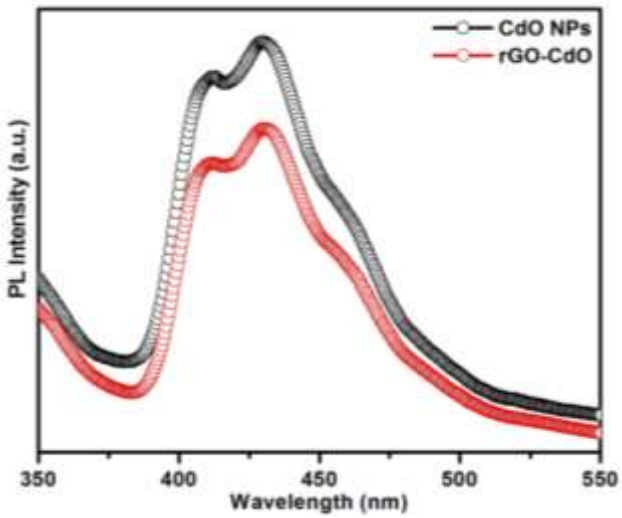


Fig. 7.6 PL spectra of CdO NPs (black) and rGO-CdO nanocomposites (red) excited at 320 nm.

7.3.6 Magnetic properties

In order to see the magnetic behavior of pure CdO NPs and rGO-CdO nanocomposites, VSM measurements of synthesized samples have been done at room temperature under the applied magnetic field in the range of -15000 Oe to +15000 Oe. The diamagnetic signal coming from the sample holder was subtracted from the measured magnetic signal of the samples. The variation of magnetization vs. applied field for pure CdO NPs and rGO-CdO nanocomposites is shown in Fig. 7.7a and 7b, respectively. I have observed hysteresis loop for pure CdO NPs, as shown in Fig. 7.7a. Interestingly, the presence of hysteresis loop is also observed for the CdO NPs decorated over rGO sheets (see Fig. 7.7b). The insets of

Fig. 7.7a and 7.7b are the enlarged hysteresis loop. The presence of hysteresis loop for pure CdO NPs and CdO NPs decorated over rGO sheets indicates the RTFM nature of these samples. The presence of non zero coercivity also demonstrates the weak ferromagnetic behavior of the synthesized samples [37].With the help of hysteresis loop, the value of coercivity (Hc) and saturation magnetization (Ms) for pure CdO NPs was calculated to be 239 Oe and 0.021emu/g, respectively. However, in case of rGO-CdO nanocomposites, the value of Hc and Ms turns out to be 233Oe and 0.034emu/g, respectively. The presence of Hc for rGO-CdO nanocomposites demonstrates that the rGO based materials may be a prospective candidate for application in storage of high density information [37]. The increased value of Ms for rGO-CdO nanocomposites compared to the pure CdO NPs may be due to the interaction of magnetic domains of CdO NPs with spin units present on the rGO sheets. The interaction of magnetic domains of CdO NPs with spin units present on the rGO sheets is shown schematically in Fig. 7.8.Wang et al. [38] had reported the presence of RTFM for graphene. The presence of RTFM in graphene may be attributed to itinerant electron magnetism rather than super exchange magnetic coupling interaction between spins like molecule-based magnets [38]. A number of studies [38-39] had been done on magnetic behavior of graphene and it had been reported that the RTFM could be originated due to various defects present in the graphene structure. Radovicet al. [40] has reported that the removal of functional group would introduce various defects such as; vacancies and topological defects on graphene structure with unpaired electrons as spin units which induced magnetic behavior in graphene. The

stability of unpaired electrons, as spin units, in these structures is possible mainly due to the large π-conjugation between the carbon atoms [38]. Thus, the possible origin of ferromagnetism may be credited to spin units existing as defects in the graphene sheets.

The bulk CdO is a diamagnetic material at room temperature. However, in the present study the CdO NPs show weak ferromagnetic nature at room temperature. The RTFM of metal oxide based NPs such as; ZnO [41], SnO_2[42]and CeO_2 [43] has been observed and well studied by several research groups. Sundaresan et al. [44] had explained the origin of ferromagnetic nature in oxide based NPs in terms of exchange interactions between localized electron spin moments resulting from oxygen vacancies at the surface of nanoparticles. It has been suggested that the ferromagnetism may be a universal characteristic of metal oxides nanoparticles. However, the above explanation for presence of RTFM in metal oxides NPs could only be applicable to the metal elements which have unpaired spin in their outermost shell. The unpaired spin may induce weak ferromagnetic nature in the absence of oxygen vacancies at the surface of the nanostructures. However, in the present report, the RTFM nature of CdO NPs could not be explained on the basis of oxygen vacancies since the Cd atom does not have unpaired electron in their outer most shell and thus the same explanation could not be used for such systems. In order to explain the weak ferromagnetic nature of CdO NPs, I proposed a scheme for filling of electrons in the different electronic states of CdO. The proposed scheme is shown in Fig. 7.9. As per scheme, there are two possibilities for filling of two valence electrons as donated by the Cd atom to p orbital of O atom (i) both electrons may occupy the electronic states in the 2p

orbital of oxygen atom such that the total spin becomes zero (S=0), called singlet state (ii) one electron may go to 2p orbital and another may go to 3s orbital of oxygen atom making total spin one (S=1), called triplet state. The density functional calculations (DFT) shows that the structural energy of CdO in S=1 state is 0.46 eV lowered than that of S=0 state. Thus, on the basis of results obtained from the DFT calculations, one can say that the scheme (ii), where S=1, is energetically most possible way for the formation of CdO. As I know that the magnitude of spin multiplicities, 2S+1, for the clusters resulting considerable variations in the magnetic moment. The magnetic moment of any molecule/clusters is related with the spin by the expression $\mu=2S\mu_B$, where μ_B is the Bohr magneton. Since the CdO is formed under scheme (ii), where S=1, therefore according the expression $\mu =2S\mu_B$, CdO exhibits weak ferromagnetic behaviour, as I have observed experimentally. Thus, it is expected that interaction of magnetic moments of pure CdO and spin units present over graphene is mainly responsible for inducing RTFM in rGO-CdO nanocomposites.

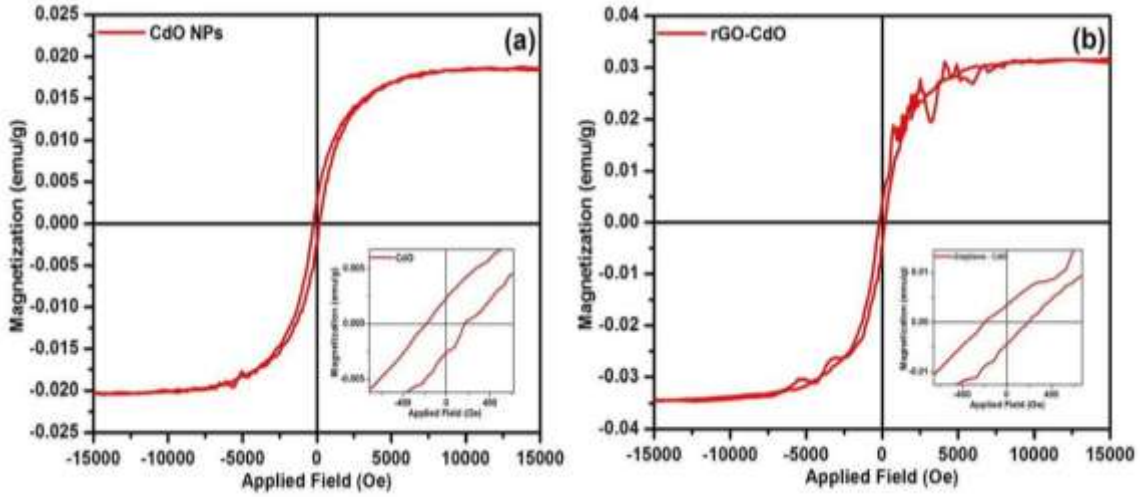


Fig. 7.7 M-H curve of (a) CdO NPs (b) rGO-CdO nanocomposites. The inset of each figure shows the corresponding M-H curve for applied field - 400 Oe < H < + 400 Oe.

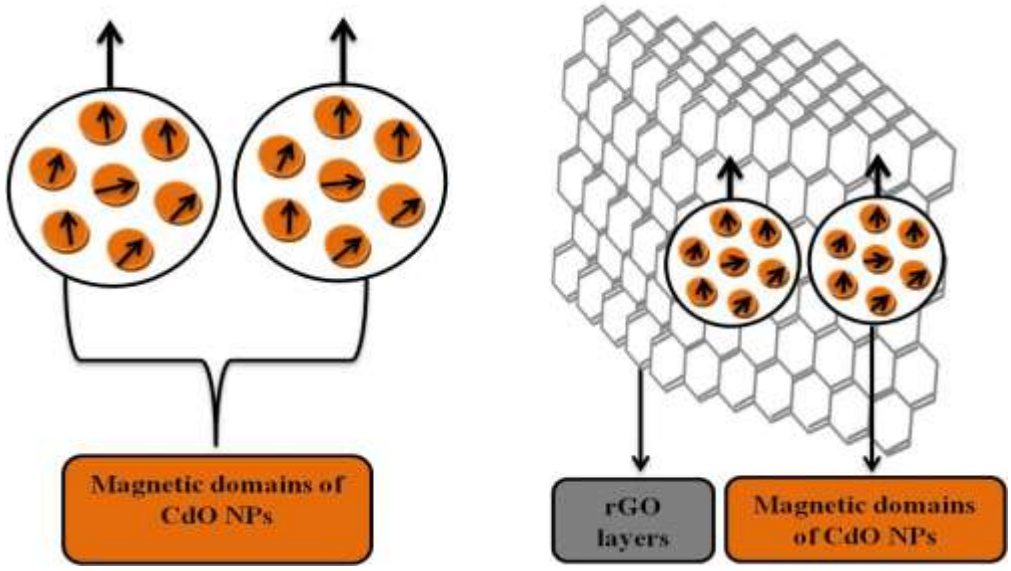


Fig. 7.8 Mechanism for RTFM in pure CdO NPs and rGO-CdO nanocomposites.

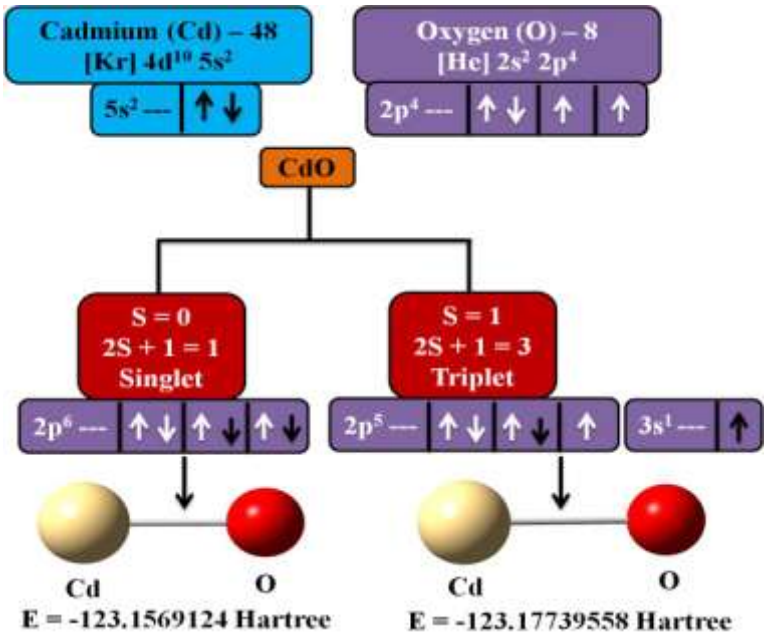


Fig. 7.9 A scheme for distribution of electrons in different electronic states of CdO.

7.3.7 Photocatalytic degradation of MB dye

The photocatalytic activities of pure CdO NPs and rGO-CdO nanocomposites have been evaluated using the degradation of MB dye in aqueous solution under UV light irradiation. Compared to pure CdO NPs, rGO-CdO nanocomposites exhibit enhanced photocatalytic activity. The characteristic absorption peak of MB dye at ~664 nm is selected to monitor the photodegradation process. Fig. 7.10a-b shows the degradation of MB dye with pure CdO NPs and rGO-CdO nanocomposites under UV light of wavelength 254 nm. In order to estimate the residual concentration of MB dye after photodegration, the ratio C/C_0 is calculated and plotted with reaction time where C_0 and C are the concentrations of MB dye at t=0 and at any time t, respectively. The plot of C/C_0 with reaction time for rGO, pure CdO NPs and rGO-CdO nanocomposites is shown in Fig. 7.10c. From Fig. 10c, it is clear

that after exposing the mixed solution of MB dye and photocatalysts such as; CdO NPs, rGO and rGO-CdO nanocomposites by UV radiation for 110 min, the pure CdO NPs degrade the MB dye up to 65% while the dye solution mixed with rGO-CdO nanocomposites degrade the MB dye up to 80%. Thus, it is quite evident by looking at the experimental results that the incorporation of rGO has a significant influence on enhancing the photocatalytic activity of pure CdO NPs. This result confirms that the pure CdO NPs has intrinsic photocatalytic activity under UV light irradiation and its photocatalytic activity may be enhanced by decorating them on rGO sheets. The degradation of MB dye is almost negligible in absence of photocatalysts such as, pure CdO NPs or CdO NPs decorated over rGO sheets. However, MB dye was found to be slightly degraded in the presence of rGO due to its light adsorption ability originated by π-π stacking interaction between rGO sheets and MB dye molecule [45].

The degradation mechanism of the MB dye with pure CdO NPs and rGO-CdO nanocomposites under UV light irradiation is shown in Fig. 7.11.When mixed solution of dye and photocatalyst is exposed to UV light with excitation wavelength 254 nm, which has a photon of energy equal or greater than the band gap energy (4.5 eV) of the CdO NPs, electron (e^-) of VB is excited to the CB of CdO NPs by inducing a hole (h^+) in the VB. The excited e^- will react with adsorbed O_2 molecules and forms $O_2^{\bullet -}$ radicals. On the other hand, the h^+ of VB of CdO NPs are taken by OH^- derived from the aqueous solution and consequently ·OH radicals are formed in the mixed solution. These radicals, ($O_2^{\bullet -}$and ·OH) act as oxidizing agent in the solution. These radicals react with MB dye and decompose it

into CO_2, H_2O and other small molecules. The recombination time of e^-- h^+ pairs is faster for pure CdO NPs. The fast recombination of e^--h^+ pairs slowed down the degradation process. The incorporation of rGO sheets to CdO NPs prolonged the recombination process of e^--h^+ pairs and as a consequence, the degradation of MB dye is enhanced significantly. In fact, in rGO-CdO nanocomposites, the rGO sheets act as electron acceptor and transporter of electrons due to nice interfacial contact between rGO sheets and CdO NPs. As a result, the electrons of CB of CdO NPs easily transfered to the rGO sheets and prolonged the recombination process of e^--h^+ pairs. The effective delay in the recombination time of photogenerated e^-- h^+ pairs in CdO NPs causes to increase the density of free charge carriers in the dye solution mixed with rGO-CdO nanocomposites. These additional free charge carriers, further, react with O_2 and OH^- present in the mixed solution and forms $O_2^{\bullet -}$ and ·OH radicals, which effectively react with MB dye to degrade the dye molecules relatively high than that of the degradation produced by the pure CdO NPs. The complete degradation process of MB dye in presence of rGO-CdO nanocomposites as a photocatalyst may be explained with the help of following equations:

$$\text{rGO-CdO nanocomposites} + \text{photon } (h\nu, 254\text{nm}) \rightarrow (e^-)\ CB + (h^+)\ VB$$

$$H_2O + h^+ \rightarrow OH^- + H^+$$

$$OH^- + h^+ \rightarrow \cdot OH\ (\text{radical})$$

$$O_2 + e^- \rightarrow O_2^{\bullet -}(\text{radical})$$

$$\text{MB dye} + (\text{rGO-CdO}) + O_2^{\bullet -} \rightarrow \text{degraded products}$$

$$\text{MB dye} + (\text{rGO-CdO}) + \cdot OH \rightarrow \text{degraded products}$$

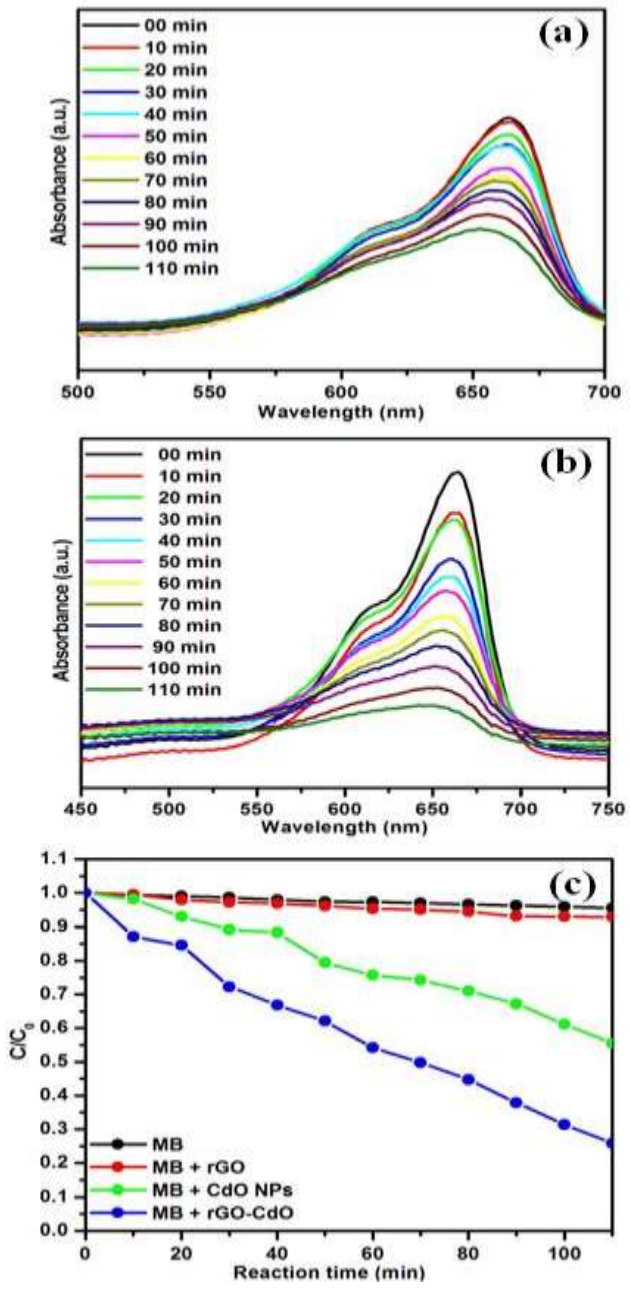


Fig. 7.10 Absorption spectra of a solution of MB dye in presence of (a) CdO NPs (b) rGO-CdO nanocomposites under UV light irradiation (c) degradation of MB dye with different photocatalysts in terms of relative concentration (C/C_0) of MB dye with reaction time.

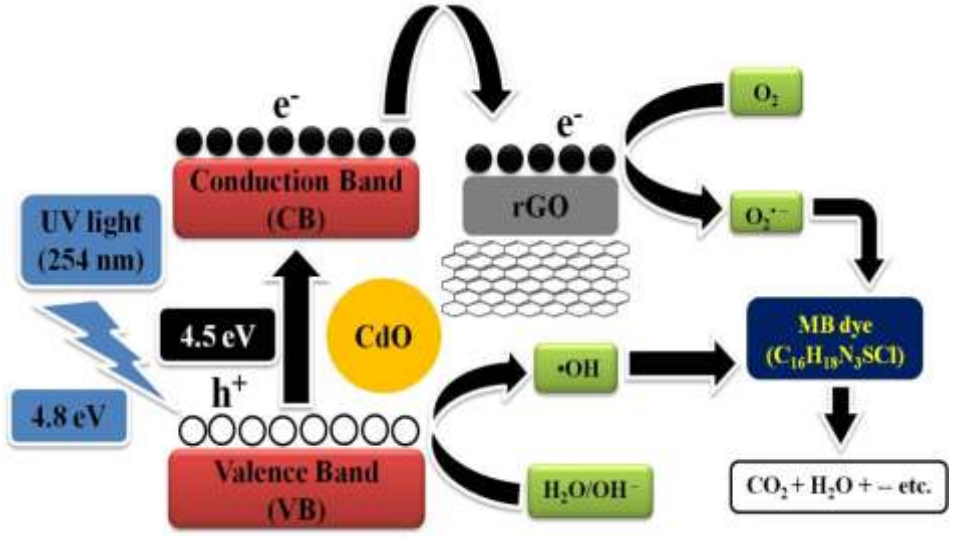


Fig. 7.11 Schematic diagram showing the charge transfer process for the photodegradation of MB dye.

7.4 Conclusion

In summary, I have developed a facile one-step in situ hydrothermal method to grow highly dispersed CdO NPs on rGO sheets. Further, the pure CdO NPs and rGO sheets have also been synthesized by following the same synthesis procedure. The structural, optical and magnetic properties along with photocatalytic activity of pure CdO, rGO and rGO-CdO nanocomposites for degradation of MB dye have been discussed. The results obtained from HR-TEM and Raman measurements show that the hydrothermal method is a good approach to decorate the monodispersed, stable and dense CdO NPs on rGO sheets. HR-TEM observations indicate that the rGO sheets are fully exfoliated and decorated with CdO NPs of an average size of ~5 nm. The rGO-CdO nanocomposites are found to have enhanced photocatalytic degradation of MB dye molecule compared to pure CdO NPs and

rGO sheets under UV light irradiation. The enhanced photocatalytic activity of rGO-CdO nanocomposites is attributed to the increase of free charge carriers due to prolongation of recombination time of e^{-}-h^{+} pairs. The pure CdO NPs shows RTFM. The RTFM of CdO NPs is increased on decoration of these NPs over rGO sheets. Due to enhanced photocatalytic activity of the rGO-CdO nanocomposites, it may be used as promising material for practical applications in environmental pollutant management.

References

[1] A. K. Geim, K. S. Novoselov, Nat. Mater., 2007, **6**, 183.

[2] M. D. Stoller, S. Park, Y. Zhu, J. An, R. S. Ruoff, Nano Lett., 2008, **8**, 3498.

[3] K. I. Bolotin, K. J. Sikes, Z. Jiang, M. Klima, G. Fudenberg, J. Hone, P. Kim, H. L. Stormer, Solid State Commun., 2008, **146**, 351.

[4] A. A. Balandin, S. Ghosh, W. Bao, I. Calizo, D. Teweldebrhan, F. Miao, C. N. Lau, Nano Lett., 2008, **8**, 902.

[5] C. Lee, X. Wei, J. W. Kysar, J. Hone, Science, 2008, **321**, 385.

[6] Y. Zhang, Y. -W. Tan, H. L. Stormer, P. Kim, Nature, 2005, **438**, 201.

[7] P. Blake, P. D. Brimicombe, R. R. Nair, T. J. Booth, D. Jiang, F. Schedin, L. A. Ponomarenko, S. V. Morozov, H. F. Gleeson, E. W. Hill, A. K. Geim, K. S. Novoselov, Nano Lett., 2008, **8**, 1704.

[8] K. S. Kim, Y. Zhao, H. Jang, S. Y. Lee, J. M. Kim, K. S. Kim, J. -H. Ahn, P. Kim, J. Y. Choi, B. H. Hong, Nature, 2009, **457**,706.

[9] J. S. Bunch, A. M. V. Zande, S. S.Verbridge, I. W. Frank, D. M. Tanenbaum, J.

M. Parpia, H. G. Craighead, P. L. McEuen, Science, 2007, **315**, 490.

[10] Y. Yang, L. Ren, C. Zhang, S. Huang, T. Liu, ACS Appl. Mater. Interfaces, 2011, **3**, 2779.

[11] Y. Wei, C. Gao, F. -L. Meng, H. -H. Li, L. Wang, J. -H. Liu, X. -J. Huang, J. Phys. Chem. C, 2012, **116**, 1034.

[12] S. Kumar, A. K. Ojha, AIP Advances, 2013, **3**, 052109.

[13] J. Chang, V. V. Todkar, R. S. Mane, D. Ham, T. Ganesh, S. H. Han, Phys. E, 2009, **41**, 1741.

[14] H. Park, S. Chang, J. Jean, J. J. Cheng, P. T. Araujo, M. Wang, M. G. Bawendi, M. S. Dresselhaus, V. Bulovic, J. Kong, S. Gradecak, Nano Lett., 2013, **13**, 233.

[15] Y. Yao, Z. Yang, H. Sun, S. Wang, Ind. Eng. Chem. Res., 2012, **51**, 14958.

[16] S. Wu, H. Cao, S. Yin, X.Liu, X. Zhang, J. Phys. Chem. C,2009, **113**, 17893.

[17] A. Sarkar, A. Shchukarev, A. -R. Leino, K. Kordas, J. -P. Mikkola, P. O. Petrov, E. S. Tuchina, A. P. Popov, M. E. Darvin, M. C. Meinke, J. Lademann, V. V. Tuchin, Nanotechnology, 2012, **23**, 475711.

[18] J. Zhang, Z.Xiong, X. S. Zhao, J. Mater. Chem., 2011, **21**, 3634.

[19] H. -i. Kim, G. -h. Moon, D. Monllor-Satoca, Y. Park, W. Choi, J. Phys. Chem. C, **2012**, 116, 1535.

[20] U. Alvera, W. Zhou, A. B. Belay, R. Krueger, K. O. Davis, N. S. Hickman, Appl. Surf. Sci., 2012, **258**, 3109.

[21] T. Ghosh, K. Ullah, V. Nikam, C. -Y. Park, Z. -D. Meng, W. -C. Oh, Ultrason.

Sonochem., 2013, **20**, 768.

[22] W. Tao, J. Chang, D. Wu, Z. Gao, X. Duan, F. Xu, K. Jiang, Mater. Res. Bull., 2013, **48**, 538.

[23] N. Li, G. Liu, C. Zhen, F. Li, L. L. Zhang, H. M. Cheng, Adv. Funct. Mater., 2011, **21**, 1717.

[24] D. C. Marcano, D. V. Kosynkin, J. M. Berlin, A. Sinitskii, Z. Sun, A. Slesarev, L. B. Alemany, W. Lu, J. M. Tour, ACS Nano, 2010, **4**, 4806.

[25] S. Chen, J. Zhu, X. Wu, Q. Han, X. Wang, ACS Nano, 2010, **4**, 2822.

[26] C. Xu, X. Wang, J. Zhu, J. Phys. Chem. C, 2008, **112**, 19841.

[27] L. Jiang, M. Yao, B. Liu, Q. Li, R. Liu, H. Lv, S. Lu, C. Gong, B. Zou, T. Cui, B. Liu, J. Phys. Chem. C, 2012, **116**, 11741.

[28] C. Casiraghi, S. Pisana, K. S. Novoselov, A. K. Geim, A. C. Ferrari, Appl. Phys. Lett., 2007, **91**, 233108.

[29] O. Akhavan, ACS Nano, 2010, **4**, 4174.

[30] R. Cuscó, J. Ibáñez, N. Domenech-Amador, L. Artús, J. Zúñiga-Pérez, V. Muñoz-Sanjosé, J. Appl. Phys., 2010, **107**, 063519.

[31] X. Shen, J. Wu, S. Bai, H. Zhou, J. Alloy. Compd., 2010, **506**, 136.

[32] A. C. Ferrari, J. C. Meyer, V. Scardaci, C. Casiraghi, M. Lazzeri, F. Mauri, S. Piscanec, D. Jiang, K. S. Novoselov, S. Roth, A. K. Geim, Phys. Rev. Lett., 2006, **97**, 187401.

[33] L. E. Brus, J. Chem. Phys., 1984, **80**, 4403.

[34] W. Dong, C. Zhu, Opt. Mater., 2003, **22**, 227.

[35] G. Williams, P. V. Kamat, Langmuir, 2009, **25**, 13869.

[36] M. Benhaliliba, C. E. Benouis, A. Tiburcio-Silver, F. Yakuphanoglu, A. Avila-Garcıa, A. Tavira, R. R. Trujillo, Z. Mouffak, J. Lumin., 2012, **132**, 2653.

[37] B. Li, H. Cao, J. Yin, Y. A.Wu, J. H. Warner, J. Mater. Chem., 2012, **22**, 1876.

[38] Y. Wang, Y. Huang, Y. Song, X. Zhang, Y. Ma, J. Liang, et al., Nano Lett., 2009, **9**, 220.

[39] M. A. H. Vozmediano, M. P. Lopez-Sancho, T. Stauber, F. Guinea, Phys. Rev. B, 2005, **72**, 155121.

[40] L. R. Radovic, B. Bockrath, J. Am. Chem. Soc., 2005, **127**, 5917.

[41] Q. Xu, Z. Wen, H. Zhang, X. Qi, W. Zhong, L. Xu, D. Wu, K. Shen, M. Xu, AIP Advances, 2011, **1**, 032127.

[42] C. Wang, M. Ge, J. Z. Jiang, Appl. Phys. Lett., 2010, **97**, 042510.

[43] S. Phokha, S. Pinitsoontorn, S. Maensiri, J. Appl. Phys., 2012, **112**, 113904.

[44] A. Sundaresan, R. Bhargavi, N. Rangarajan, U. Siddesh, C. N. R. Rao, Phys. Rev. B, 2006, **74**, 161306.

[45] Y. Luo, S. Fan, N. Hao, S. Zhong, W. Liu, Cryst Eng Comm, 2015, **17**, 503.

CHAPTER - 8

Scope of future work

In this chapter, based on the research work reported in the present thesis, a brief description of future scope of research work has been given.

In the present work, CdO nanowires, CdO/MnO_2 (core/shell) nanostructures and monodispersed CeO_2 nanoparticles were synthesized by simple and low cost chemical methods such as; co-precipitation and sol-gel. The, GO, rGO, rGO-CdS and rGO-CdO nanocomposites were also synthesized by a facile one pot solvothermal/hydrothermal method. The co-precipitation and sol-gel methods are found to be one of the cheapest and easiest synthesis techniques for manufacturing size and shape controlled nanostructures such as; quantum dots, nanowires and core/shell nanostructures. The quantum dots, nanowires and core/shell nanostructures of other materials can be synthesized on the basis of synthesis protocols presented in this thesis. The optical, magnetic, photocatalytic and antimicrobial activities of other transition metal oxides nanostructures of different shapes and sizes could also be done. These special types of nanostructures are of great importance for several applications such as; optoelectronics, nanoelectronics, energy storage materials and environmental issues.

In addition to the technological application, the graphene based nanocomposites have been now considered as a promising material due to its unique properties and of great potential for application in many areas of science and technology, particularly to solve the problems of energy crisis and environmental issues. The graphene based metal oxides nanocomposites have been successfully made in the laboratory and its possible applications in the areas of supercapacitors, fuel cells, photovoltaic devices, photocatalysis and sensing platforms have been explored. The synthesis protocols reported in the present thesis for synthesis of graphene based metals oxides nanocomposites provide highly

dispersed nanostructures with intimate contact with the graphene sheets. The rGO-CdS and rGO-CdO nanocomposites show enhanced photocatalytic activity to degrade MB dye compared to degradation capability of individual CdS and CdO nanoparticles. Thus, in view of tumble band gap, weak ferromagnetism and enhanced photocatalytic activity of the synthesized metal oxide nanostructures and its nanocomposites with rGO, I would like to extend my future research in the areas of controlled synthesize and investigations on optical and magnetic properties of other metal oxide based nanostructures. Further, I shall also try to decorate well dispersed metal oxides nanostructures over rGO sheets to modify their optical and magnetic properties. The photocatalytic activities of pure metal oxides nanostructures and those decorated over the rGO sheets will be investigated for photodegradation of pollutant molecules under visible and UV irradiation. The future scope of research has been summarized under the following bullet points:

- I would like to find some more reducing agents to get high yield of rGO.
- Synthesis of other layered nanostructures such as; MoS_2 with graphene to get improved optical and magnetic properties.
- Investigation of new photocatalyst materials for photodegradation of long organic molecules.
- Synthesis of other semiconductor nanostructures of controlled shape and size using the synthesis protocols presented in the present thesis.
- Synthesis of rGO decorated with transition metal oxides nanostructures for enhanced photocatalytic activity.